CONTINUOUS VERSUS DISCONTINUOUS ELASTIC MODULUS DISTRIBUTION IN INVERSE PROBLEMS BASED ON FINITE ELEMENT METHODS

A Thesis

by

XUCHEN LIU

Submitted to the Office of Graduate and Professional Studies of
Texas A&M University
in partial fulfillment of the requirements for the degree of

MASTER OF SCIENCE

Chair of Committee,	Sevan Goenezen
Committee Members,	Hong Liang
	Anastasia Muliana
Head of Department,	Andreas A. Polycarpou

May 2015

Major Subject: Mechanical Engineering

ABSTRACT

Elasticity imaging, which is also known as Elastography, aims to determine the elastic property distribution of non-homogeneous deformable solids such as soft tissues. This can be done non-destructively using displacement fields measured with medical imaging modalities, such as ultrasound or magnetic resonance imaging. Elasticity imaging can potentially be used to detect tumors based on the stiffness contrast between different materials. This requires the solution of an inverse problem in elasticity. This field has been growing very fast in the past decade. One of the most useful applications of elasticity imaging may be in breast cancer diagnosis, where the tumor could potentially be detected and visualized by its stiffness contrast from its surrounding tissues. In this work the inverse problem will be solved for the shear modulus which is directly related to the Young's modulus through the Poisson's ratio. The inverse problem is posed as a constrained optimization problem, where the difference between a computed (predicted) and measured displacement field is minimized. The computed displacement field satisfies the equations of equilibrium. The material is modeled as an isotropic and incompressible material. The present work focuses on assessing the solution of the inverse problem for problem domains defined with a continuous and discontinuous shear modulus distribution. In particular, two problem domains will be considered: 1) a stiff inclusion in a homogeneous background representing a stiff tumor surrounded by soft tissues, 2) a layered ring model representing an arterial wall cross-section. The hypothetical "measured" displacement field for these problem domains will be created by solving the finite element forward problem. Additionally, noise will be added to the displacement field to simulate noisy measured displacement data.

According to the results of my thesis work, the potential of the elasticity imaging in the medical field is emerging. The inclusion in problem domain 1, representing a stiffer tumor in a uniform background, can be found and located in the shear modulus reconstructions. Thus, these reconstructed images can potentially be used to detect tumors in the medical field.

ACKNOWLEDGEMENTS

I would like to thank my committee chair, Dr. Goenezen, and my committee members, Dr. Liang, Dr. Muliana, for their guidance and support throughout the course of this research.

Thanks also go to my friends and colleagues and the department faculty and staff for making my time at Texas A&M University a great experience.

Finally, thanks to my mother and father for their encouragement.

TABLE OF CONTENTS

Page

LIST OF FIGURES

LIST OF TABLES

Page

1. INTRODUCTION

The elastic properties of tissues can be mapped in-vivo and non-invasively using interior displacement fields measured with medical imaging modalities such as ultrasound or magnetic resonance imaging. This requires the solution of an inverse problem in elasticity, which is often referred to as elasticity imaging or elastography [1-5, 9-11, 17, 20, 44, 45]. This has important applications in detecting tumors based on their stiffness contrast between the tumor and its surrounding tissue. One of the most useful applications of elasticity imaging may be in breast cancer diagnosis [6–8]. These elastic properties could be utilized to classify different tissue types and potentially distinguish between cancerous and benign tissues. Elastography initially started as strain imaging [36, 37] resulting in boundary sensitive elasticity images. In order to avoid these artifacts in strain imaging, the shear modulus reconstruction is obtained by solving the inverse problem from the physical equations of equilibrium for the actual elastic properties, such as the Young's modulus or shear modulus. Another method, known as direct inversion algorithms, solves the partial differential equations directly for the elastic property distribution [14, 24-27]. However, this method requires an accurate estimation of all components of the displacement field, which is usually not the case using displacement data from ultrasound techniques.

The solution of the inverse problem has been extended to nonlinear and incompressible hyperelastic materials in [9, 10]. Mesh locking due to the incompressibility constraint has been addressed therein as well utilizing stabilized finite element methods.

In this thesis, all material models are linear, and due to the plane stress assumption, no mesh locking for the incompressibility assumption is expected. The main focus of this thesis is to assess the error in the shear modulus reconstruction due to the assumption of shear modulus continuity in the problem domain when solving the inverse problem. In [9-11, 17] the elastic property distribution (e.g., shear modulus distribution) is interpolated with linear shape functions and the elastic properties are nodal unknowns in the finite element mesh. Thus, the number of elastic property unknowns is equivalent to the number of mesh nodes in the finite element model. This also implies that the elastic property distribution is continuous over the problem domain as opposed to discontinuous over finite elements which is common in most commercial finite element solvers. Thus, solving the inverse problem assuming a continuous elastic property distribution when the actual elastic property distribution is discontinuous, will lead to errors in the final reconstructions. In this thesis, this discretization error will be studied and its impact on the final reconstructed shear modulus distribution.

The discretization error in the finite element forward problem has been studied by various researchers. For example, Kim and Paulino [11] analyzed functionally graded materials, whose element incorporates the material property gradient at the size scale of the element. They used the generalized isoparametric formulation, i.e., the same shape functions to interpolate the unknown displacements, the geometry, and the material parameters. This important isoparametric concept is also applied in [9]. They compared the performance of elements for functionally graded materials with that of conventional homogeneous elements. Their findings show that the continuously defined material elements are superior to the conventional homogeneous elements. Horgan and Chan [12] investigated the effects of discontinuous versus continuous defined materials on the response of linearly elastic isotropic plane strain and plane stress cases. They considered an analog of the classic Lamé problem which showed that the response of the continuous case is significantly different from that of the discontinuous case.

The inverse problem in this thesis is posed as a constrained minimization problem and solved iteratively using a limited BFGS method, which is a quasi-Newton method. An objective function is formulated to minimize the difference between the predicted and measured displacement fields. A regularization term based on the total variation diminishing is also included in the objective function. The predicted displacement satisfies the forward problem. The constitutive model for the forward problem is modeled in plane stress and the material is assumed to be incompressible in 3D.

Again, since the shear modulus μ is a function of the coordinate, there are two main methods to interpolate it. One is to define the shear modulus element-wise [11, 12], this is that the shear modulus is constant on finite elements.

Another way is to define the shear modulus continuously by defining their shear modulus values on the mesh nodes and interpolate them with finite element shape functions in the entire problem domain. In this thesis, the forward problem will be solved utilizing both discretization methods for the shear modulus distribution. Then the inverse problem is solved utilizing the hypothetical "measured" displacement data from both discretization methods. However, the inverse problem is solved assuming that the shear modulus is defined continuously in the problem domain. The error in the final reconstructions will be compared for two problem domains representing 1) a small and stiff inclusion in a soft background domain representing a stiff tumor surrounded by soft tissue, and 2) a layered ring model representing an arterial wall.

2. METHODS

For the present work, an in-house written inverse problem solver will be utilized which is written based on a finite element framework. In the inverse solver program, the difference between the measured displacement and the predicted displacement is minimized iteratively. Here, the predicted displacement satisfies the forward problem, i.e. the equations of equilibrium, which is computed for the current estimate of the shear modulus distribution. The forward problem is briefly discussed for a constitutive model given in Section 2.1. Then the inverse problem along with the objective function are introduced in Section 2.2.

2.1 Forward Problem

In the forward problem the displacement field is solved for a given target shear modulus distribution and boundary conditions. While the material response is modeled to be linear, geometric nonlinearity has been taken into account despite of the fact that small strains were used throughout this work. The reason for this is pure convenience as is elaborated on more thoroughly below.

The inverse solver utilized in this work has a build-in forward problem solver based on finite element methods. The currently available subroutine supports a nonlinear material response with 2 elastic properties, the shear modulus and a nonlinear elastic property. This is due to the fact that most soft tissues have a nonlinear stress-strain response with gradual stiffening at large strains [39, 40]. Researchers often use an exponentially stiffening strain energy function to model this nonlinear mechanical response in soft tissues [41, 42]. In [9], the authors replace the first principal invariant of the Cauchy Green tensor I_1 in the Blatz model with $J^{-2/3}I_1$, leading to a stress formulation that has a clearly defined deviatoric and hydrostatic stress term. The strain energy function used therein is given by:

$$W = \frac{\mu}{2\gamma}\left(e^{\gamma\left(J^{-\frac{2}{3}}I_1-3\right)}-1\right) \tag{2.1}$$

Here μ is the shear modulus, γ is a nonlinear parameter that describes the nonlinear material response, and I_1 = trace(C) is the first principal invariant of the Cauchy Green tensor. It is a standard procedure to derive the stress-strain relationship from this strain energy density function as well as the finite element algorithms. The details on this are omitted here and details on this can be reviewed in [9].

The nonlinear stress-strain behavior in uniaxial tension for this strain energy density function is given by the equation:

$$\sigma = \mu\left(\lambda^2 - \frac{1}{\lambda}\right)e^{\gamma\left(\lambda^2+\frac{2}{\lambda}-3\right)} \tag{2.2}$$

where σ is the uniaxial Cauchy stress and λ is the stretch. As mentioned earlier, the present work focuses on linear materials, which can be represented by this strain energy density function by setting the nonlinear property to zero. This leads to the exponential to become 1. It is noted that geometric nonlinearity is taken into account following this procedure.

2.2 Inverse Elasticity Problem

The shear modulus is reconstructed by solving an inverse problem for a known displacement field in the problem domain. The inverse problem is posed as a constrained minimization problem and solved iteratively using the limited BFGS method, which is a quasi-Newton method. The predicted displacement satisfies the forward problem for the current estimate of the shear modulus. The inverse problem formulation is as follows: Say we have n measured (numerical) displacement fields $u_{meas}^{1},\dots,u_{meas}^{n}$, find the shear modulus μ such that the objective function

$$\pi = \frac{1}{2}\sum_{i=1}^{n} w_i \left\| Tu^i - Tu_{meas}^i \right\|_0^2 + \frac{1}{2}\alpha\int_{\Omega_0}\sqrt{\left|\nabla\mu\right|^2 + c^2}\, d\Omega_0 \tag{2.3}$$

is minimized based on the predicted displacement fields that satisfy the equations of equilibrium and boundary conditions.

The general equation for the objective function is shown in Eq. (2.3), where the first term is a measure of the difference between the measured (numerical) and predicted displacement fields in the L_2 norm represented by $\left\|\bullet\right\|_0^2$. Then a weighting factor w_i is used to scale each term to make sure that all the displacements, small and large, have the same contribution to the objective function. The tensor T is a diagonal tensor that allows a different weight for each displacement component. The regularization term is shown as the second term in Eq. (2.3), where α is the regularization parameter. This has to be chosen appropriately depending on the noise level in the measured displacements. The regularization factor can be chosen based on the so called L-curve method, the Morozov's discrepancy principle, or on a smoothness criteria as utilized in this work. The smoothness criteria assumes that a small region is sufficiently smooth, while the overall shear modulus distribution is not overly smoothed, which could occur for a large choice of the regularization factor. More information about how to choose appropriate regularization parameter can be referred to [43]. The total variation diminishing (TVD) regularization is used because it can smooth the overall solution of the inverse problem while the sharp inclusion boundaries are still preserved ([16]). In other words, gradients in the shear modulus are not penalized. The constant c is a small non-zero number that ensures that the regularization term is differentiable.

Finally, it is important to note that the gradient of the objective function with respect to the nodal unknown shear modulus is required at every minimization call, and it is crucial to compute this efficiently utilizing the adjoint method. The adjoint method enables solving the gradient, thus the overall inverse problem, in a reasonable time. A flow chart is given below, listing the steps in solving the inverse problem with the adjoint method. Details on the gradient calculation are given in [9, 10, 11, 17] and will not be further discussed here. Figure 2.1 shows a flow chart of solving the inverse problem.

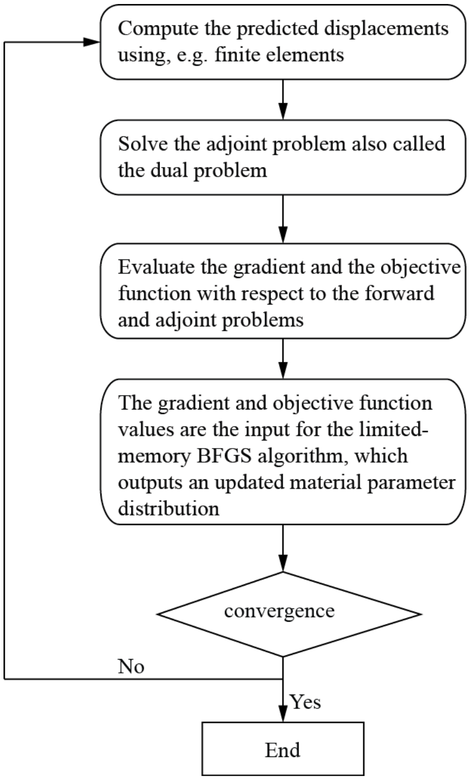

Figure 2.1 Flow chart of solving the inverse problem

3. RESULTS

3.1 Strain Analysis in Forward Problem

In this section a strain error analysis will be performed to compare the strain from the forward problem in both element-wise and continuously defined materials for two models, Model 1 and Model 2 described below. This analysis will be done utilizing a coarse and a fine mesh with bilinear finite elements.

3.1.1 Target Shear Modulus Distribution in Model 1

The first is a model that can represent a stiff tumor in a homogeneous soft background with unit length. Uniform Dirichlet boundary conditions are prescribed on the top with a magnitude of 0.01. This yields an overall compressive strain of 1%. The radius of the inclusion is 0.2. The motion in y direction of the bottom edge is fixed and the center node of the bottom edge is fixed to avoid rigid body motion. The other boundary conditions are assumed to be traction free. The shear modulus ratio between the inclusion and the background is 10. The model is shown in Figure 3.1.

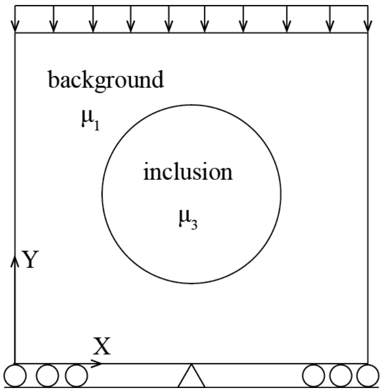

Figure 3.1 Model 1

Figure 3.2 shows the target shear modulus distribution in both continuously and element-wise defined materials using a coarse mesh and a fine mesh. The coarse mesh has 900 bilinear elements and the fine mesh has 3600 bilinear elements. The corresponding target shear modulus distribution along the horizontal centerline is shown in Figure 3.3.

In Figure 3.3 (a), (b), the linear transition of the shear modulus occurs at the border between the inclusion and the background. This demonstrates that the material is continuously defined. While in Figure 3.3 (c) and (d), the discontinuous transition of the shear modulus occurs at the border of the inclusion and the background. This demonstrates that the material is element-wise defined. As the mesh is refined (cf. (a), (b)), the linear transition of the shear modulus is getting closer to the discontinuous case.

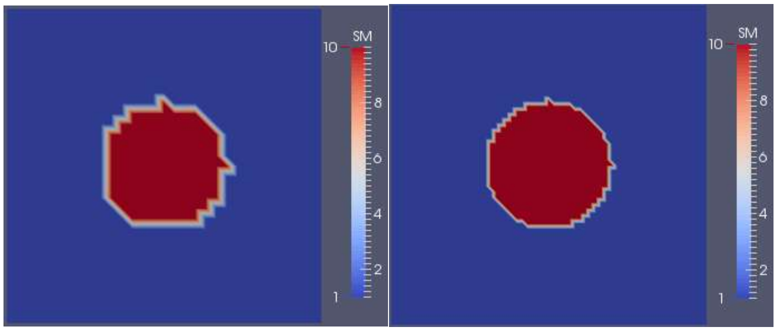

(a) Continuously defined material coarse mesh (b) Continuously defined material fine mesh

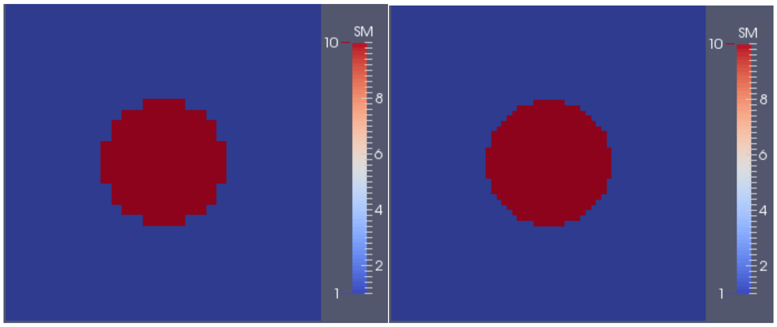

(c) Element-wise defined material coarse mesh (d) Element-wise defined material fine mesh

Figure 3.2 Target shear modulus distribution

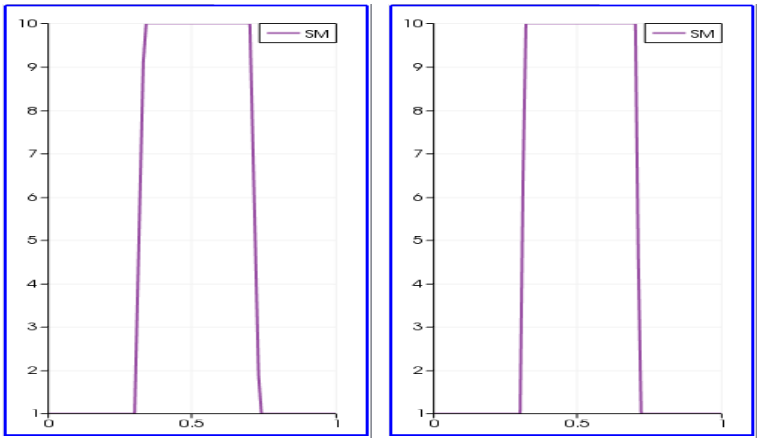

(a) Continuously defined material in coarse mesh (b) Continuously defined material in fine mesh

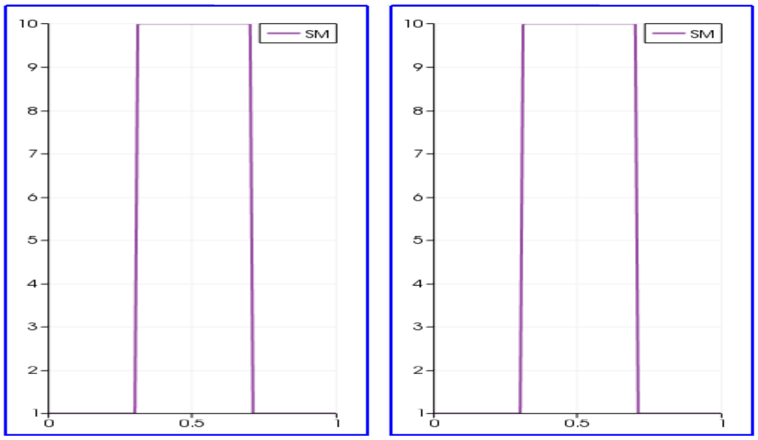

(c) Element-wise defined material coarse mesh (d) Element-wise defined material fine mesh

Figure 3.3 Target shear modulus distribution along the horizontal centerline

The effect of using these two different material discretization schemes is analyzed with respect to the strain. Figure 3.4 represents the calculated strain in continuously and element-wise defined materials using both coarse and fine mesh. In Figure 3.4, the inclusion is sort of visible in the strain images. But there are also other patterns in the strain image, which may cause misleading interpretations when screening for diseased tissues in real medical applications. Thus, strain imaging has limited applicability to detect diseased tissues.

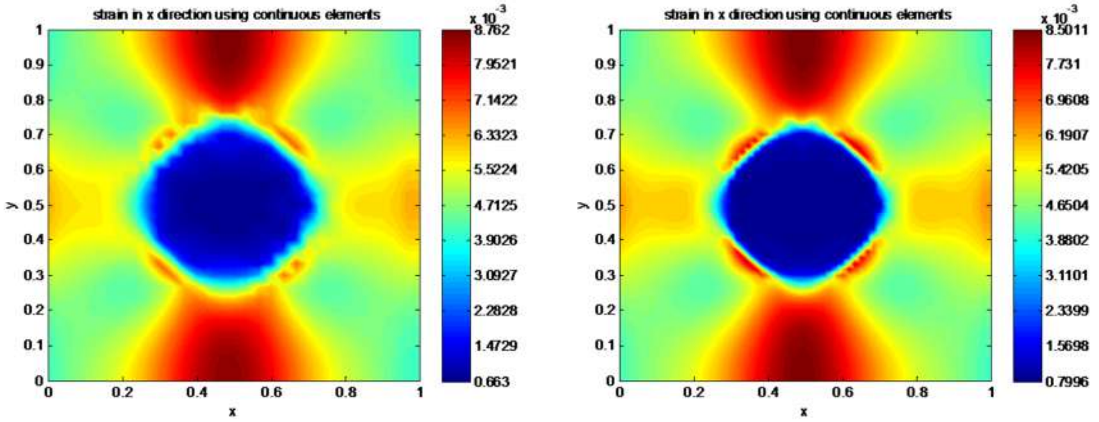

(a) Continuously defined material in coarse mesh (b) Continuously defined material in fine mesh

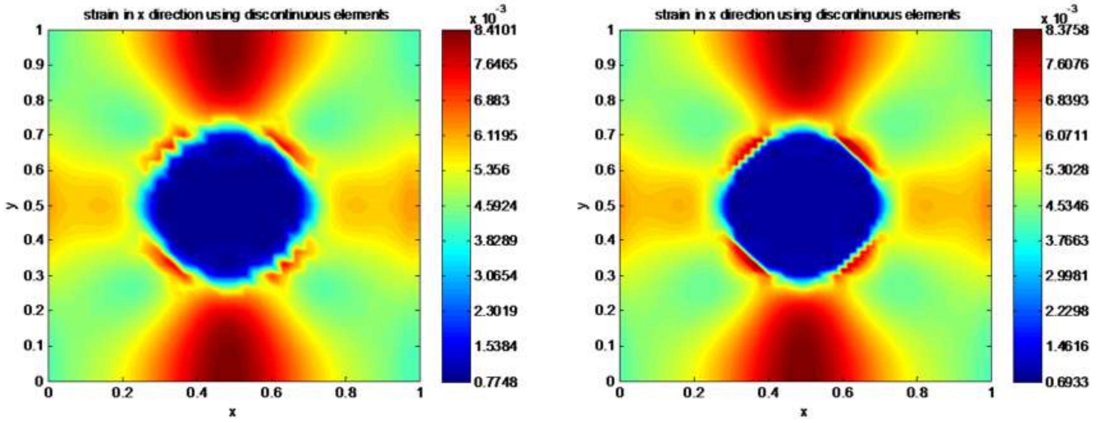

(c) Element-wise defined material in coarse mesh (d) Element-wise defined material in fine mesh

Figure 3.4 Horizontal Strain Visualization

Next, a total relative strain difference Δe is defined to compare the strain difference obtained from the continuously and element-wise defined shear modulus distribution.

$$\Delta e = \frac{\sqrt{\sum_{i=1}^{\#nodes}\left(e_{x\,i}^{n} - e_{x\,i}^{e}\right)^{2}}}{\sqrt{\sum_{i=1}^{\#nodes}\left(e_{x\,i}^{e}\right)^{2}}} \tag{3.1}$$

where $e_{x\,i}^{n}$ is the horizontal strain at the ith node using continuously defined material, e_{xi}^{e} is the horizontal strain at the ith node using element-wise defined material. This total relative strain difference between the continuously and element-wise defined materials decreases from 7.63% to 4.72% when the mesh is refined. Further a relative spatial strain difference between the continuously and element-wise defined shear modulus is shown in Figure 3.5 for a coarse and fine mesh. The spatial difference is defined as follows:

$$spatial\ difference = \frac{e_{x\,i}^{n} - e_{x\,i}^{e}}{e_{xi}^{e}} \tag{3.2}$$

From Figure 3.5, it is observed that the maximum spatial difference occurs at the border of inclusion and background. The maximum spatial difference decreases slightly with mesh refinement from 72% to 62%. This observation is highly important, as the strain will affect the stress in the same order. Thus, a stress analysis could be underestimated or overestimated by about 60%-70% if the shear modulus is not properly discretized.

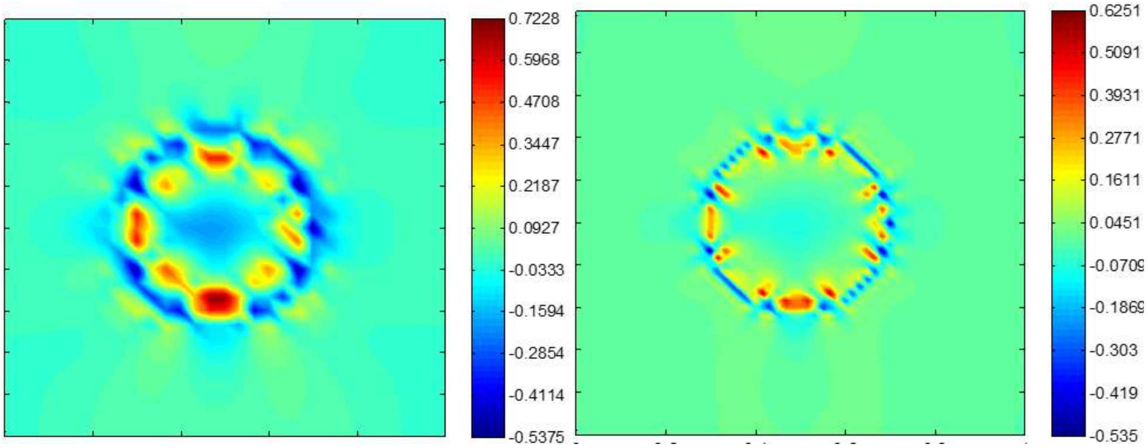

(a) coarse mesh (b) fine mesh

Figure 3.5 Spatial difference in horizontal strain between different materials

3.1.2 Target Shear Modulus Distribution in Model 2

The second model is a ring model that could represent an artery model which has an inner radius of 1 and the ratio between the thickness and the outer radius is 0.15. Dirichlet boundary conditions are prescribed on the inner radius with a magnitude of one percent of the thickness. The outer surface of the model is assumed to be traction free. The model is shown in Figure 3.6. The shear modulus values for model 2 are given in Table 3.1.

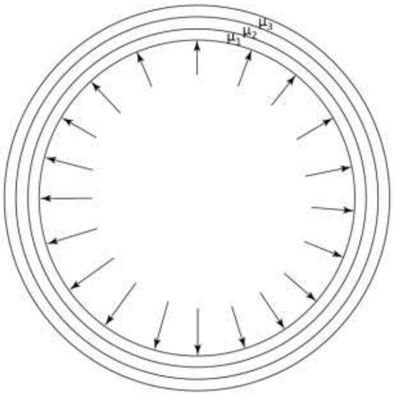

Figure 3.6. Model 2

Shear modulus	Homogeneous	Nonhomogeneous
μ_1	1	1
μ_2	1	5
μ_3	1	10

Table 3.1 Material properties

Figure 3.7 shows the target shear modulus distribution in both continuously and element-wise defined materials using a coarse mesh and a fine mesh. The coarse mesh has 720 bilinear elements and the fine mesh has 2880 bilinear elements. The corresponding target shear modulus distribution as a function of the thickness of the model along the horizontal centerline is shown in Figure 3.8. In Figure 3.8 (a), (b), the linear transition of the shear modulus occurs at the border between layers. This demonstrates that the material is continuously defined. While in Figure 3.8 (c) and (d), the discontinuous transition of the shear modulus occurs at the border of the layers. This demonstrates that the material is element-wise defined. As the mesh is refined (cf. (a), (b)), the linear transition of the shear modulus is getting closer to the discontinuous case.

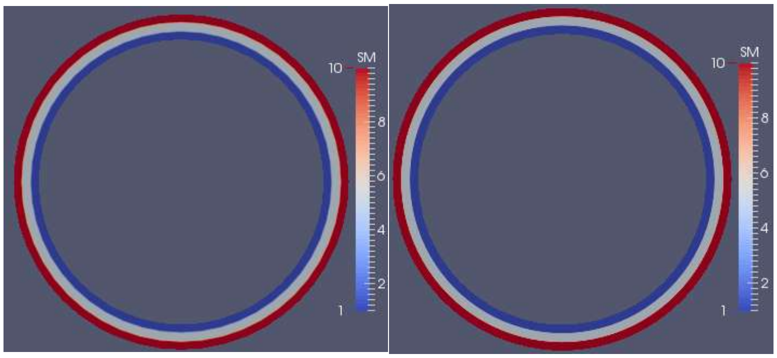

(a) Continuously defined material coarse mesh (b) Continuously defined material fine mesh

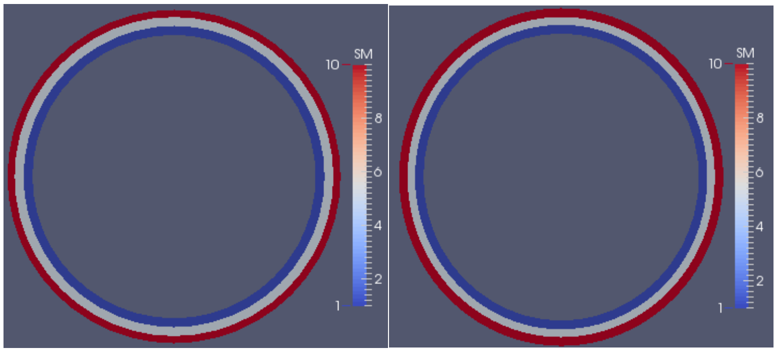

(c) Element-wise defined material coarse mesh (d) Element-wise defined material fine mesh

Figure 3.7 Target shear modulus distribution

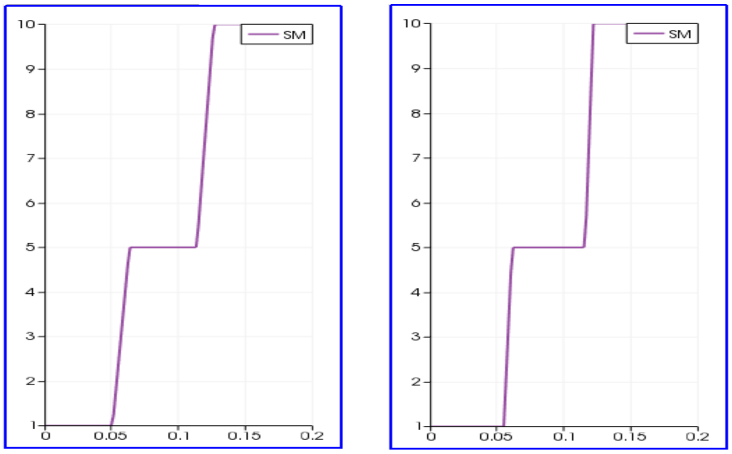

(a) Continuously defined material in coarse mesh
(b) Continuously defined material in fine mesh

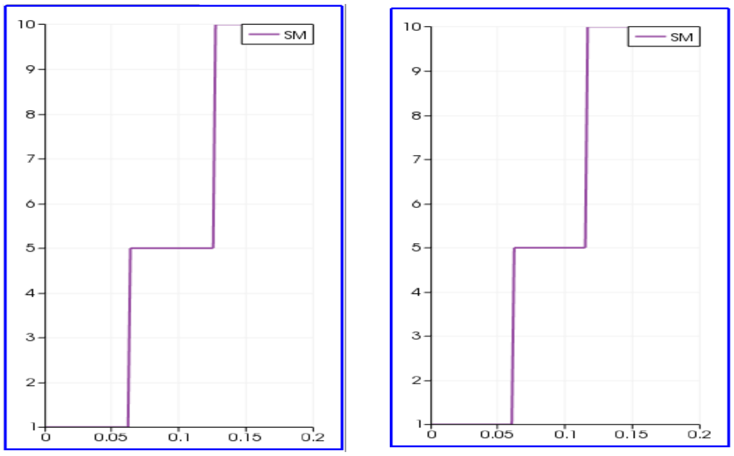

(c) Element-wise defined material coarse mesh
(d) Element-wise defined material fine mesh

Figure 3.8 Target shear modulus distribution as a function of thickness

The effect of using these two shear modulus discretization schemes is also compared for the radial strain. Figure 3.9 represents the calculated strain in continuously and element-wise defined materials using both coarse and fine mesh. It is observed that the difference between the radial strain with continuously and element-wise defined materials decreases when the mesh is refined by a factor of 2 along both the radial and circumferential direction.

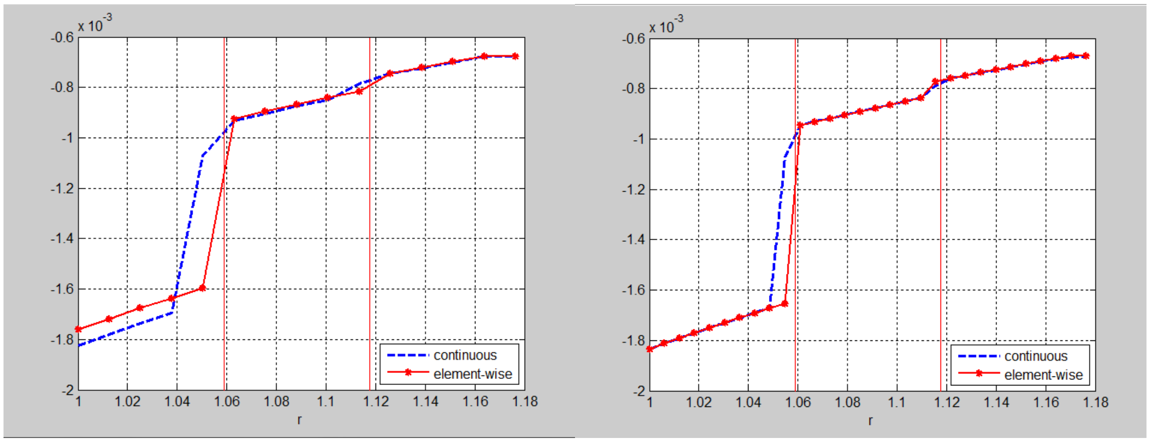

(a) radial strain in coarse mesh (b) radial strain in fine mesh

Figure 3.9 Radial strain with continuously and element-wise defined material

A total relative difference Δe is defined to compare the strain using continuously and element-wise defined materials.

$$\Delta e = \frac{\sqrt{\sum_{i=1}^{\#nodes} \left(e_{x\,i}^{n} - e_{x\,i}^{e}\right)^2}}{\sqrt{\sum_{i=1}^{\#nodes} \left(e_{x\,i}^{e}\right)^2}} \tag{3.3}$$

where $e_{x\,i}^{n}$ is the raidal strain at the i^th^ node using continuously defined material, e_{xi}^{e} is the radial strain at the i^th^ node using element-wise defined material. This total relative difference between the continuously and element-wise defined materials decreases from 11.97% to 8.83% when the mesh is refined. Further spatial difference is shown in Figure 3.10. The spatial difference is defined as follows:

$$spatial\ difference = \frac{e_{xi}^{n} - e_{xi}^{e}}{e_{xi}^{e}} \tag{3.4}$$

From Figure 3.10, it is observed that the maximum spatial difference occurs at the interface between the inclusion and background. The maximum spatial difference even increases slightly with mesh refinement from 32% to 35%. Again it is noted that these large strain differences will be inherited in the stresses. Thus, the stress computation could be off significantly if the shear modulus discretization does not represent the actual shear modulus discretization.

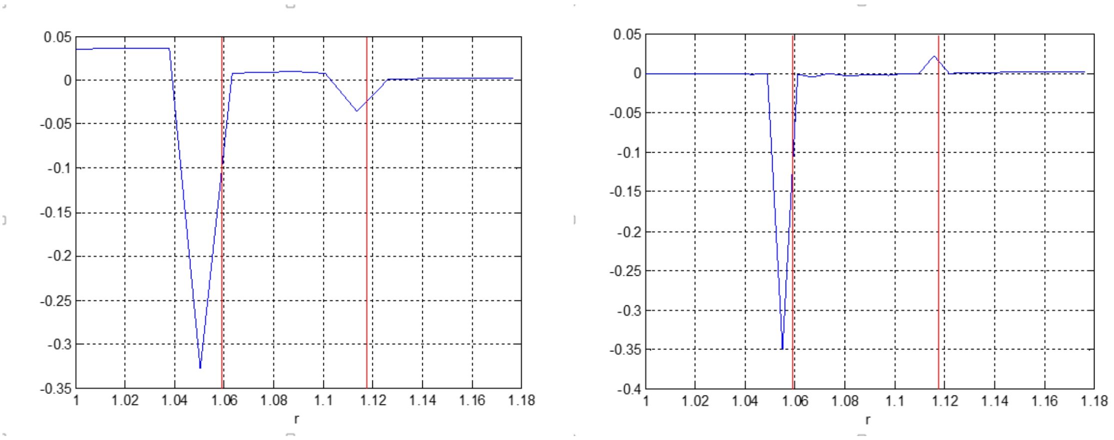

(a) coarse mesh (b) fine mesh

Figure 3.10 Spatial difference in radial strain between different materials

3.2 Strain Analysis in Forward Problem

The TVD regularization in the objective function contains a gradient operator acting on the shear modulus. This implies that for convenience of implementing the inverse algorithms, it is simpler to assume that the shear modulus distribution is continuous in the entire problem domain. However, if the actual shear modulus distribution is in fact discontinuous in the problem domain, a certain error will be committed. In this section, this reconstruction error will be studied for the hypothetical displacement fields obtained in section 3.1.

3.2.1 Shear Modulus Reconstruction in Model 1

3.2.1.1 Element-wise Defined Material with Noise Free Data

There is one inclusion in a homogeneous background for the shear modulus. The inclusion has the shear modulus value of 10 and the shear modulus in the background is unity. The measured displacement field is created by solving the forward problem as described in section 3.1. The same boundary conditions as described in section 3.1 for the forward problem are used to solve the inverse problem in this section. Both coarse and fine mesh are considered.

The reconstruction of the shear modulus using the inclusion model is given in Figure 3.11and 3.14 using coarse and fine mesh, respectively. The shear modulus will increase as the regularization parameter, α decreases. In Figure 3.11 (c) the reconstructed shear modulus ratio of inclusion to background approaches the exact value, 10, when the regularization parameter, α=2e-11. Figure 3.12 and 3.13 show the shear modulus value plotted along the horizontal and vertical lines through the center of the inclusions. In Figure 3.17 the relative error in shear modulus is visualized spatially. One can observe that the shear modulus is well recovered. The comparison between the exact and reconstructed value of the shear modulus along both the horizontal and vertical centerline in Figure 3.17 show that the reconstructed value is almost good except at the borders of the different material domains. The reason for this is that the gradient of the objective function will change continuously.

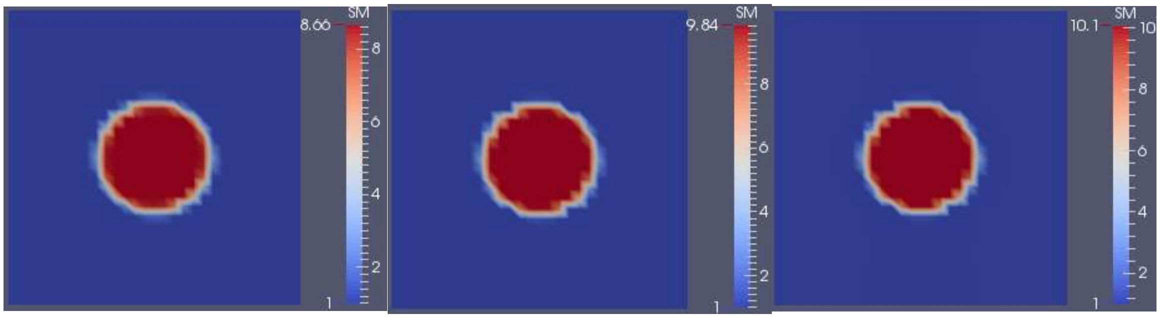

(a) α=1e-10 (b) α=3e-11 (c) α=2e-11

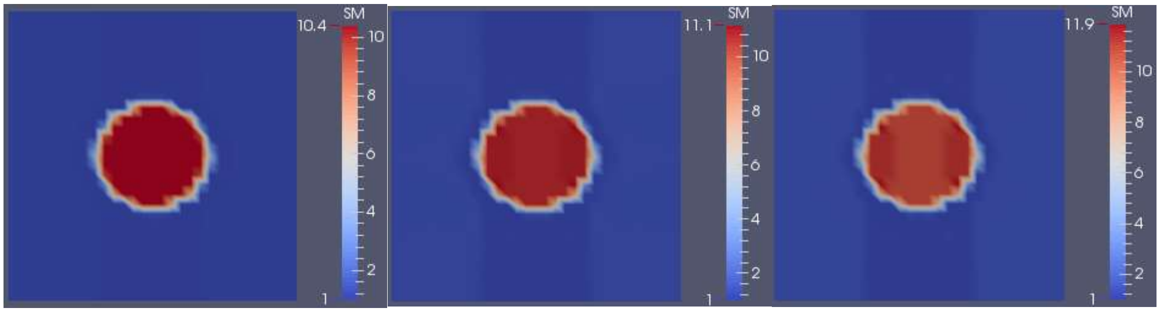

(d) α=1e-11 (e) α=4e-12 (f) α=3e-12

Figure 3.11 Shear modulus reconstruction from element-wise defined material with coarse mesh and noise free data

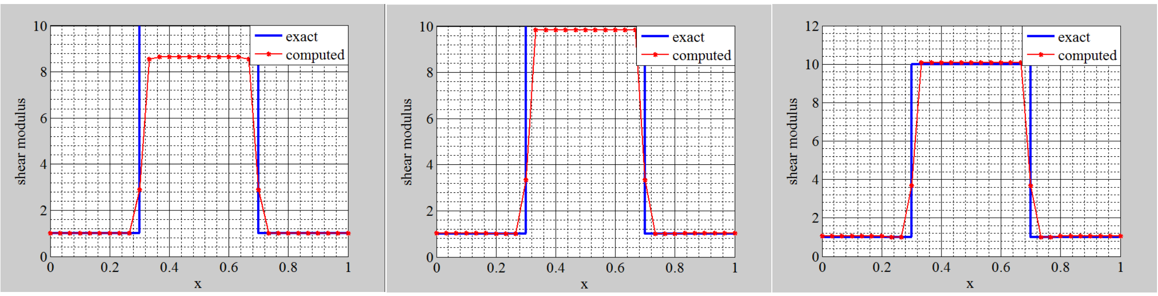

(a) α=1e-10 (b) α=3e-11 (c) α=2e-11

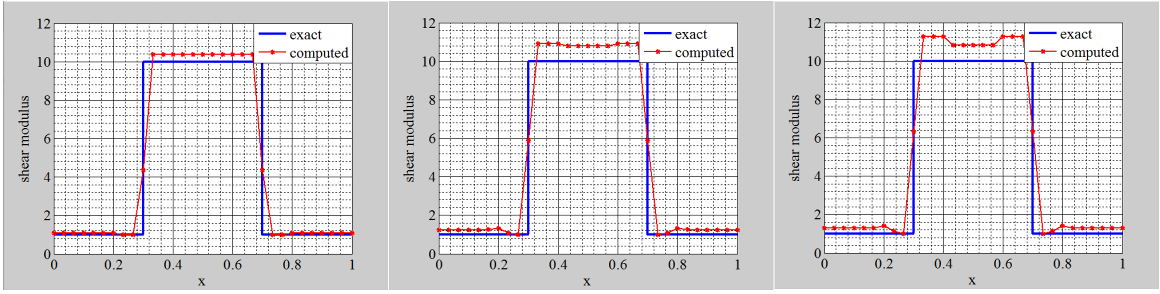

(d) α=1e-11 (e) α=4e-12 (f) α=3e-12

Figure 3.12 Shear modulus reconstruction from element-wise defined material with coarse mesh and noise free data along the horizontal centerline

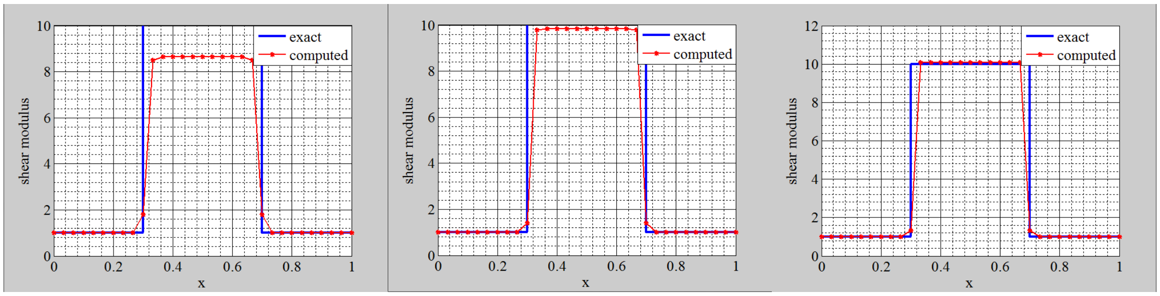

(a) α=1e-10 (b) α=3e-11 (c) α=2e-11

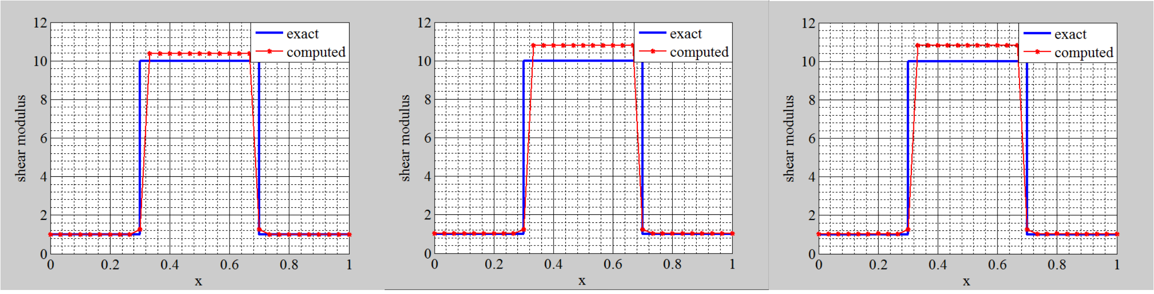

(d) α=1e-11 (e) α=4e-12 (f) α=3e-12

Figure 3.13 Shear modulus reconstruction from element-wise defined material with coarse mesh and noise free data along the vertical centerline

For the shear modulus reconstructions utilizing a fine mesh, Figure 3.14 shows the reconstruction of the shear modulus using the displacement field obtained from the element-wise defined shear modulus discretization with a fine mesh. In Figure 3.14 (d) the reconstructed shear modulus ratio of inclusion to background approaches the exact value, 10, when the regularization parameter, α=1e-11. Figure 3.15 and 3.16 show the shear modulus value plotted along the horizontal and vertical lines through the center of the inclusions. In Figure 3.18 the relative error in shear modulus is visualized spatially. One can observe that the shear modulus is well recovered. One can also observe that the shear modulus is reproduced very well with clear inclusion boundaries, even though its boundaries are very close to the domain boundaries.

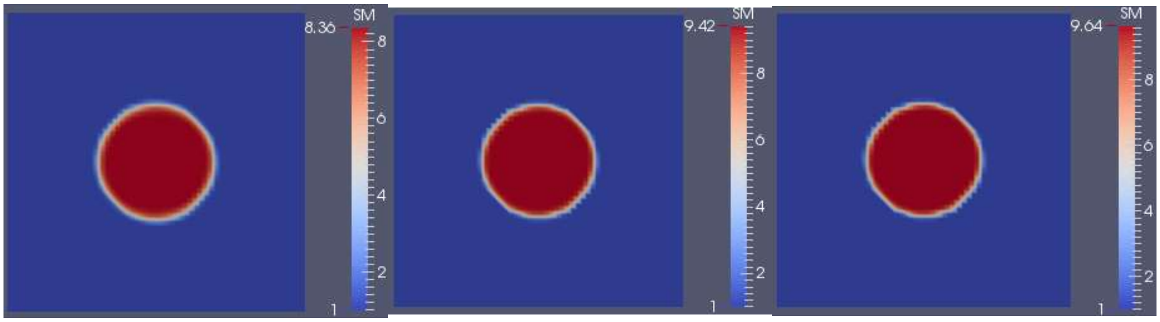

(a) α=1e-10 (b) α=3e-11 (c) α=2e-11

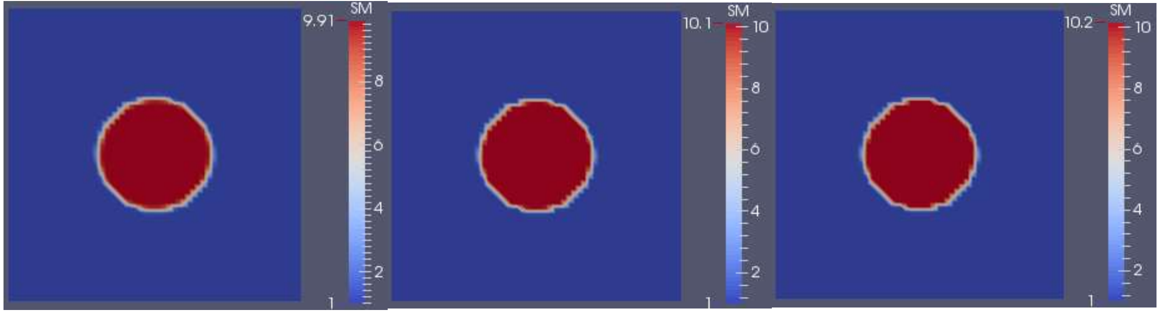

(d) α=1e-11 (e) α=4e-12 (f) α=3e-12

Figure 3.14 shear modulus reconstruction from element-wise defined material with fine mesh and noise free data

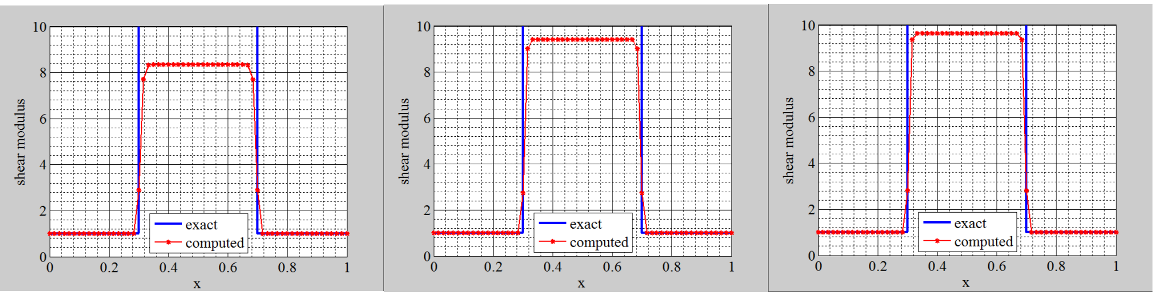

(a) α=1e-10 (b) α=3e-11 (c) α=2e-11

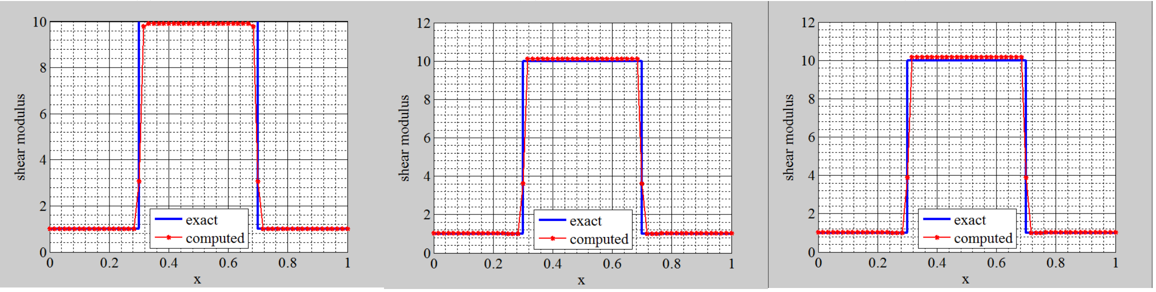

(d) α=1e-11 (e) α=4e-12 (f) α=3e-12

Figure 3.15 Shear modulus reconstruction from element-wise defined material with fine mesh and noise free data along the horizontal centerline

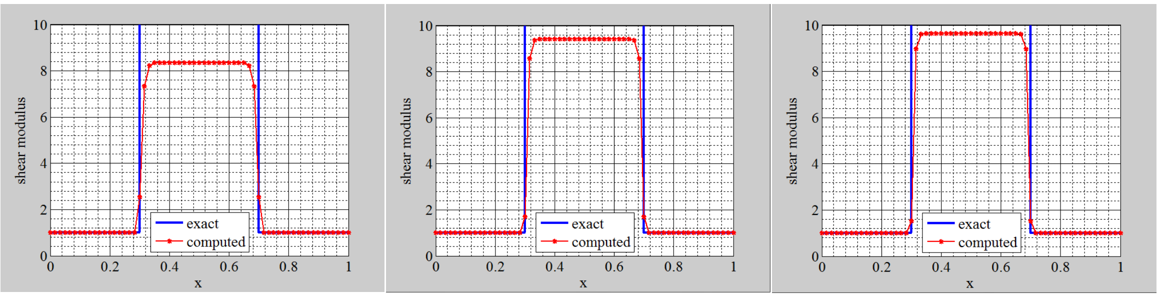

(a) α=1e-10 (b) α=3e-11 (c) α=2e-11

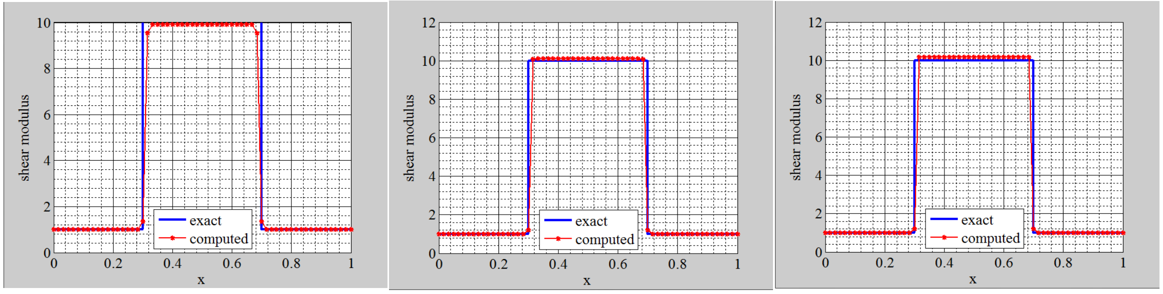

(d) α=1e-11 (e) α=4e-12 (f) α=3e-12

Figure 3.16 Shear modulus reconstruction from element-wise defined material with fine mesh and noise free data along the vertical centerline

The total relative error in the shear modulus reconstruction is defined here by

$$e_{\mu} = \sqrt{\frac{\sum_{i=1}^{\#nodes} \left(\mu_i^{exact} - \mu_i^{computed} \right)^2}{\sum_{i=1}^{\#nodes} \left(\mu_i^{exact} \right)^2}} \tag{3.5}$$

Also the relative spatial error in the shear modulus reconstruction is defined here by

$$relative\ spatial\ error = \frac{\mu_{x\,i}^{n} - \mu_{x\,i}^{e}}{\mu_{x\,i}^{e}} \tag{3.6}$$

In Figure 3.17 and 3.18, the relative spatial error in the shear modulus reconstruction is visualized for the coarse and fine mesh, respectively. One can observe that the largest error occurs at the interface between inclusion and background, which can be expected from the previous section. One can also observe that the relative spatial error for the coarse mesh is significantly higher than for the fine mesh. Thus, mesh refinement helps to reduce the relative spatial error as well as the relative total error in the shear modulus reconstruction.

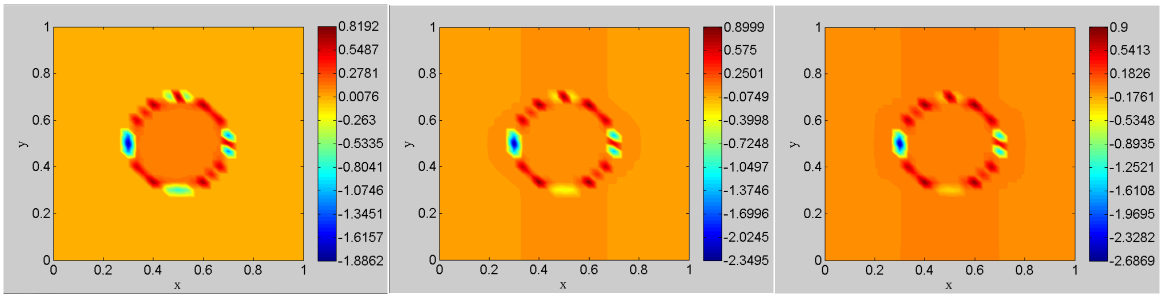

(a) α=1e-10
Relative error = 25.96%

(b) α=3e-11
Relative error = 24.69%

(c) α=2e-11
Relative error = 24.72%

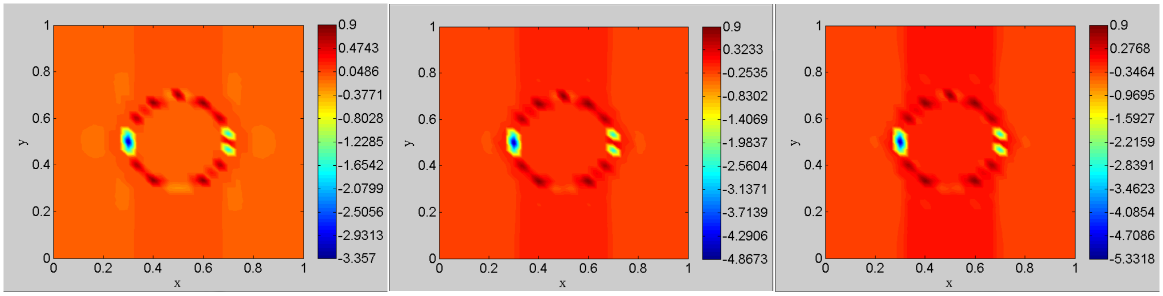

(d) α=1e-11
Relative error = 25.06%

(e) α=4e-12
Relative error = 25.99%

(f) α=3e-12
Relative error = 26.81%

Figure 3.17 Spatial error of the shear modulus reconstruction with a coarse mesh

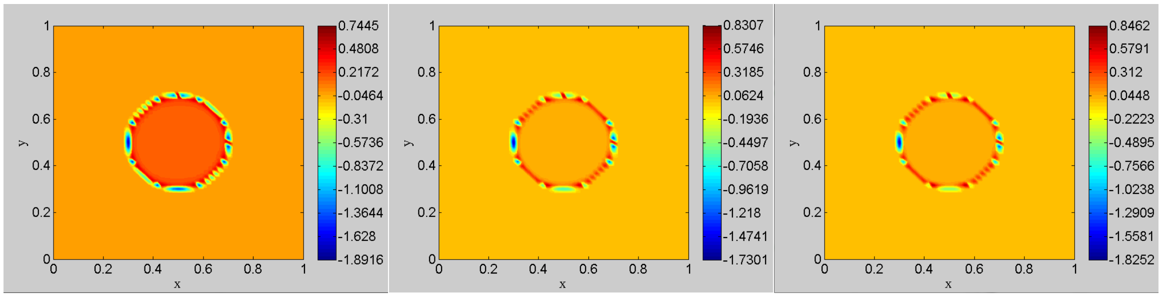

(a) α=1e-10
Relative error = 22.21%

(b) α=3e-11
Relative error = 15.58%

(c) α=2e-11
Relative error = 15.05%

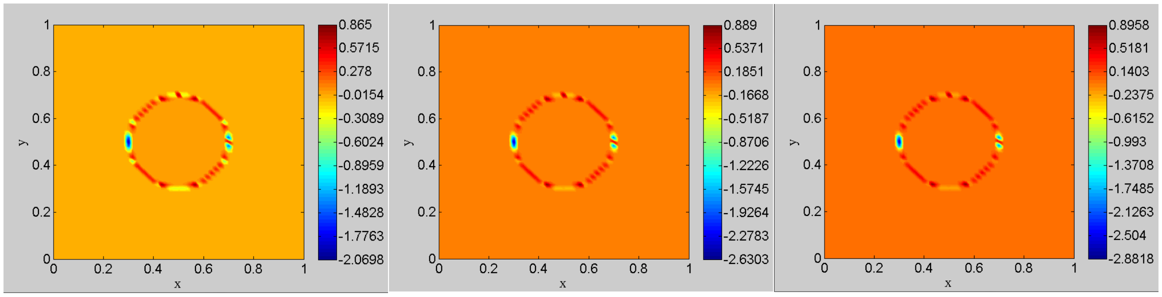

(d) α=1e-11
Relative error = 14.83%

(e) α=4e-12
Relative error = 14.79%

(f) α=3e-12
Relative error = 14.75%

Figure 3.18 Spatial error in the shear modulus reconstruction with a fine mesh

3.2.1.2 Continuously Defined Material with Noise Free Data

In the following, the inverse problem is solved utilizing the displacement data obtained from the continuously defined shear modulus distribution in the forward problem. No noise is added to the displacement data yet. For the coarse mesh in Figure 3.19 (d), the reconstructed shear modulus ratio of inclusion to background approaches the exact value, 10, when choosing the regularization parameter, α=1e-12. One can observe that the value of the shear modulus will stop increasing when the value approaches the exact value, 10. This is one difference from the reconstruction using the element-wise defined material. Figure 3.20 and 3.21 show the shear modulus value plotted along the horizontal and vertical centerline. In Figure 3.22 the relative error in shear modulus is visualized spatially. One can observe that the shear modulus is well recovered.

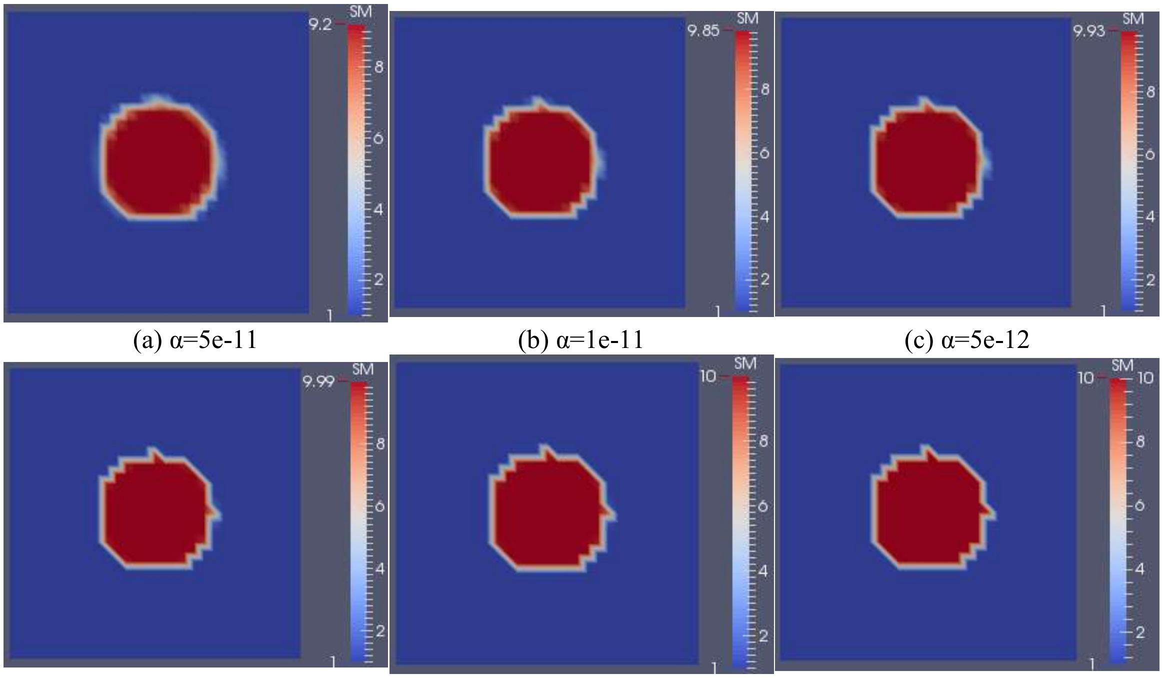

(a) α=5e-11 (b) α=1e-11 (c) α=5e-12

(d) α=1e-12 (e) α=5e-13 (f) α=1e-13

Figure 3.19 Shear modulus reconstruction from continuously defined material with coarse mesh and noise free data

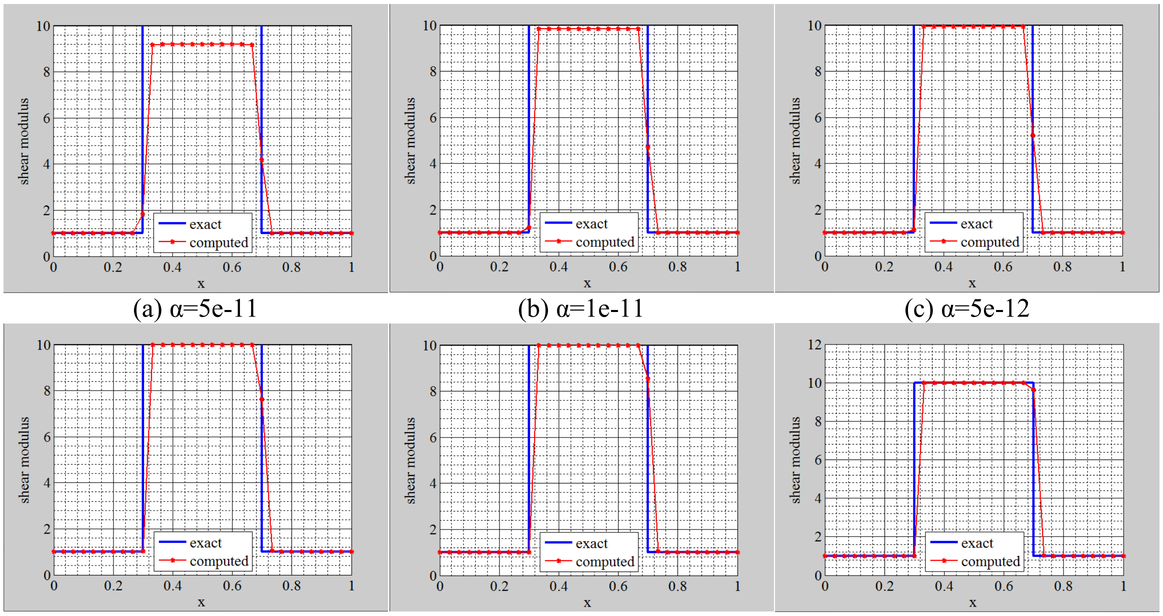

(a) α=5e-11 (b) α=1e-11 (c) α=5e-12

(d) α=1e-12 (e) α=5e-13 (f) α=1e-13

Figure 3.20 Shear modulus reconstruction from continuously defined material with coarse mesh and noise free data along the horizontal centerline

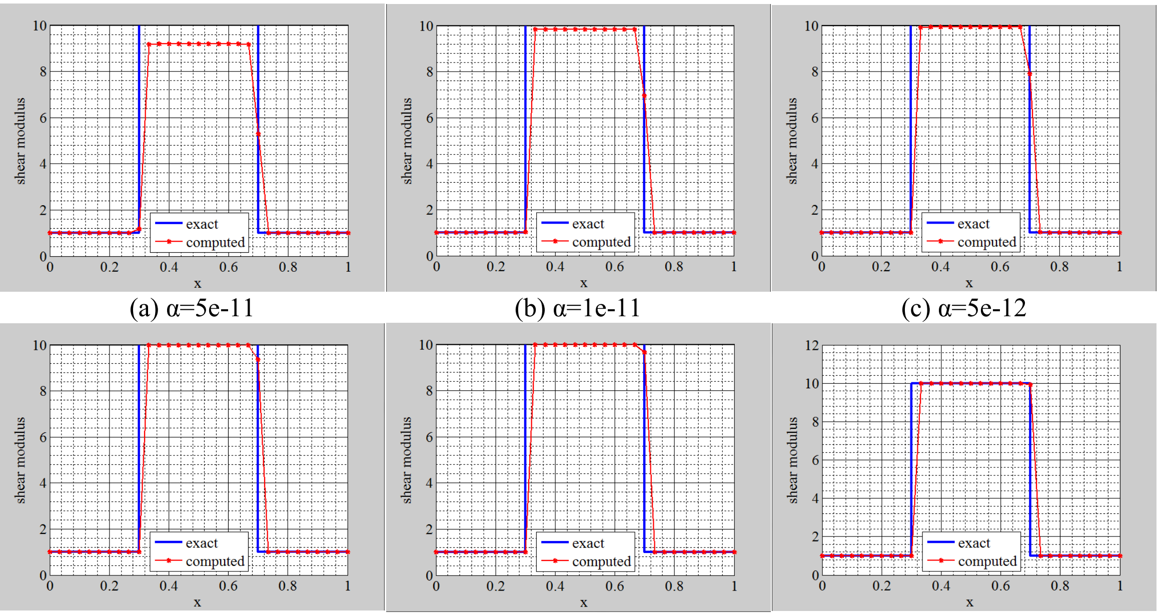

(a) α=5e-11 (b) α=1e-11 (c) α=5e-12

(d) α=1e-12 (e) α=5e-13 (f) α=1e-13

Figure 3.21 Shear modulus reconstruction from continuously defined material with coarse mesh and noise free data along the vertical centerline

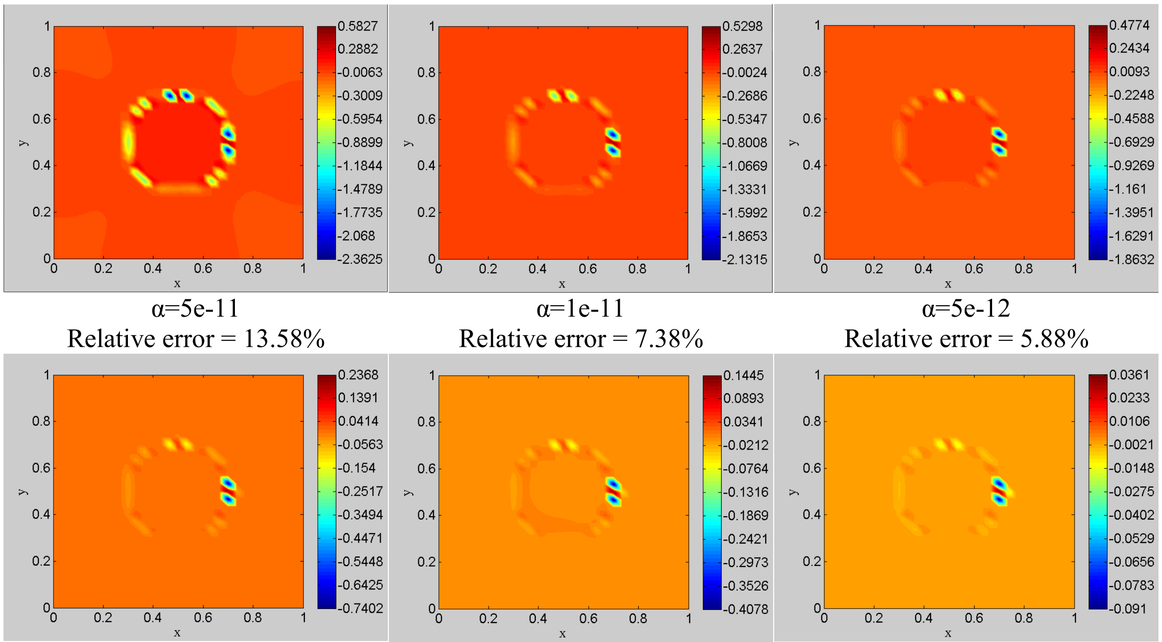

α=5e-11
Relative error = 13.58%

α=1e-11
Relative error = 7.38%

α=5e-12
Relative error = 5.88%

α=1e-12
Relative error = 2.54%

α=5e-13
Relative error = 1.51%

α=1e-13
Relative error = 0.37%

Figure 3.22 Spatial error in the shear modulus reconstruction with a coarse mesh

Figure 3.23 shows the reconstruction of the shear modulus using the displacement data from the continuously defined material with a fine mesh. One can observe that the value of the recovered shear modulus stops increasing when the value approaches the exact value, 10. Figure 3.24 and 3.25 show the shear modulus value plotted along the horizontal and vertical centerlines. In Figure 3.26 the relative error in the shear modulus is visualized spatially. Here, the relative error increases as the mesh is refined. It can be observed that the shear modulus is well recovered, i.e. the shear modulus is reproduced very well with clear inclusion boundaries. The total relative error and the maximum spatial error decrease when the mesh is refined (cf. Figure 3.22, 3.26).

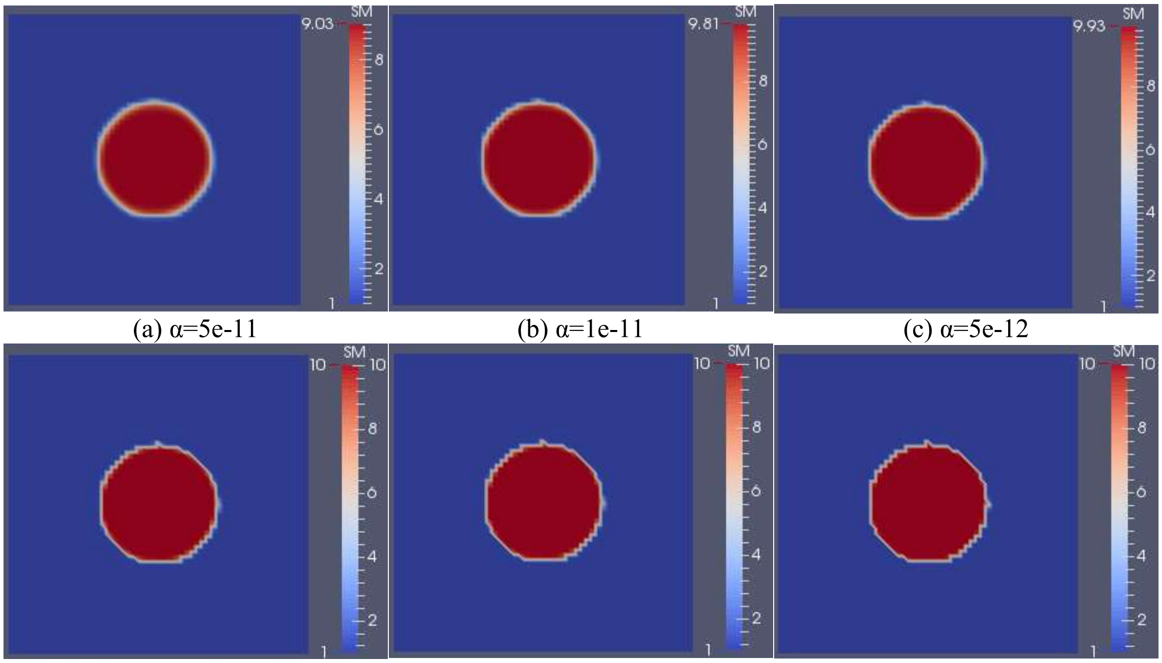

(a) α=5e-11 (b) α=1e-11 (c) α=5e-12

(d) α=1e-12 (e) α=5e-13 (f) α=1e-13

Figure 3.23 Shear modulus reconstruction from continuously defined material with fine mesh and noise free data

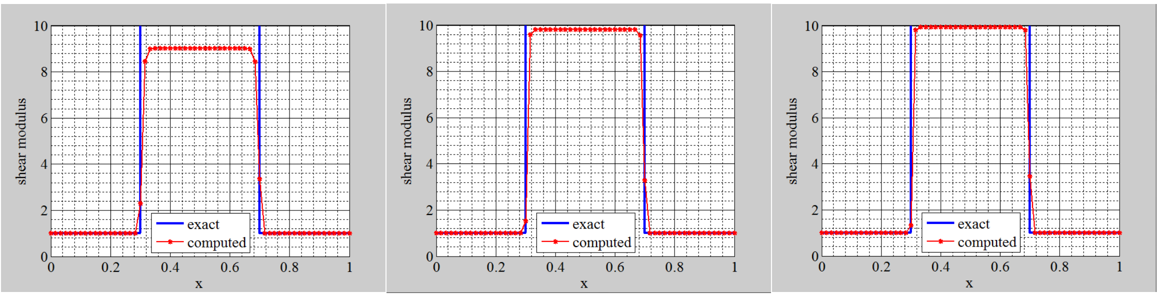

(a) α=5e-11 (b) α=1e-11 (c) α=5e-12

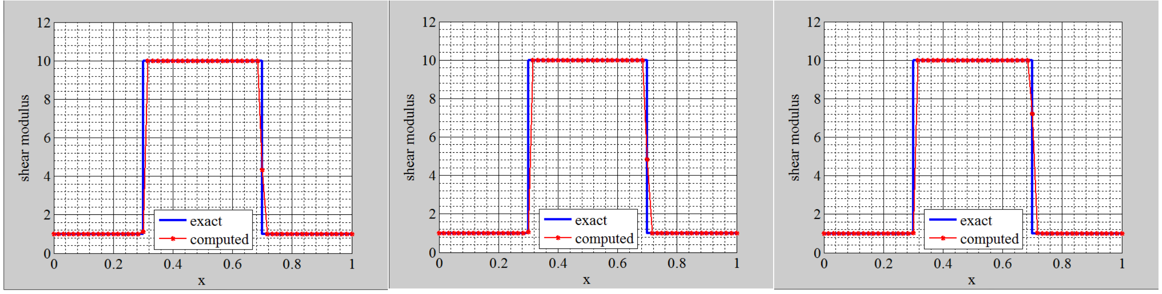

(d) α=1e-12 (e) α=5e-13 (f) α=1e-13

Figure 3.24 Shear modulus reconstruction from continuously defined material with fine mesh and noise free data along the horizontal centerline

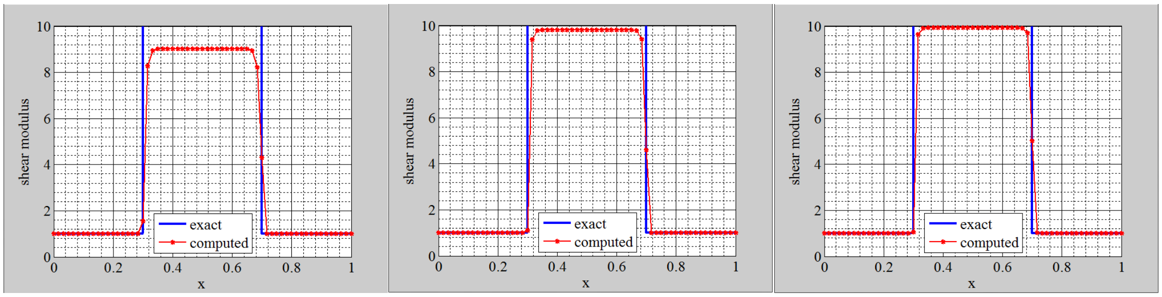

(a) α=5e-11 (b) α=1e-11 (c) α=5e-12

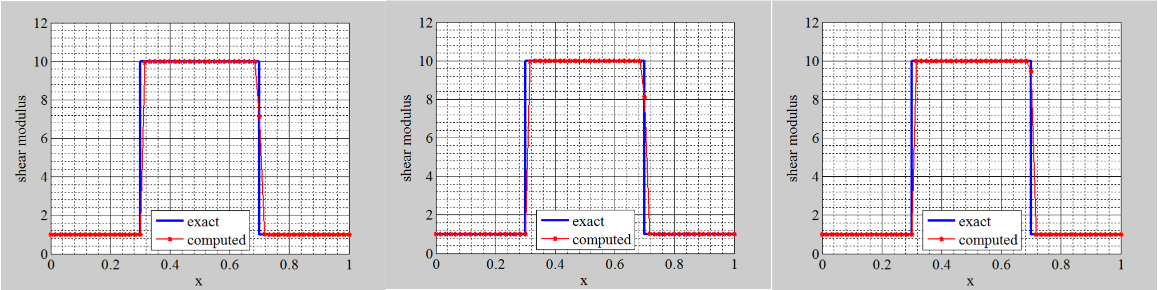

(d) α=1e-12 (e) α=5e-13 (f) α=1e-13

Figure 3.25 Shear modulus reconstruction from continuously defined material with fine mesh and noise free data along the vertical centerline

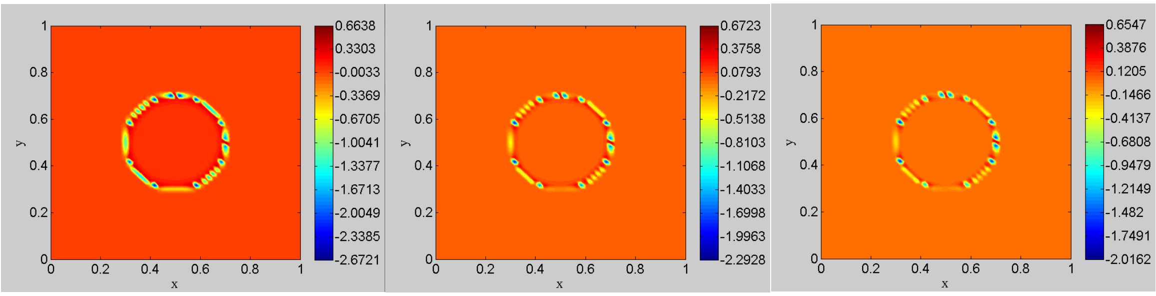

α=5e-11 α=1e-11 α=5e-12

Relative error = 15.92% Relative error = 9.51% Relative error = 7.87%

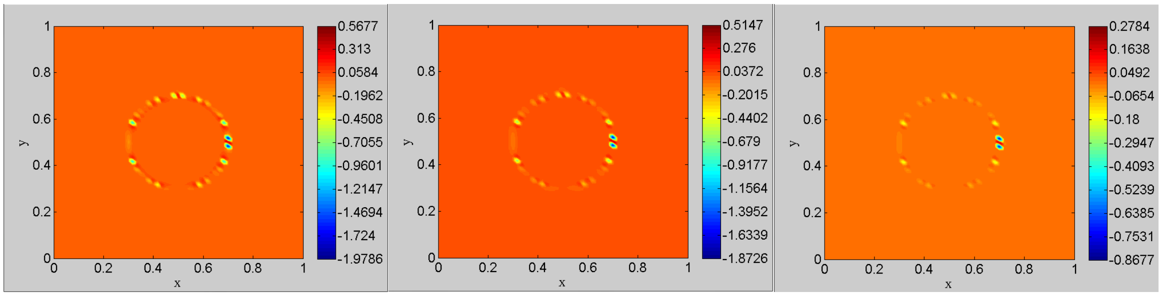

α=1e-12 α=5e-13 α=1e-13

Relative error = 4.68% Relative error = 3.63% Relative error = 1.57%

Figure 3.26 Spatial error in the shear modulus reconstruction with a fine mesh

3.2.1.3 Element-wise Defined Material with Noised Data

Thereafter noise is added to the displacement field to simulate the hypothetical 'measured' displacement and use these in the inverse solver to reconstruct the spatial distribution of the material properties. These reconstructions are compared with the original distributions in order to assess the performance of this approach. About 1% and 3% white Gaussian noise are added to the displacement data to simulate noisy experimental data. For 1% noise the shear modulus reconstruction is plotted in Figure 3.27 for different regularization factors. The regularization parameter α=1e-10, appears to yield an optimal shear modulus reconstruction in terms of the smoothness and contrast of inclusion to background as well as the shape of the inclusion. It can be observed that the shear modulus reconstructions are in good agreement with the exact distributions. In order to visualize the change of the shear modulus at the interface of inclusion and background, Figure 3.28 and 3.29 are provided, where the reconstructed shear modulus is plotted along both, the horizontal and vertical centerlines. The relative spatial error is plotted in the Figure 3.30. One can observe that the maximum relative spatial error occurs at the border of the inclusion and the background.

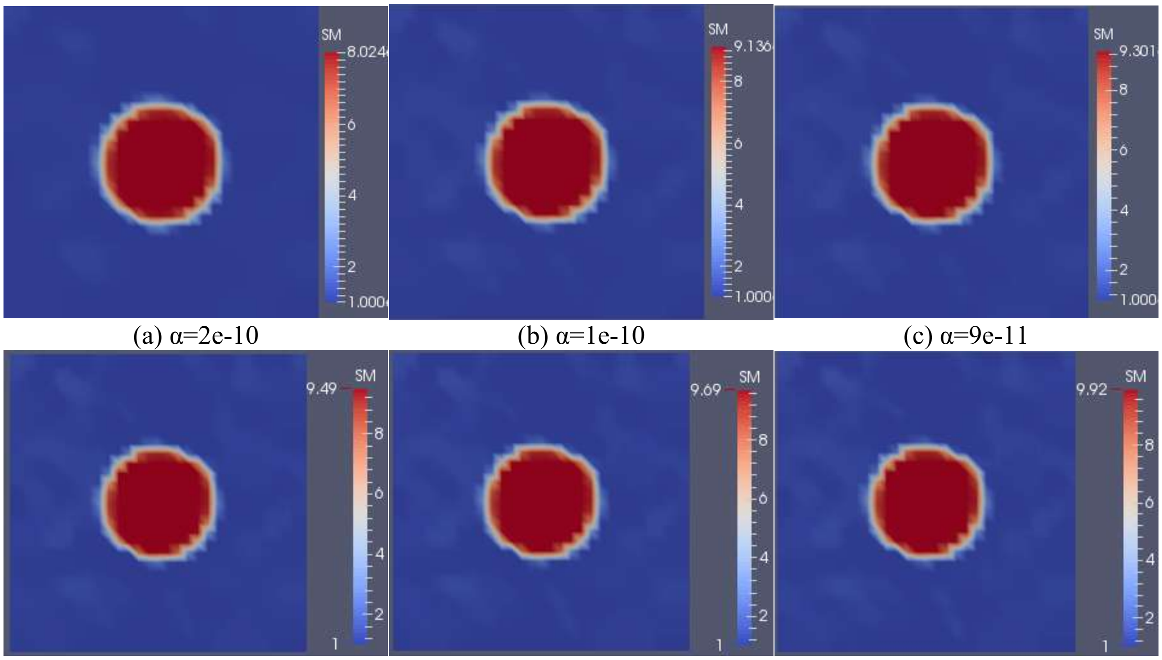

(a) α=2e-10 (b) α=1e-10 (c) α=9e-11

(d) α=8e-11 (e) α=7e-11 (f) α=6e-11

Figure 3.27 Shear modulus reconstruction from element-wise defined material with coarse mesh and 1% noise

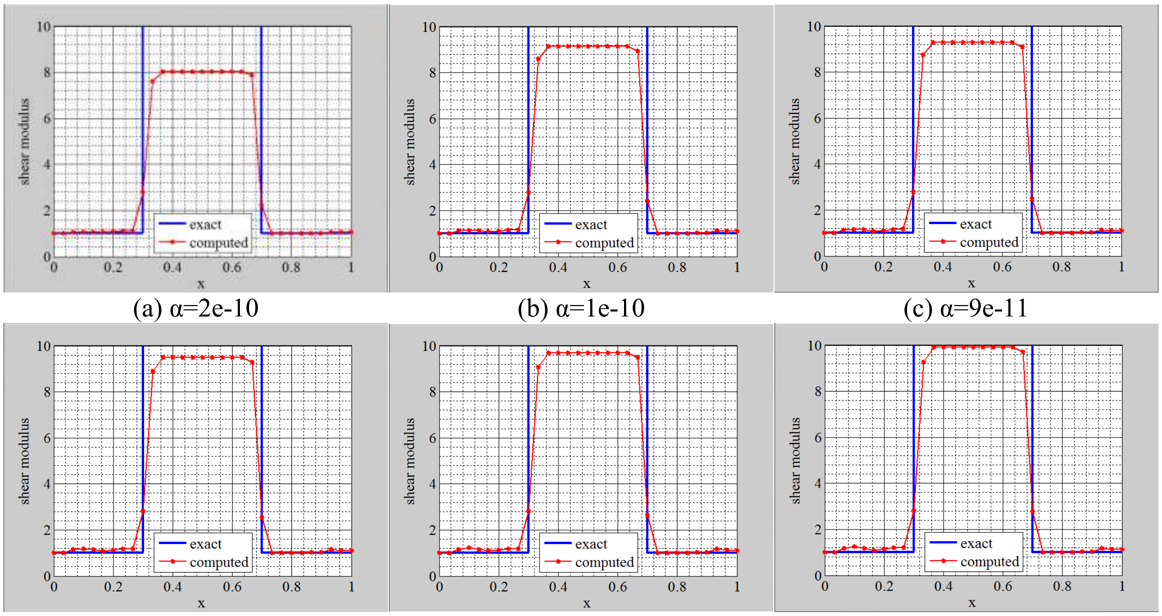

(a) α=2e-10 (b) α=1e-10 (c) α=9e-11

(d) α=8e-11 (e) α=7e-11 (f) α=6e-11

Figure 3.28 Shear modulus reconstruction from element-wise defined material with coarse mesh and 1% noise along the horizontal centerline

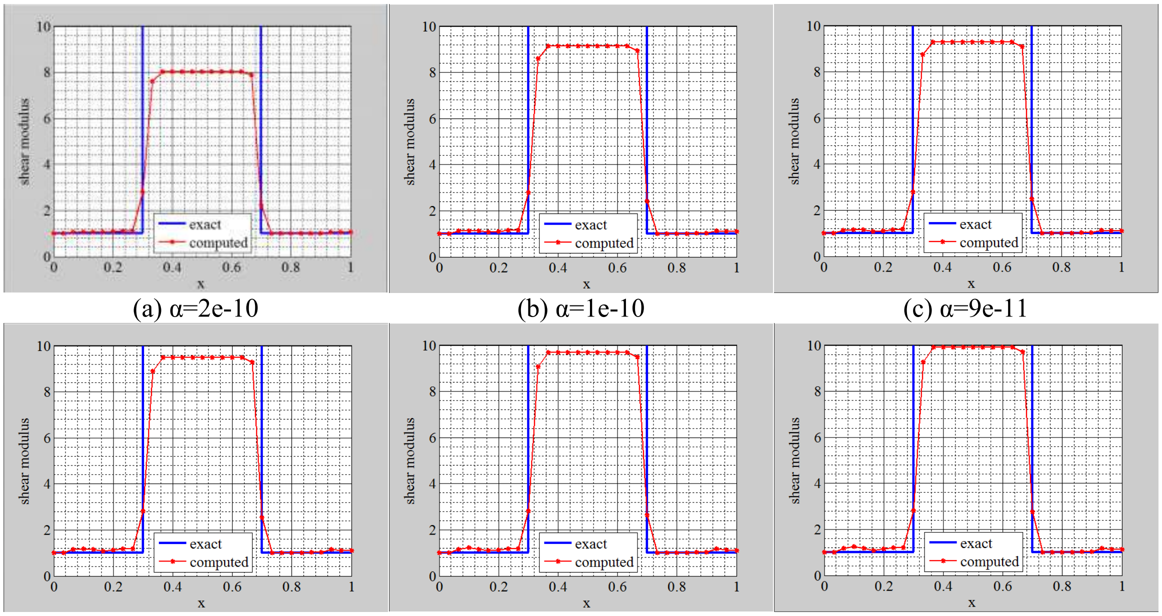

(a) α=2e-10 (b) α=1e-10 (c) α=9e-11

(d) α=8e-11 (e) α=7e-11 (f) α=6e-11

Figure 3.29 Shear modulus reconstruction from element-wise defined material with coarse mesh and 1% noise along the vertical centerline

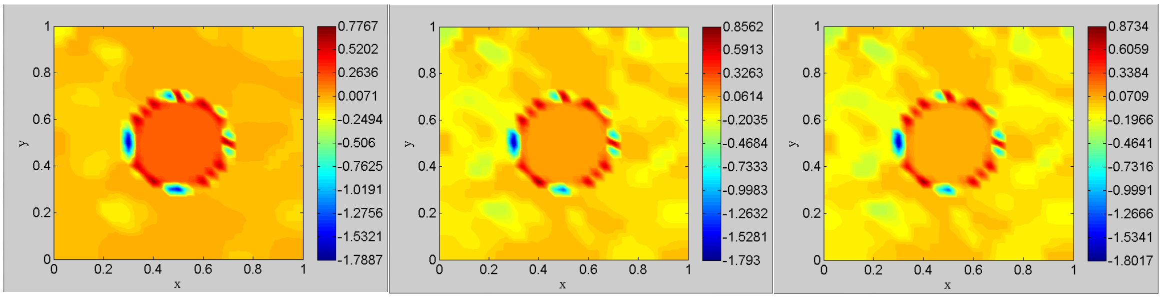

(a) α=2e-10
Relative error = 28.62%

(b) α=1e-10
Relative error = 24.54%

(c) α=9e-11
Relative error = 24.21%

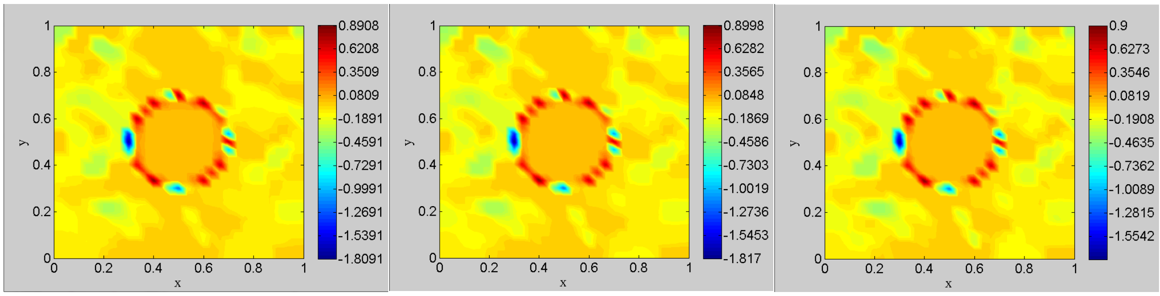

(d) α=8e-11
Relative error = 23.93%

(e) α=7e-11
Relative error = 23.72%

(f) α=6e-11
Relative error = 23.63%

Figure 3.30 Spatial error of the shear modulus with a coarse mesh and 1% noise in the displacement field

In the following, the shear modulus will be reconstructed for the displacement data with 3% white Gaussian noise. In Figure 3.31 it can be observed that reconstructions are not in good agreement with the exact distributions. The shape of the inclusion is not well recovered and the background is not homogeneous. In order to visualize the change of the shear modulus in the border of the inclusion and the background, Figure 3.32 and 3.33 show the reconstruction of the recovered shear modulus in both the horizontal and vertical direction along the centerline. The relative spatial error is plotted in Figure 3.34. The total relative error as well as the relative spatial error increases with increasing noise level (cf. Figure 3.30, 3.34).

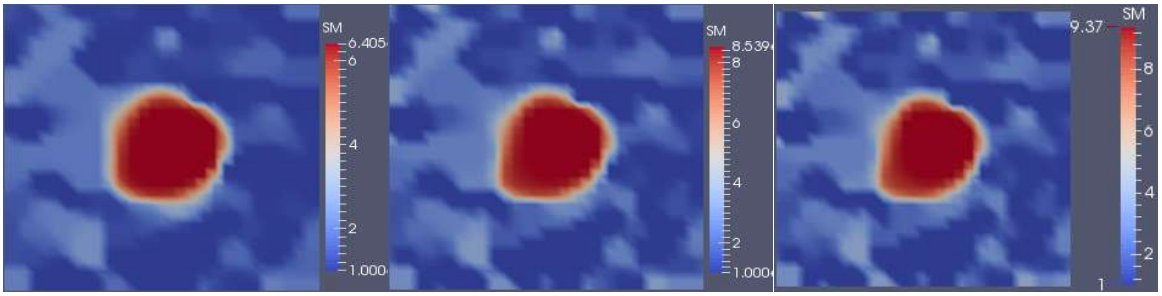

(a) α=1e-9 (b) α=5e-10 (c) α=4e-10

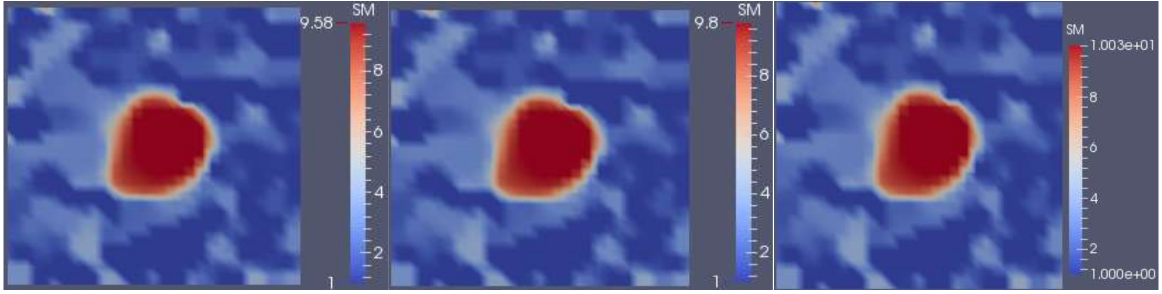

(d) α=3.8e-10 (e) α=3.6e-10 (f) α=3.4e-10

Figure 3.31 Shear modulus reconstruction from element-wise defined material with coarse mesh and 3% noise

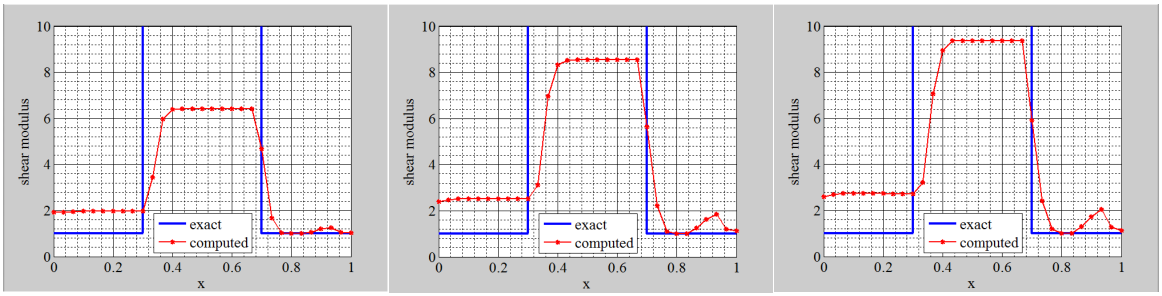

(a) α=1e-9 (b) α=5e-10 (c) α=4e-10

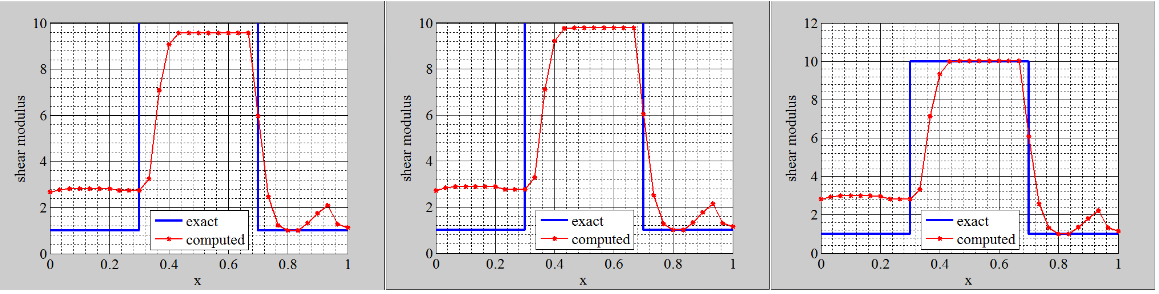

(d) α=3.8e-10 (e) α=3.6e-10 (f) α=3.4e-10

Figure 3.32 Shear modulus reconstruction from element-wise defined material with coarse mesh and 3% noise along the horizontal centerline

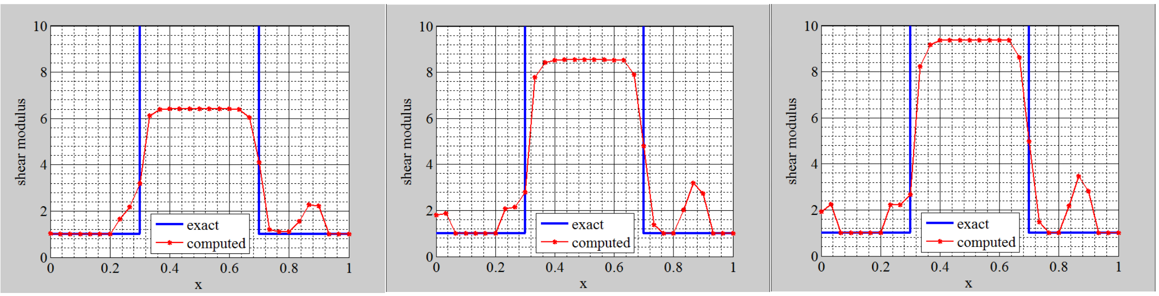

(a) α=1e-9 (b) α=5e-10 (c) α=4e-10

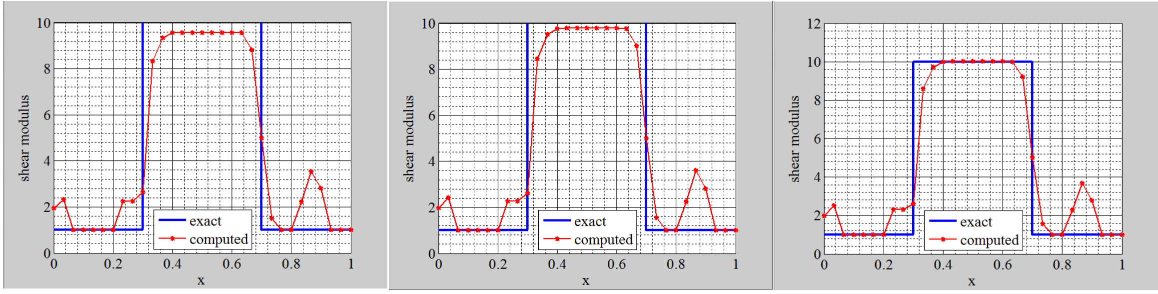

(d) α=3.8e-10 (e) α=3.6e-10 (f) α=3.4e-10

Figure 3.33 Shear modulus reconstruction from element-wise defined material with coarse mesh and 3% noise along the vertical centerline

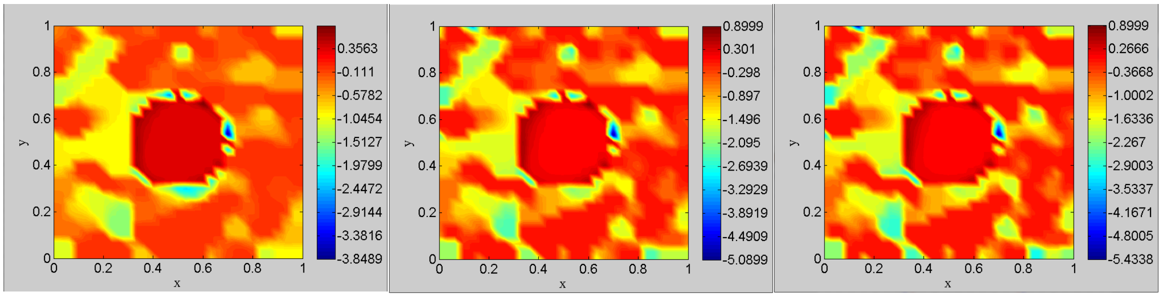

(a) α=1e-9
Relative error = 44.62%

(b) α=5e-10
Relative error = 39.61%

(c) α=4e-10
Relative error = 40.75%

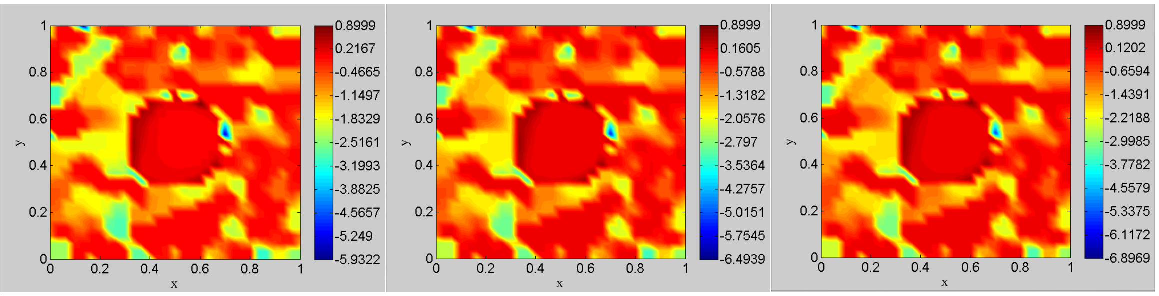

(d) α=3.8e-10
Relative error = 41.30%

(e) α=3.6e-10
Relative error = 42.00%

(f) α=3.4e-10
Relative error = 42.85%

Figure 3.34 Relative spatial error with a coarse mesh and 3% noise in the displacement field

Next, the same will be analyzed for the fine mesh model. Figure 3.35 shows the reconstruction of the shear modulus using "measured" displacement data with 1% white Gaussian noise level, where the actual target shear modulus distribution is discontinuous between the inclusion and background interface. One can observe that the shear modulus reconstruction is much better than the reconstruction with the coarse mesh. Figure 3.36 and 3.37 show the shear modulus value plotted along the horizontal and vertical centerlines. In Figure 3.38 the relative error in the shear modulus is visualized spatially. Here, the relative error does not change much as the mesh is refined, because the reconstruction is well recovered and the convergence is reached. One can also observe that the shear modulus is reproduced very well with clear inclusion boundaries, even though its boundaries are very close to the domain boundaries. Still, the maximum error occurs at the border of the inclusion and the background (see Figure 3.38).

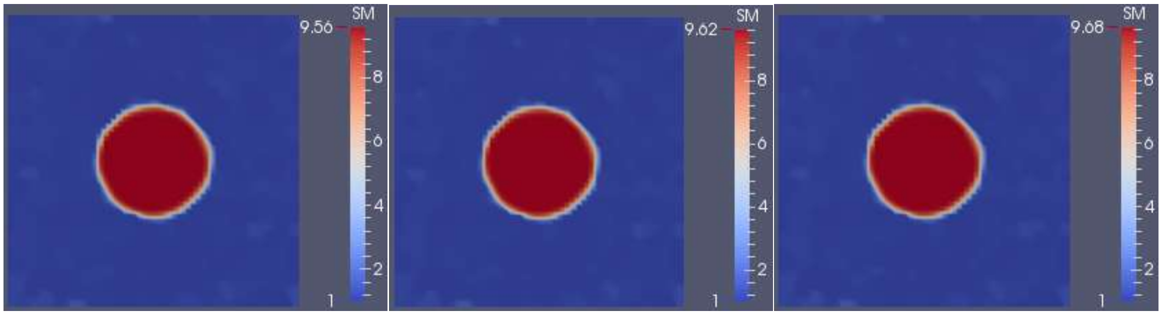

(a) α=4e-11 (b) α=3.8e-11 (c) α=3.6e-11

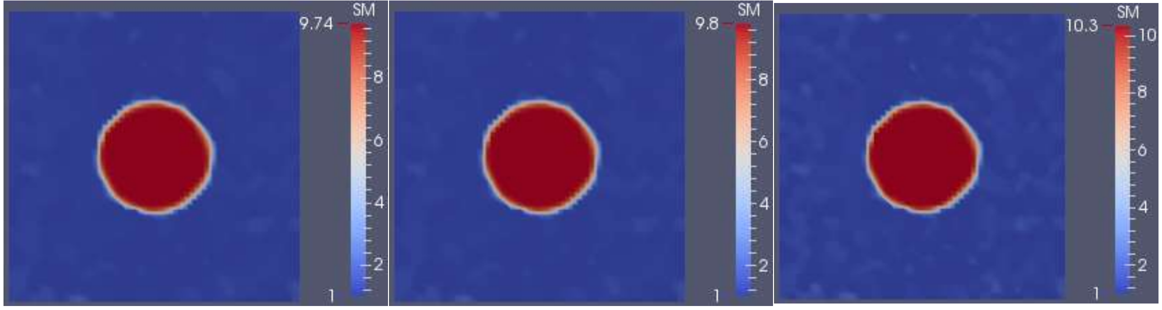

(d) α=3.4e-11 (e) α=3.2e-11 (f) α=3e-11

Figure 3.35 Shear modulus reconstruction from element-wise defined material with fine mesh and 1% noise

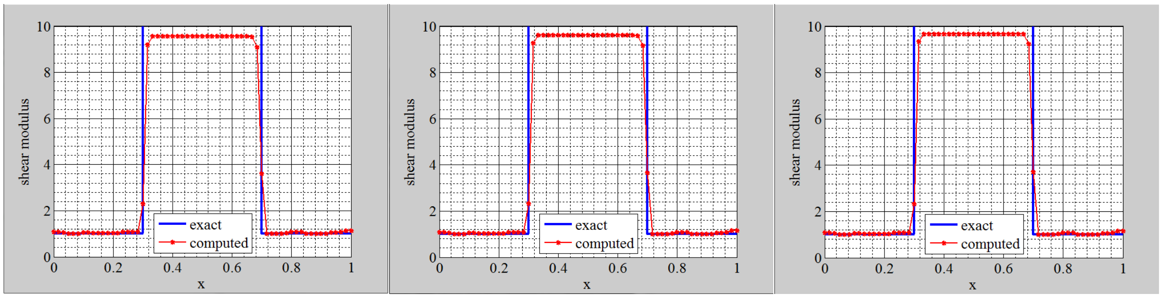

(a) α=4e-11 (b) α=3.8e-11 (c) α=3.6e-11

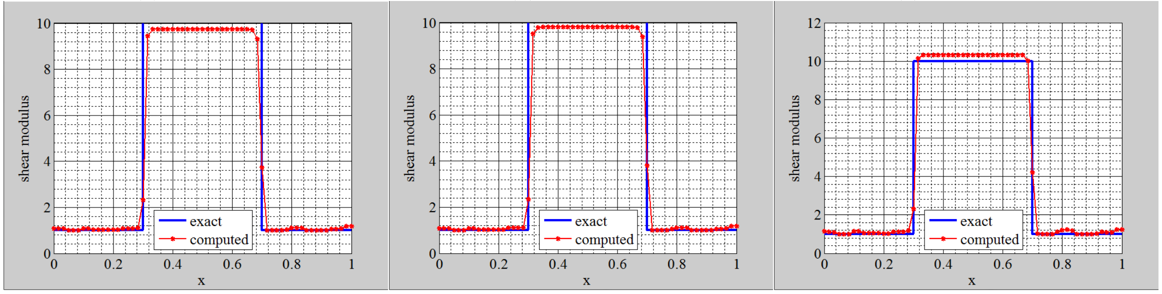

(d) α=3.4e-11 (e) α=3.2e-11 (f) α=3e-11

Figure 3.36 Shear modulus reconstruction from element-wise defined material with fine mesh and 1% noise along the horizontal centerline

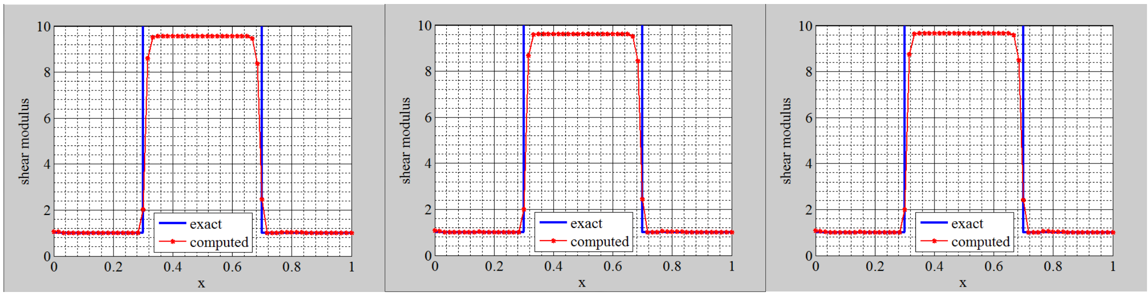

(a) α=4e-11 (b) α=3.8e-11 (c) α=3.6e-11

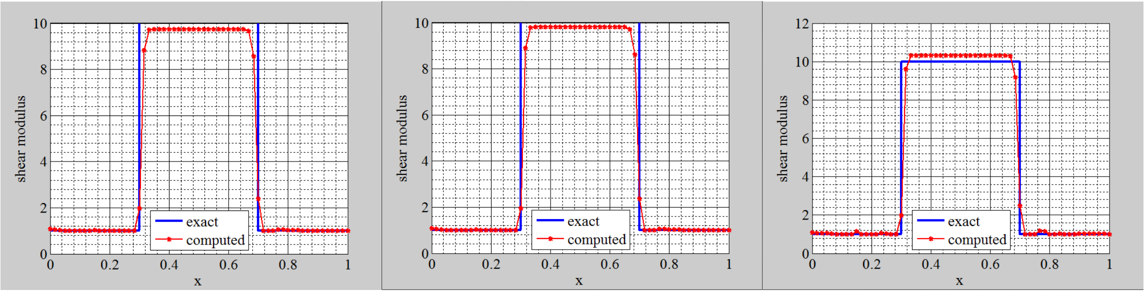

(d) α=3.4e-11 (e) α=3.2e-11 (f) α=3e-11

Figure 3.37 Shear modulus reconstruction from element-wise defined material with fine mesh and 1% noise along the vertical centerline

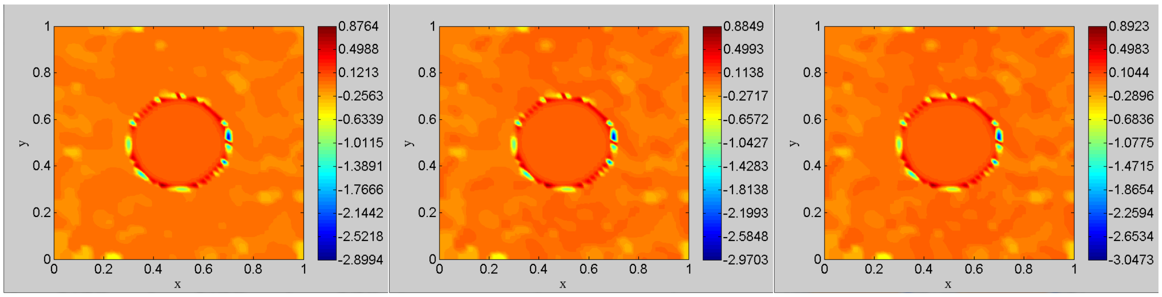

(a) α=4e-11
Relative error = 16.10%

(b) α=3.8e-11
Relative error = 15.94%

(c) α=3.6e-11
Relative error = 15.80%

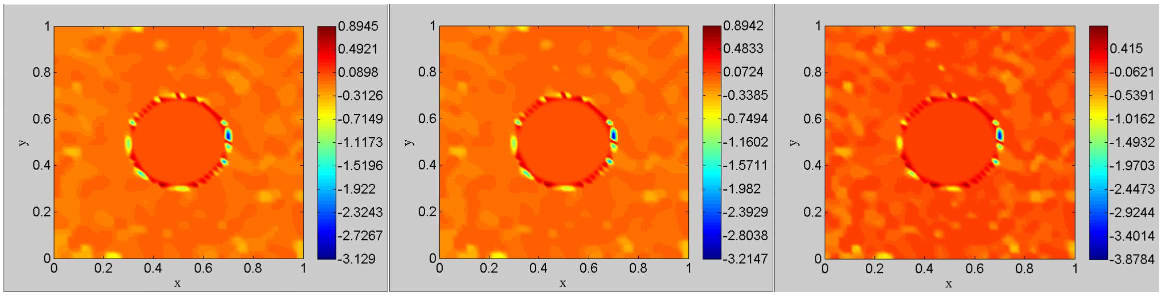

(d) α=3.4e-11
Relative error = 15.68%

(e) α=3.2e-11
Relative error = 15.57%

(f) α=3e-11
Relative error = 15.73%

Figure 3.38 Relative spatial error with a fine mesh and 1% noise in the displacement field

For 3% noise in the displacement field the shear modulus is plotted in Figure 3.39 for different regularization factors. The regularization parameter α=3e-10 appears to yield a proper shear modulus reconstruction based on the smoothness criteria. It can be observed that reconstructions are not in good agreement with the exact distributions. The border of inclusion and background is not well recovered. In order to illustrate the change of the shear modulus in the border of the inclusion and the background, Figure 3.40 and 3.41 show the reconstruction of the shear modulus in both the horizontal and vertical direction along the centerline. The relative spatial error is plotted in Figure 3.42 for different choices of the regularization factor.

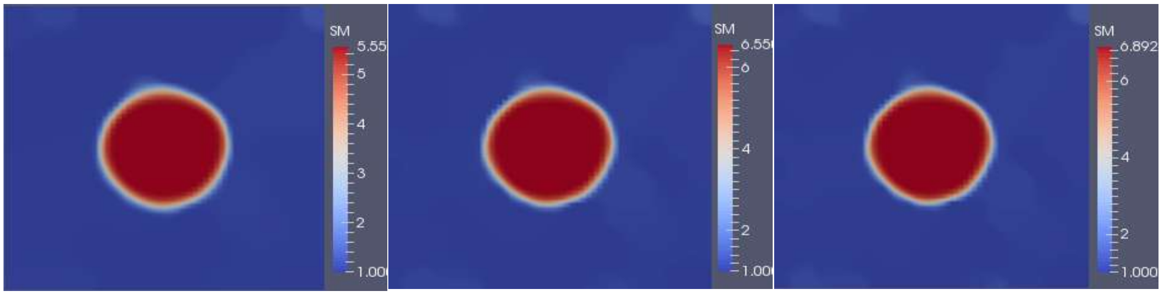

(a) α=1e-9 (b) α=5e-10 (c) α=4e-10

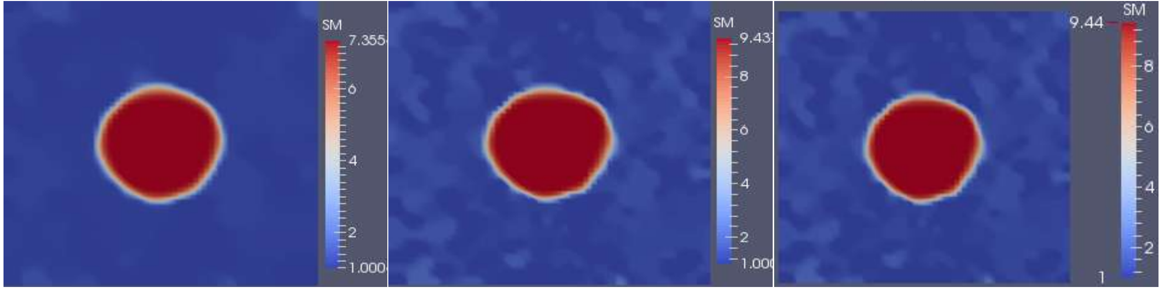

(d) α=3e-10 (e) α=2e-10 (f) α=1e-10

Figure 3.39 Shear modulus reconstruction from element-wise defined material with fine mesh and 3% noise

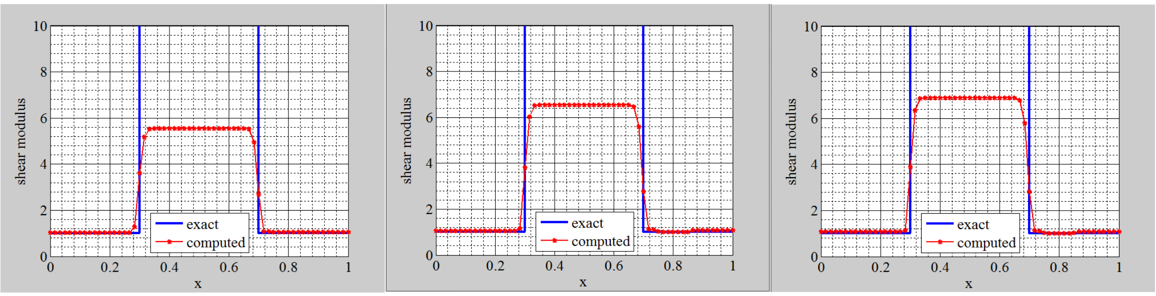

(a) α=1e-10 (b) α=5e-10 (c) α=4e-10

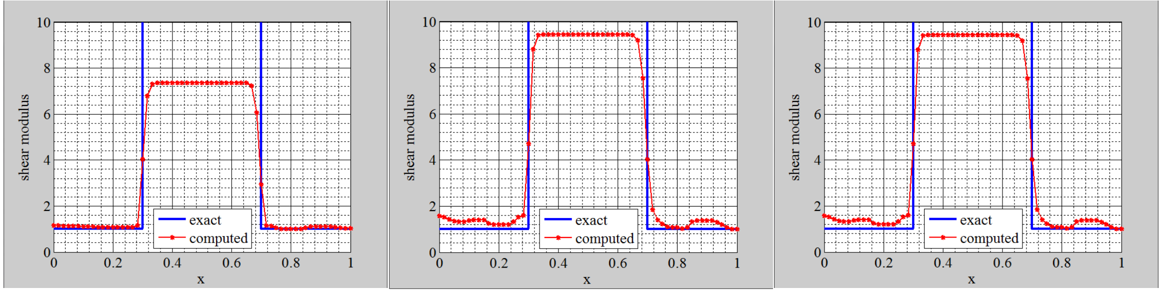

(d) α=3e-10 (e) α=2e-10 (f) α=1e-10

Figure 3.40 Shear modulus reconstruction from element-wise defined material with fine mesh and 3% noise along the horizontal centerline

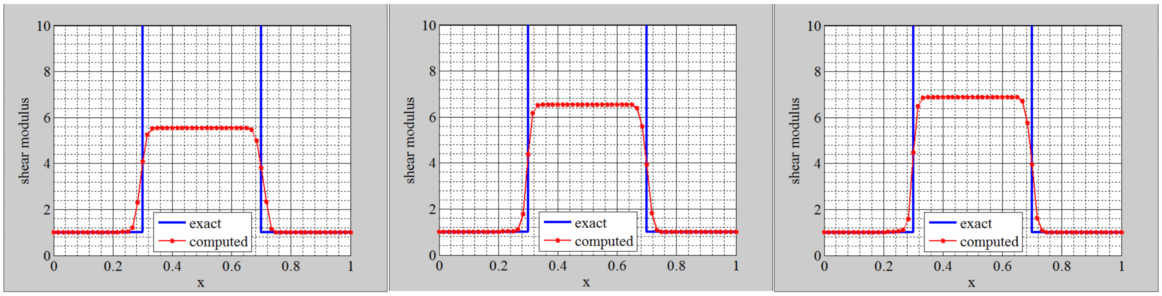

(a) α=1e-10 (b) α=5e-10 (c) α=4e-10

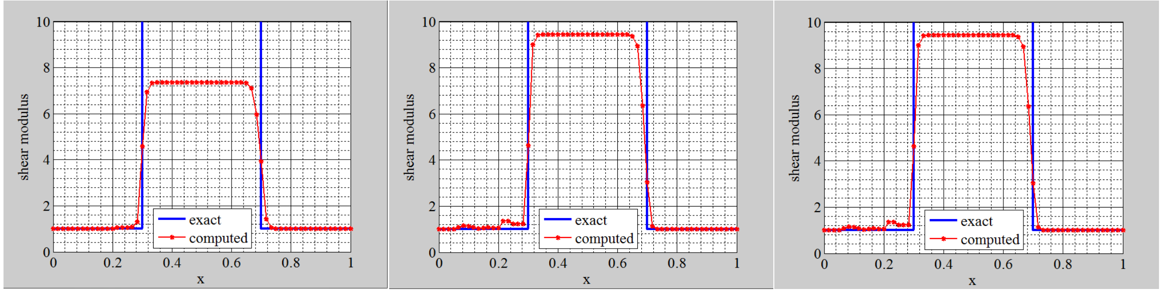

(d) α=3e-10 (e) α=2e-10 (f) α=1e-10

Figure 3.41 Shear modulus reconstruction from element-wise defined material with fine mesh and 3% noise along the vertical centerline

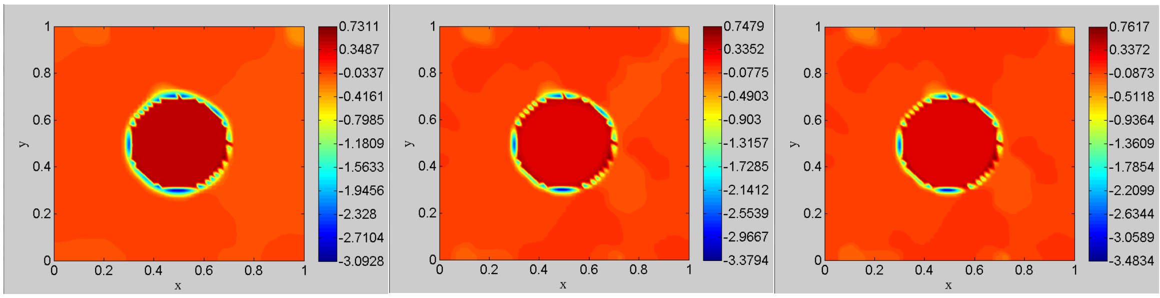

(a) α=1e-10
Relative error = 45.45%

(b) α=5e-10
Relative error = 37.17%

(c) α=4e-10
Relative error = 34.47%

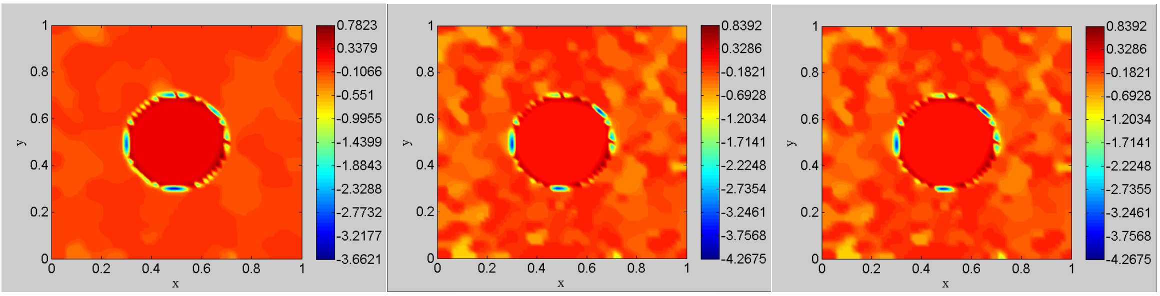

(d) α=3e-10
Relative error = 30.99%

(e) α=2e-10
Relative error = 20.20%

(f) α=1e-10
Relative error = 20.20%

Figure 3.42 Relative spatial error with a fine mesh and 3% noise in the displacement field

3.2.1.4 Continuously Defined Material with Noised Data

In this section, the shear modulus will be reconstructed for the displacement data obtained by solving the forward problem with the continuously defined shear modulus distribution. Furthermore, 1% and 3% noise are added to the displacement field. The displacement field with 1% noise is utilized to reconstruct the shear modulus distribution given in Figure 3.43 for various regularization factors. The regularization parameter $\alpha = 1e-10$ is chosen, resulting in a smooth shear modulus reconstruction. It can be observed that the reconstructions are in good agreement with the exact distributions. In order to better visualize the shear modulus transition between inclusion and background, the shear modulus values are plotted along the horizontal and vertical line passing through the center of the inclusion (see Figures 3.44 and 3.45, respectively). The relative error is plotted in Figure 3.46. It can be observed that the maximum relative error occurs at the border of the inclusion and the background.

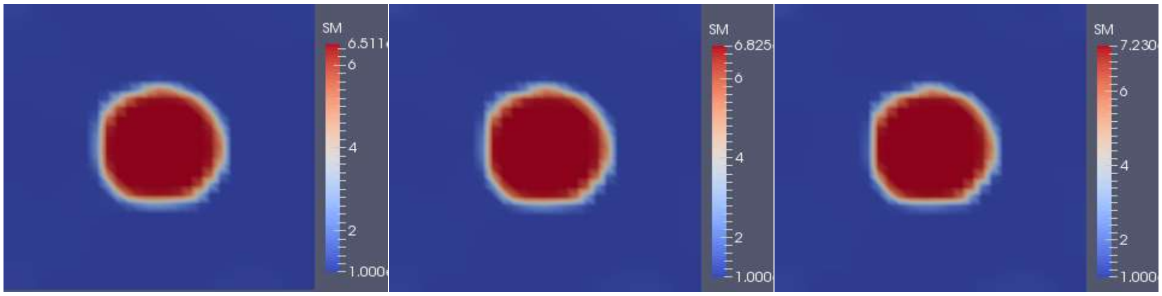

(a) α=5e-10 (b) α=4e-10 (c) α=3e-11

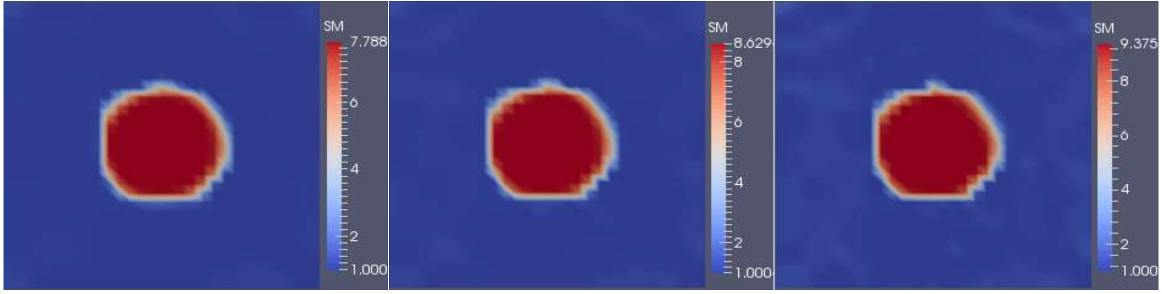

(d) α=2e-10 (e) α=1e-10 (f) α=5e-11

Figure 3.43 Shear modulus reconstruction from continuously defined material with coarse mesh and 1% noise

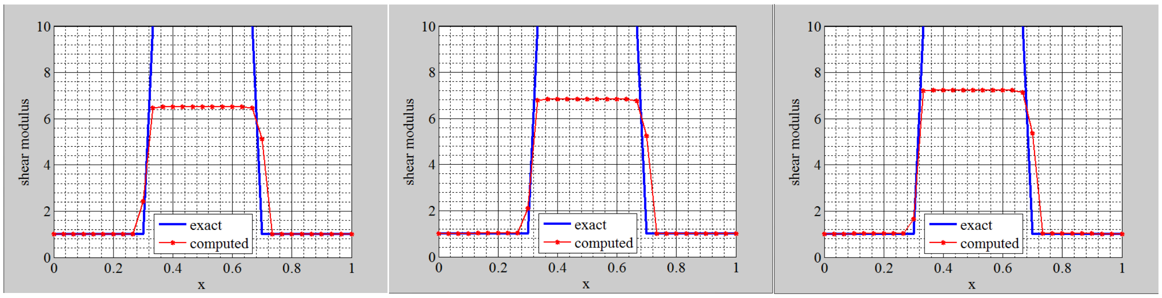

(a) α=5e-10 (b) α=4e-10 (c) α=3e-11

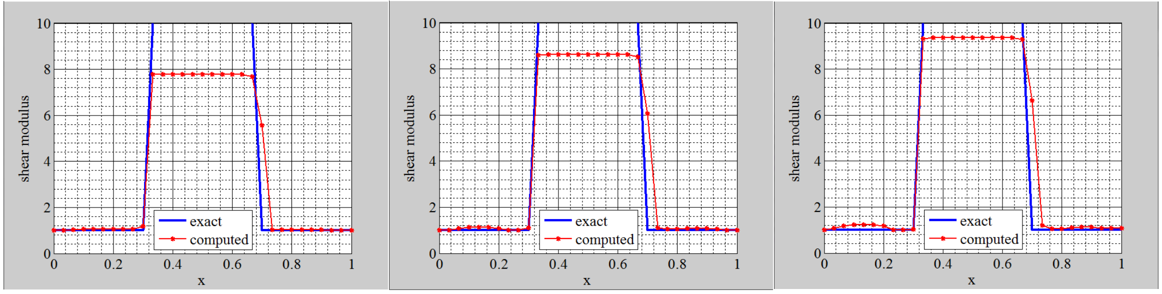

(d) α=2e-10 (e) α=1e-10 (f) α=5e-11

Figure 3.44 Shear modulus reconstruction from continuously defined material with coarse mesh and 1% noise along the horizontal centerline

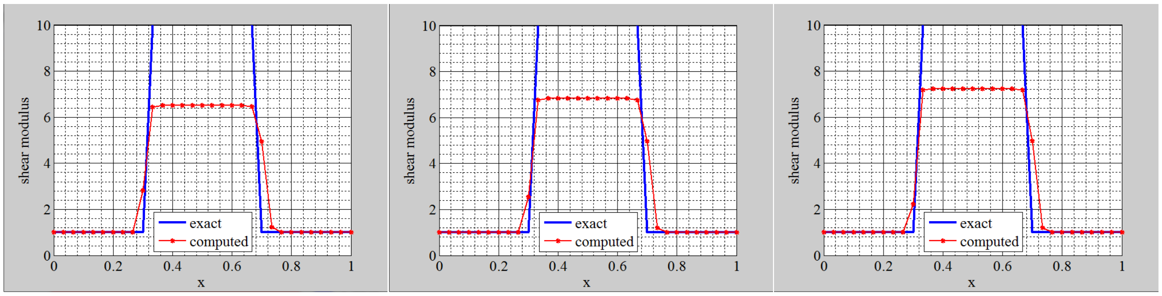

(a) α=5e-10 (b) α=4e-10 (c) α=3e-11

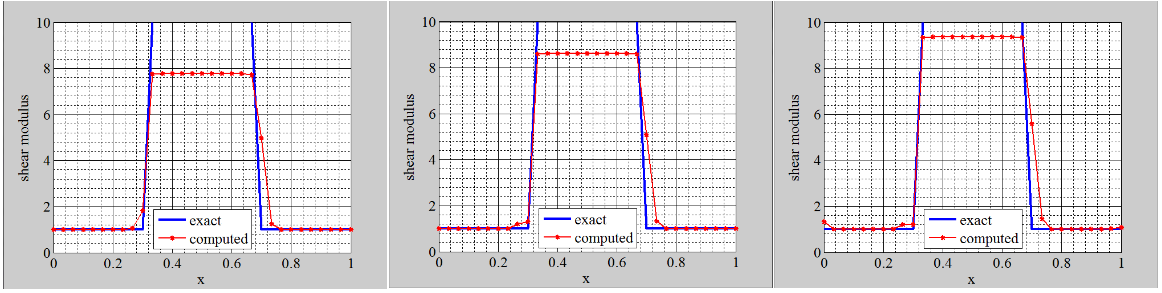

(d) α=2e-10 (e) α=1e-10 (f) α=5e-11

Figure 3.45 Shear modulus reconstruction from continuously defined material with coarse mesh and 1% noise along the vertical centerline

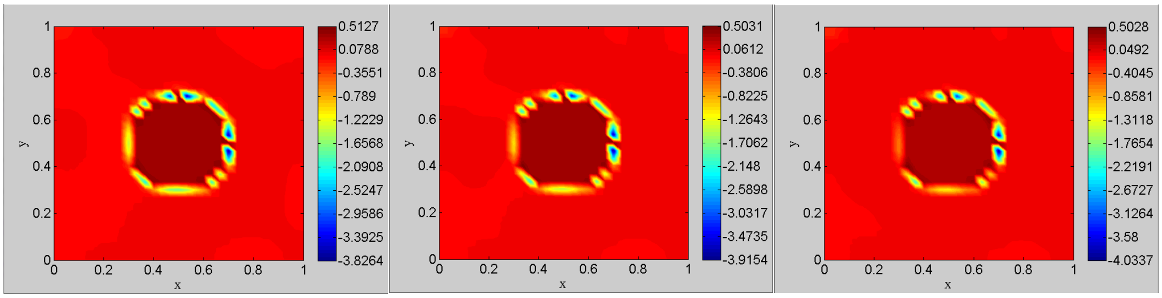

(a) α=5e-10
Relative error = 36.82%

(b) α=4e-10
Relative error = 34.02%

(c) α=3e-11
Relative error = 30.46%

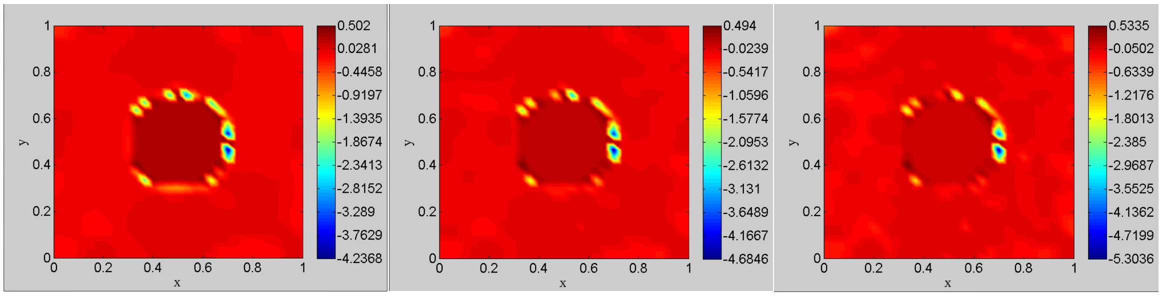

(d) α=2e-10
Relative error = 25.73%

(e) α=1e-10
Relative error = 19.51%

(f) α=5e-11
Relative error = 15.76%

Figure 3.46 Relative spatial error with a coarse mesh and 1% noise in the displacement field

The displacement field with 3% noise is utilized to reconstruct the shear modulus distribution. Figure 3.47 represents the shear modulus reconstructions for various regularization factors. The regularization parameter α=3.4e-10 appears to yield the best recovered shear modulus. It can be observed that the inclusion is visible, but due to the high noise level in the displacement field, the shear modulus value loses significantly on contrast. The shear modulus values along the horizontal and vertical line through the center of the inclusion are given in Figures 3.48 and 3.49 to visualize the transition at the interface of inclusion and background. Further, relative spatial error in the shear modulus is plotted in Figure 3.50.

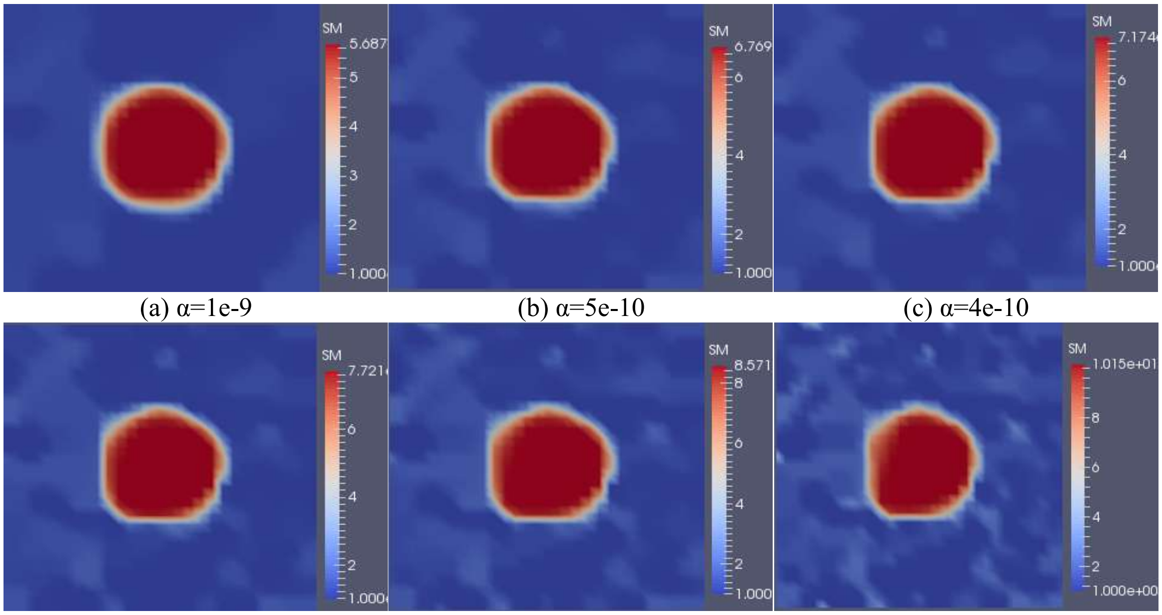

(a) α=1e-9 (b) α=5e-10 (c) α=4e-10

(d) α=3e-10 (e) α=2e-10 (f) α=1e-10

Figure 3.47 Shear modulus reconstruction from continuously defined material with coarse mesh and 3% noise

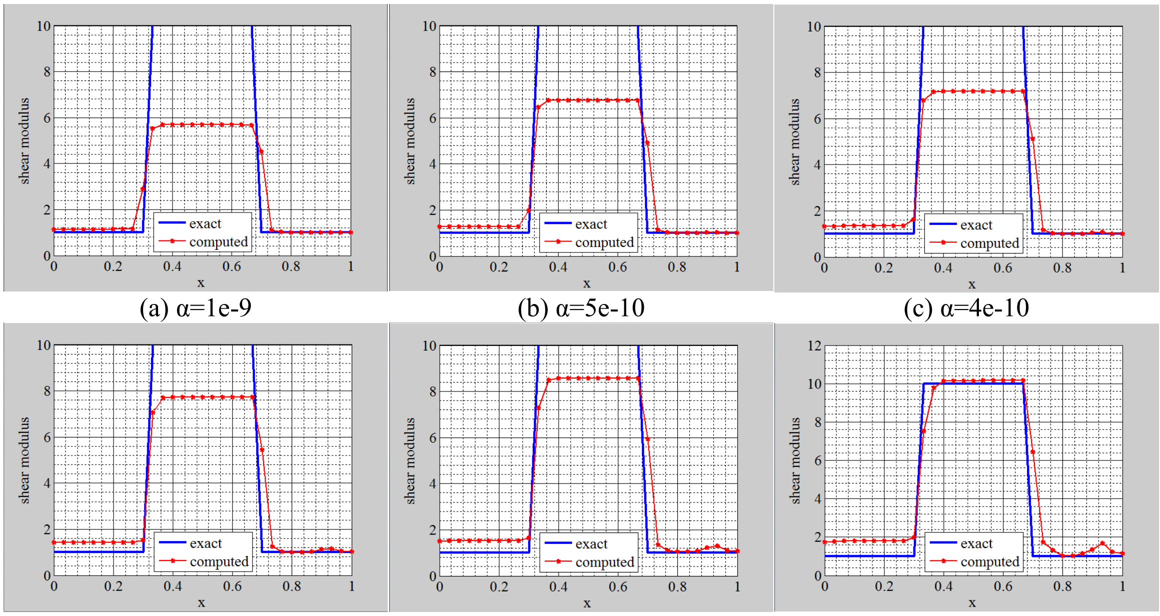

(a) α=1e-9 (b) α=5e-10 (c) α=4e-10

(d) α=3e-10 (e) α=2e-10 (f) α=1e-10

Figure 3.48 Shear modulus reconstruction from continuously defined material with coarse mesh and 3% noise along the horizontal centerline

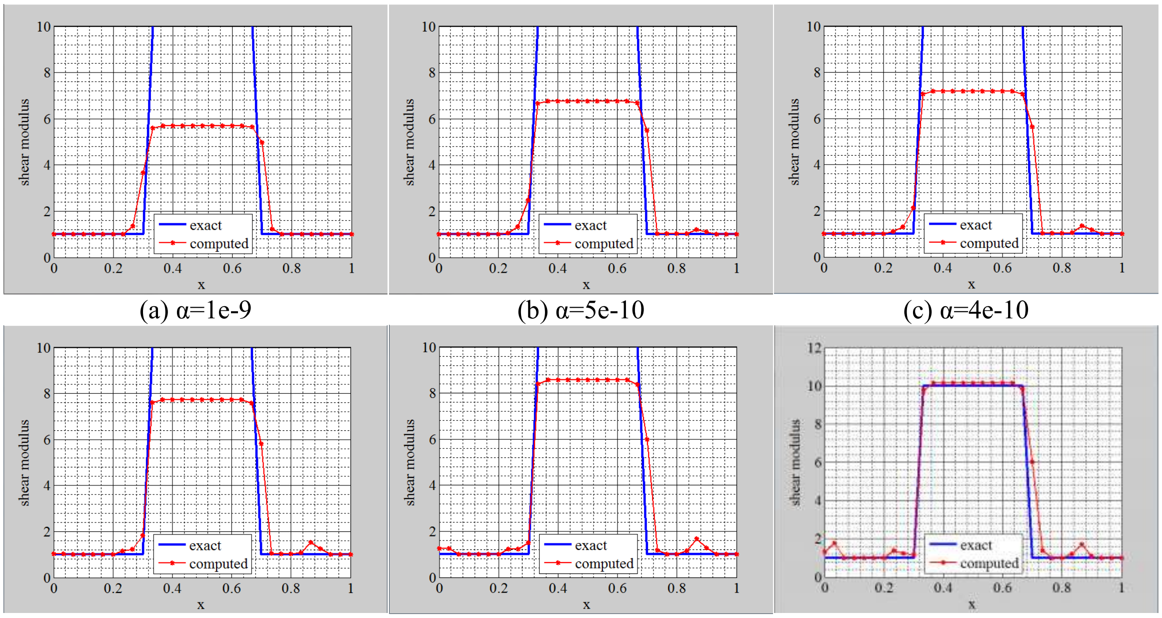

(a) α=1e-9 (b) α=5e-10 (c) α=4e-10

(d) α=3e-10 (e) α=2e-10 (f) α=1e-10

Figure 3.49 Shear modulus reconstruction from continuously defined material with coarse mesh and 3% noise along the vertical centerline

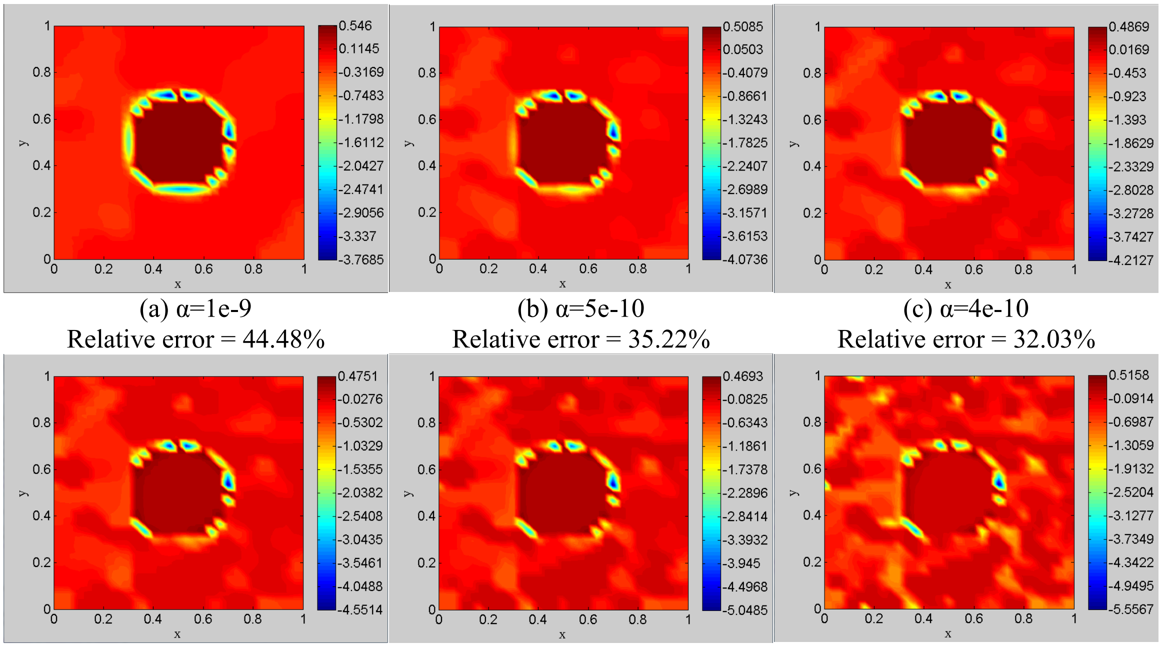

(a) α=1e-9 (b) α=5e-10 (c) α=4e-10

Relative error = 44.48% Relative error = 35.22% Relative error = 32.03%

(d) α=3e-10 (e) α=2e-10 (f) α=1e-10

Relative error = 28.20% Relative error = 23.53% Relative error = 22.00%

Figure 3.50 Relative spatial error in the shear modulus with a coarse mesh and 3% noise in the displacement field

In Figure 3.51 the reconstruction of the shear modulus is shown using a fine mesh. One can observe that the shear modulus reconstruction is much better than the reconstruction with the coarse mesh. Figure 3.52 and 3.53 show the shear modulus value plotted along the horizontal and vertical centerlines. In Figure 3.54 the relative error in the shear modulus is visualized spatially. Here, the relative spatial error in the shear modulus does not change much as the mesh is refined. One can observe that the shear modulus is very well reproduced with clear inclusion boundaries, even though its boundaries are very close to the domain boundaries. Again, the maximum error occurs at the border of the inclusion and the background (see Figure 3.54).

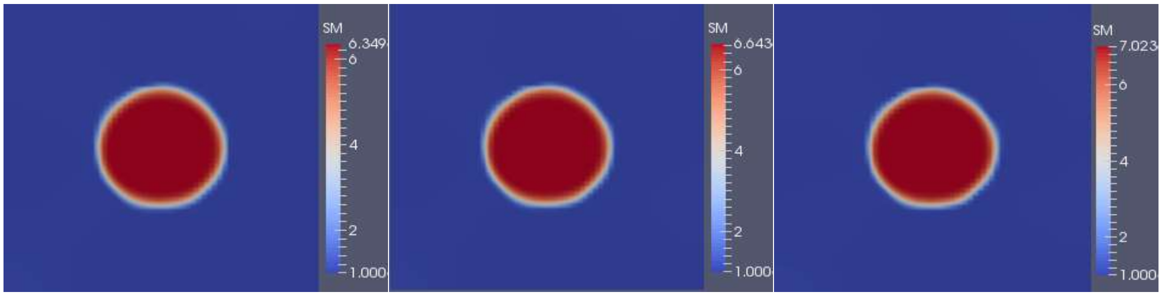

(a) α=5e-10 (b) α=4e-10 (c) α=3e-10

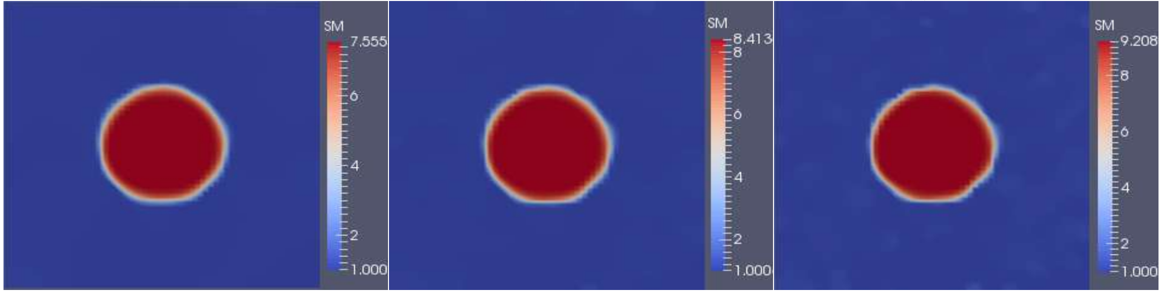

(d) α=2e-10 (e) α=1e-10 (f) α=5e-11

Figure 3.51 Shear modulus reconstruction from continuously defined material with fine mesh and 1% noise

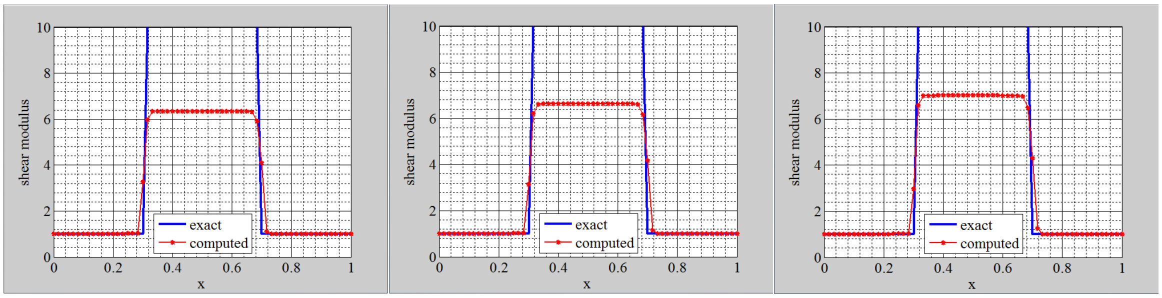

(a) α=5e-10 (b) α=4e-10 (c) α=3e-10

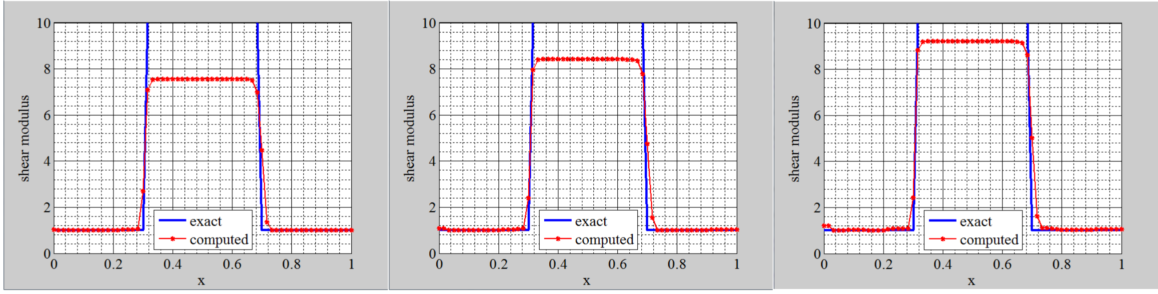

(d) α=2e-10 (e) α=1e-10 (f) α=5e-11

Figure 3.52 Shear modulus reconstruction from continuously defined material with fine mesh and 1% noise along the horizontal centerline

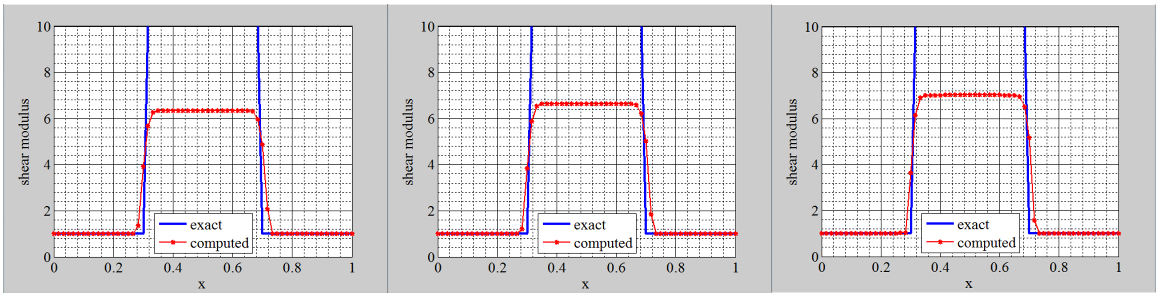

(a) α=5e-10 (b) α=4e-10 (c) α=3e-10

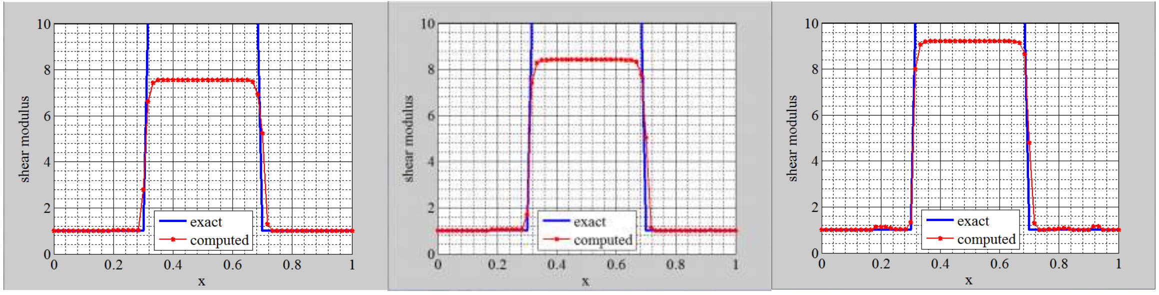

(d) α=2e-10 (e) α=1e-10 (f) α=5e-11

Figure 3.53 Shear modulus reconstruction from continuously defined material with fine mesh and 1% noise along the vertical centerline

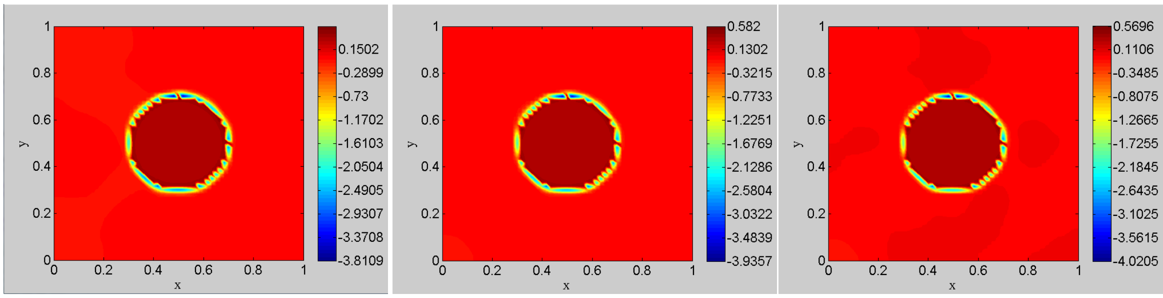

(a) α=5e-10
Relative error = 38.18%

(b) α=4e-10
Relative error = 35.66%

(c) α=3e-10
Relative error = 32.42%

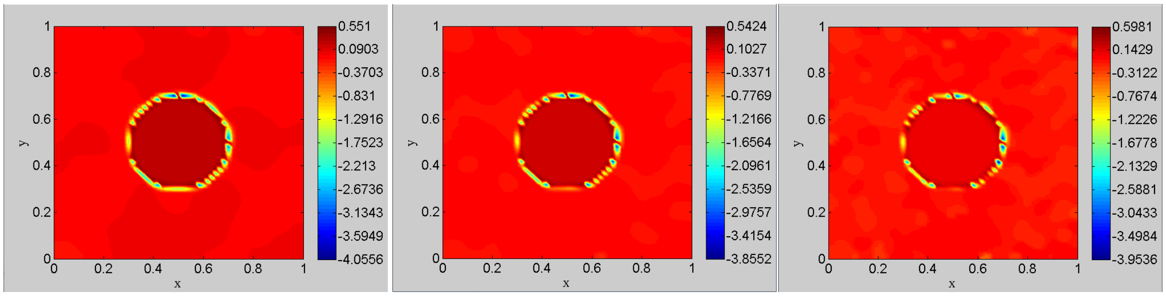

(d) α=2e-10
Relative error = 27.92%

(e) α=1e-10
Relative error = 21.05%

(f) α=5e-11
Relative error = 15.72%

Figure 3.54 Relative spatial error in the shear modulus with a fine mesh and 1% noise in the displacement field

For the displacement field with 3% noise the shear modulus reconstruction is given in Figure 3.55 for different values of the regularization factor. The regularization parameter α=3e-10 appears to yield the best shear modulus reconstruction. It can be observed that the shear modulus reconstruction improves as compared to the reconstruction utilizing the coarse mesh. This is partially due to the fact that the inclusion can be better resolved with a finer mesh. However, it also appears that the background is much smoother and "more homogeneous". In order to visualize the change of the shear modulus at the border of inclusion and background, Figure 3.56 and 3.57 are provided for both, the horizontal and vertical centerline. The relative spatial error in the shear modulus is plotted in Figure 3.58.

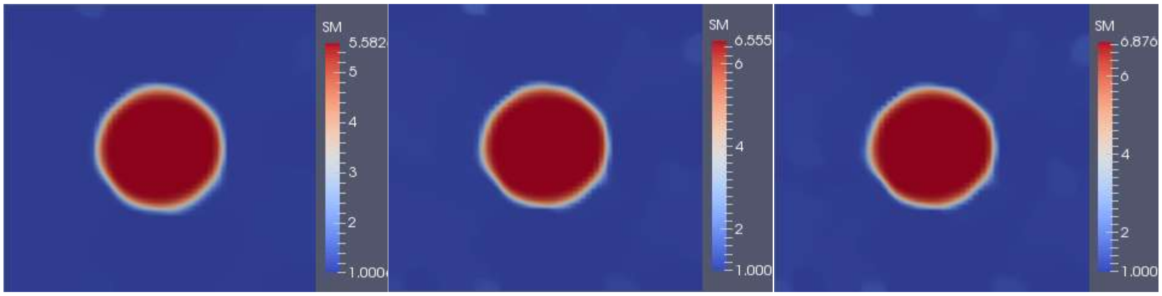

(a) α=1e-9 (b) α=5e-10 (c) α=4e-10

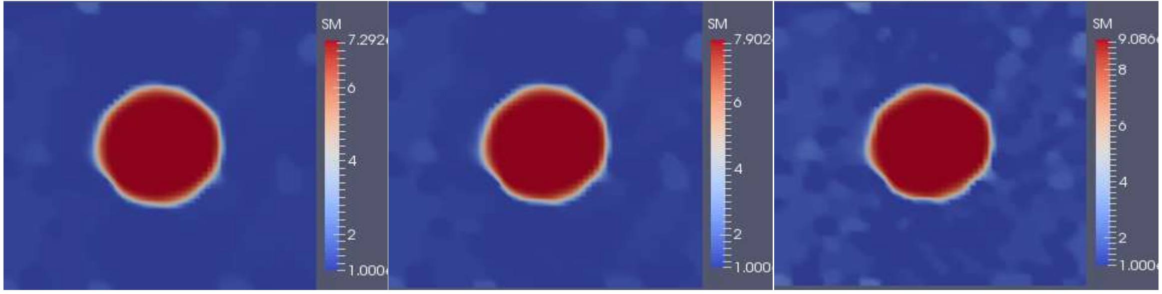

(d) α=3e-10 (e) α=2e-10 (f) α=1e-10

Figure 3.55 Shear modulus reconstruction from continuously defined material with fine mesh and 3% noise

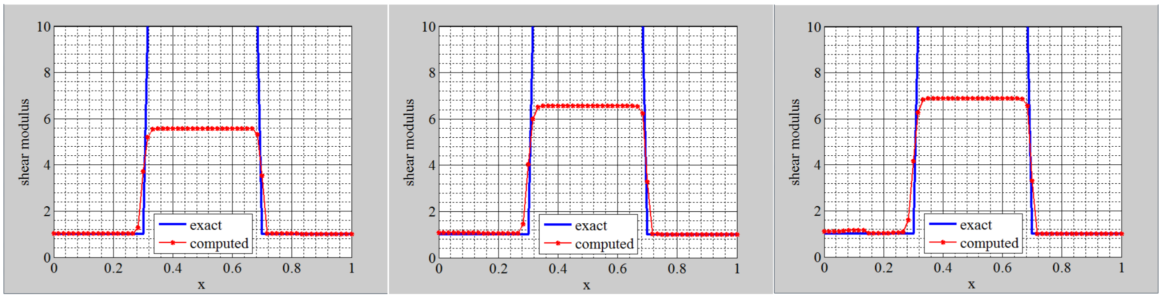

(a) α=1e-9 (b) α=5e-10 (c) α=4e-10

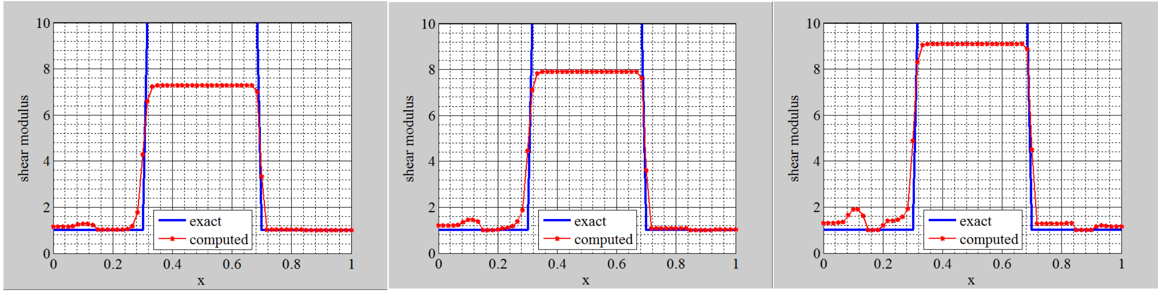

(d) α=3e-10 (e) α=2e-10 (f) α=1e-10

Figure 3.56 Shear modulus reconstruction from continuously defined material with fine mesh and 3% noise along the horizontal centerline

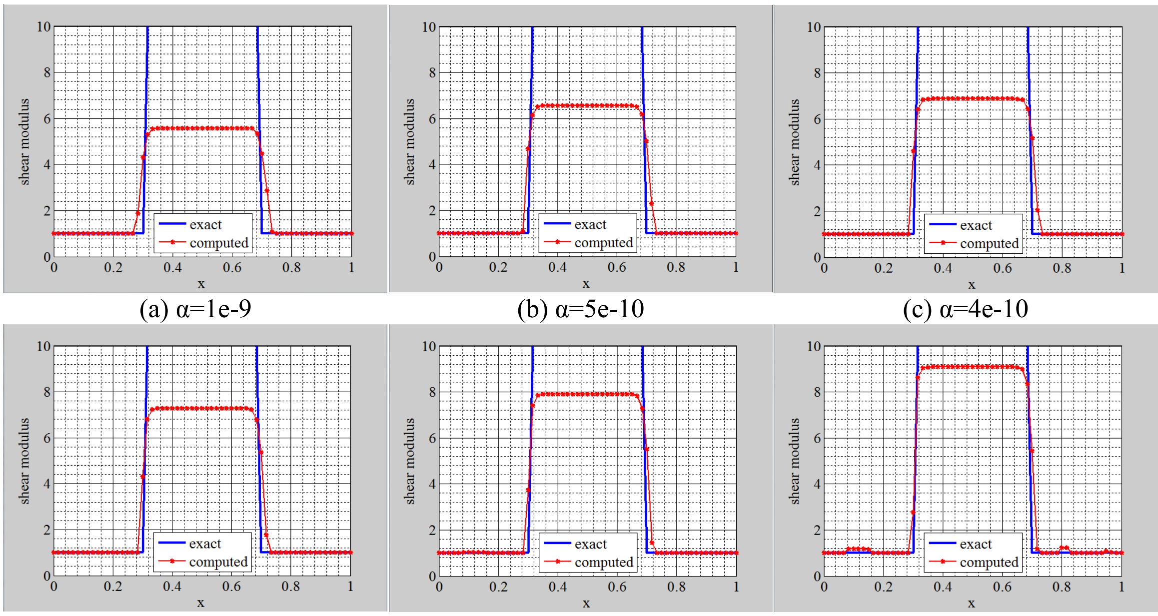

(a) α=1e-9 (b) α=5e-10 (c) α=4e-10

(d) α=3e-10 (e) α=2e-10 (f) α=1e-10

Figure 3.57 Shear modulus reconstruction from continuously defined material with fine mesh and 3% noise along the vertical centerline

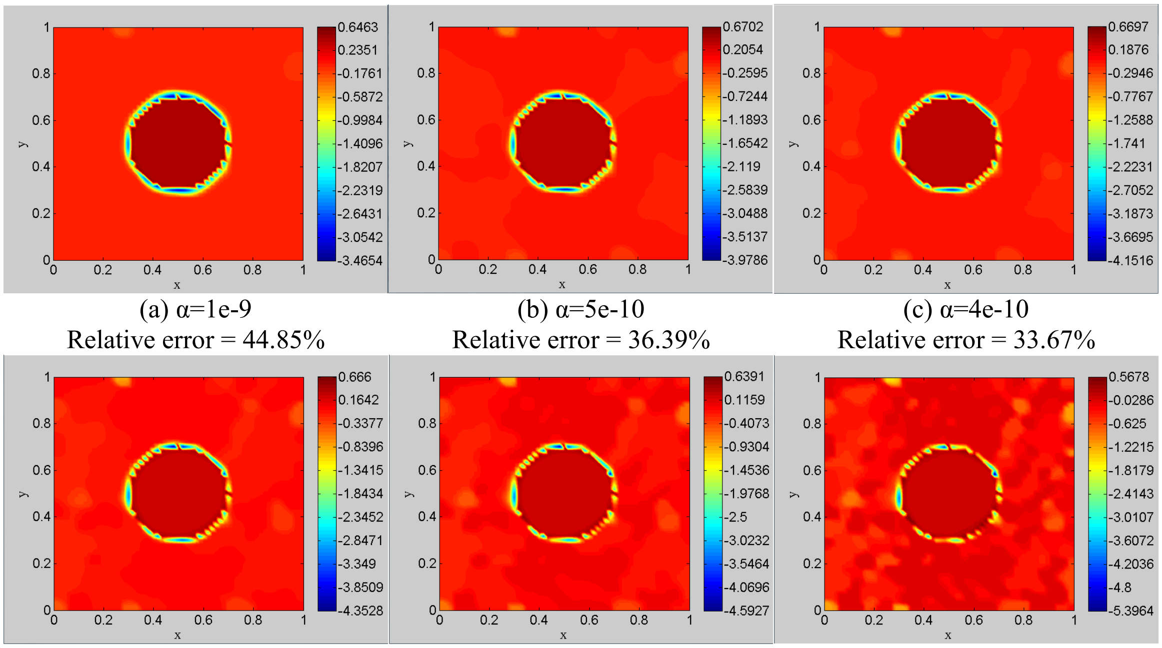

(a) α=1e-9
Relative error = 44.85%

(b) α=5e-10
Relative error = 36.39%

(c) α=4e-10
Relative error = 33.67%

(d) α=3e-10
Relative error = 30.22%

(e) α=2e-10
Relative error = 25.47%

(f) α=1e-10
Relative error = 18.64%

Figure 3.58 Relative spatial error in the shear modulus reconstruction with a fine mesh and 3% noise in the displacement data

3.2.2 Shear Modulus Reconstruction in Model 2

3.2.2.1 Element-wise Defined Material with Noise Free Data

In this section, the layered ring model introduced earlier as Model 2, is analyzed. The three layers have a shear modulus ratio of 1, 5, and 10 from the inner to the outer layer. It is noted that while a layered ring model could represent an artery's layers (e.g. adventitia, media, and intima), the shear modulus values selected herein do not represent any of those actual values present in arteries. However, this study reveals that it is possible to determine the elastic properties knowing the displacement field. The measured field is created by solving the forward problem (see section 3.1). Quadrilateral elements are used to solve the forward problem. The loading scenario is considered as follows: the ring specimen is expanded by prescribing a uniform displacement in radial direction while keeping the outer surface traction free. In Figure 3.59, the reconstructed shear modulus is plotted for different choices of the regularization parameter, α. The shear modulus ratio of the outer layer to the inner layer and the shear modulus ratio of the middle layer to the inner layer are very close to the exact value of 10 and 5, respectively. Figure 3.60 shows the shear modulus value plotted along the radial direction. This can be done because the ring model is axisymmetric, so all the elastic parameters should be the same in the radial direction no matter what direction is chosen. In Figure 3.61, the relative spatial error in the shear modulus between the recovered value and the exact value is visualized spatially with different regularization parameters. One can observe that the shear modulus is well recovered. The comparison between the exact and reconstructed value of the shear modulus along the radial direction in Figure 3.61 shows that the reconstructed shear modulus value is of good quality except at the borders of the layers.

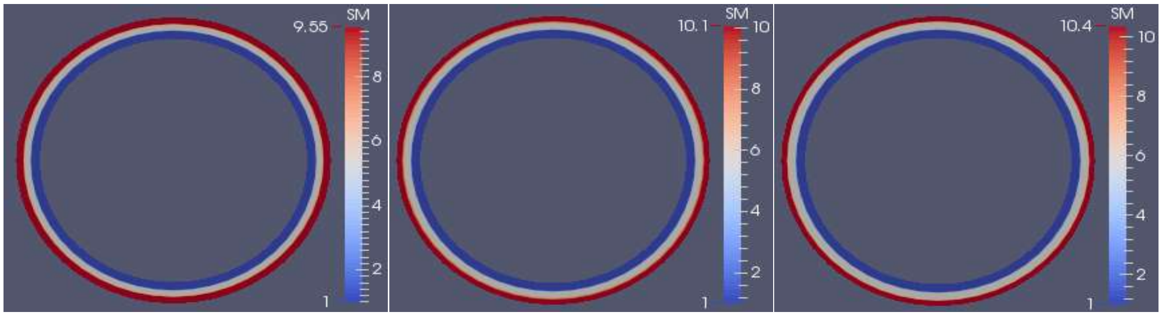

(a) α=3e-15 (b) α=2.5e-15 (c) α=2e-15

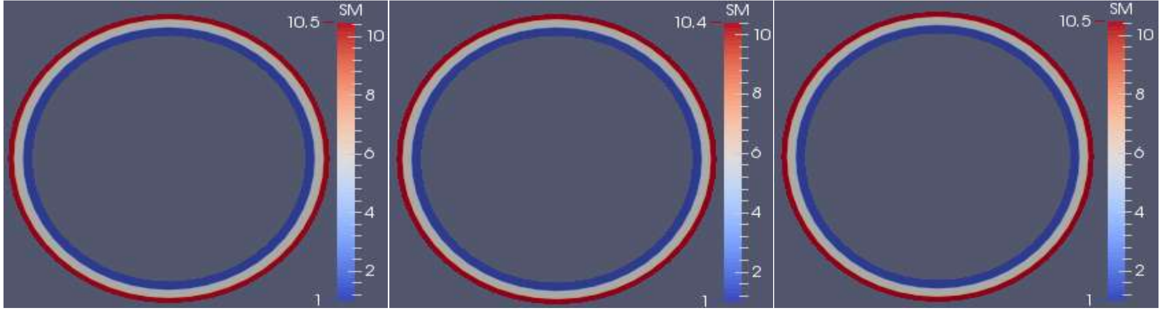

(d) α=1.75e-15 (e) α=1.5e-15 (f) α=1e-15

Figure 3.59 Shear modulus reconstruction from element-wise defined material with coarse mesh and noise free data

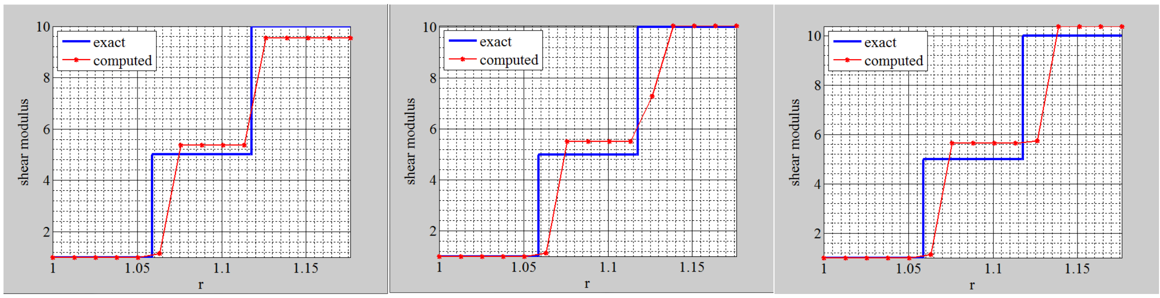

(a) α=3e-15

(b) α=2.5e-15

(c) α=2e-15

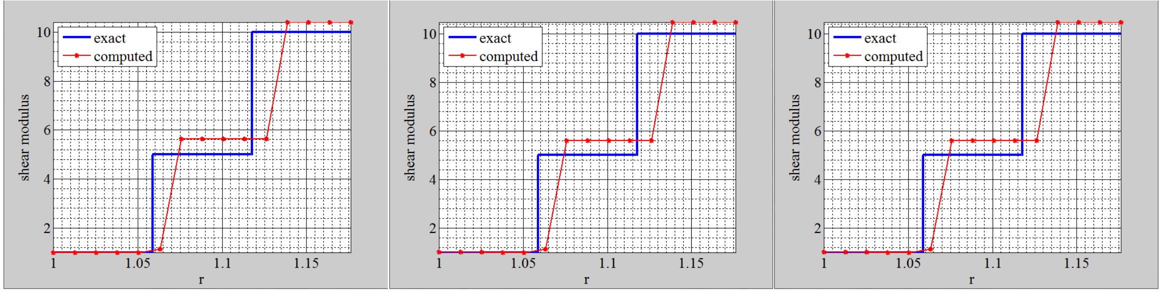

(d) α=1.75e-15

(e) α=1.5e-15

(f) α=1e-15

Figure 3.60 Shear modulus reconstruction from element-wise defined material with coarse mesh and noise free data along the radial direction

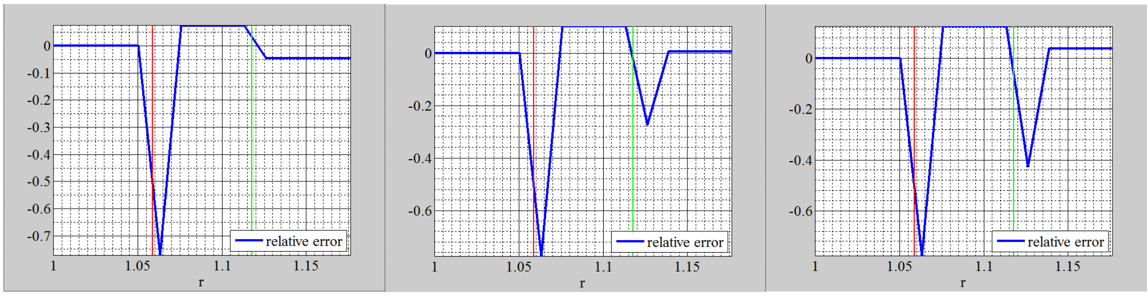

(a) α=3e-15
Relative error = 16.87%

(b) α=2.5e-15
Relative error = 20.00%

(c) α=2e-15
Relative error = 24.35%

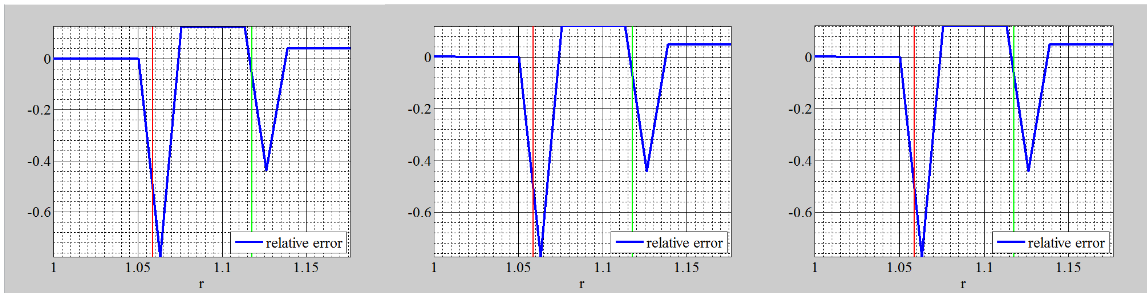

(d) α=1.75e-15
Relative error = 24.66%

(e) α=1.5e-15
Relative error = 24.65%

(f) α=1e-15
Relative error = 24.65%

Figure 3.61 Relative spatial error in the shear modulus plotted in radial direction

For the fine mesh, Figure 3.62 represents the reconstruction of the shear modulus for different regularization factors and noise free displacement data. In Figure 3.62 (b), the reconstructed shear modulus ratio of outer layer to inner layer approaches the exact value, 10, when the regularization parameter, α=2.5e-15 is chosen. Figure 3.63 shows the shear modulus value plotted along the radial direction. In Figure 3.64, the relative error in the shear modulus is visualized spatially. One can observe that the shear modulus is well recovered, in other words the target shear modulus distribution is reproduced very well with clear boundary layers.

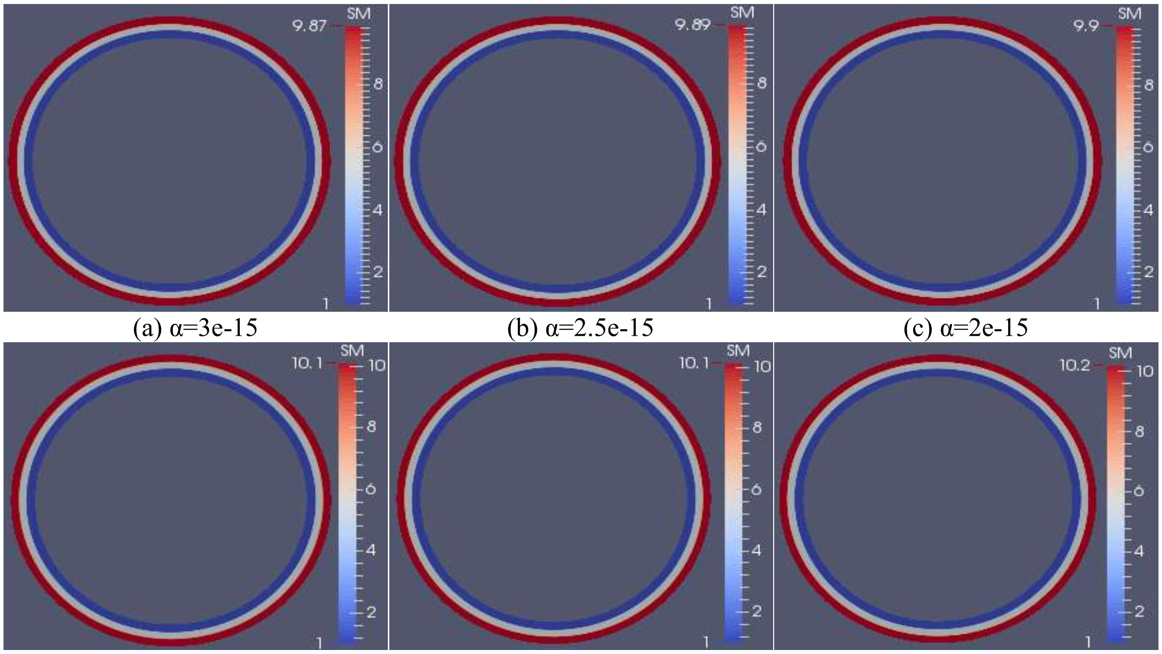

(a) α=3e-15 (b) α=2.5e-15 (c) α=2e-15

(d) α=1.75e-15 (e) α=1.5e-15 (f) α=1e-15

Figure 3.62 Shear modulus reconstruction from element-wise defined material with fine mesh and noise free data

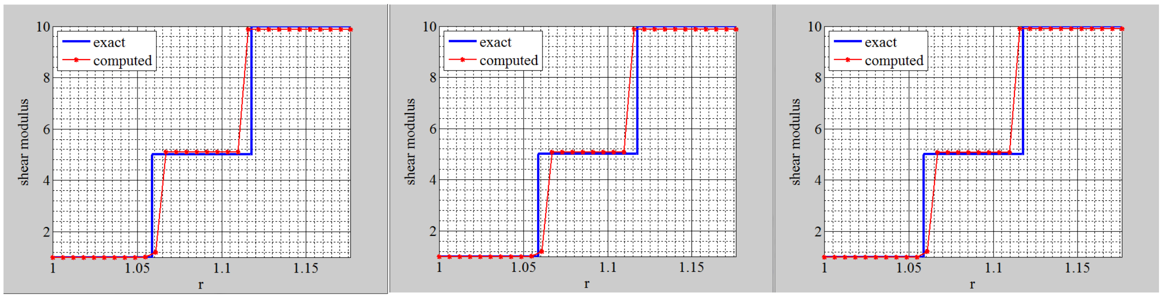

(a) α=3e-15 (b) α=2.5e-15 (c) α=2e-15

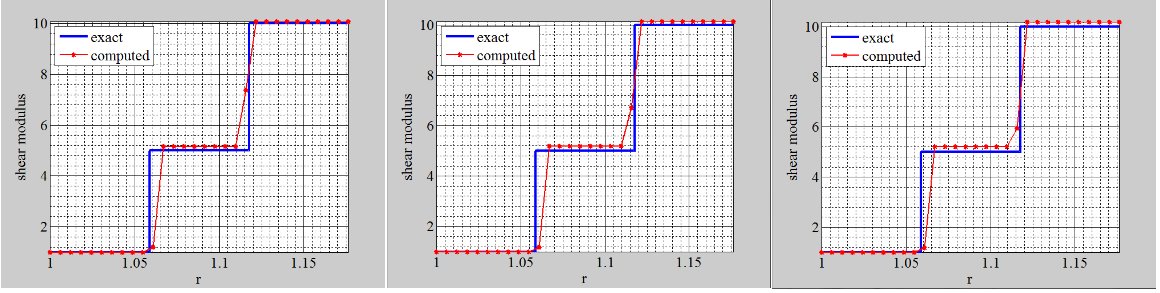

(d) α=1.75e-15 (e) α=1.5e-15 (f) α=1e-15

Figure 3.63 Shear modulus reconstruction from element-wise defined material with fine mesh and noise free data along the radial direction

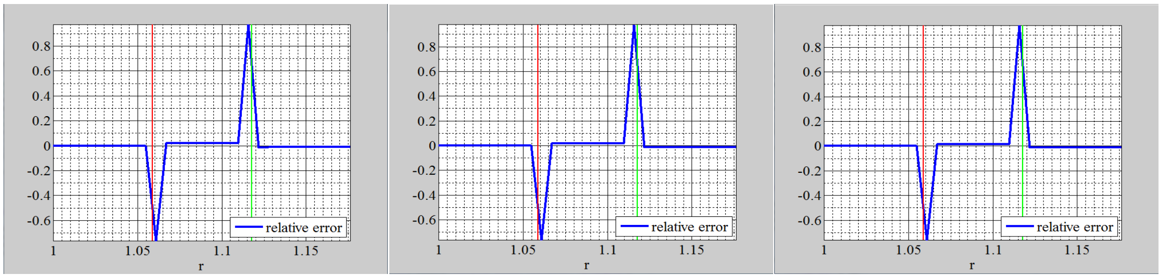

(a) α=3e-15
Relative error = 17.27%

(b) α=2.5e-15
Relative error = 17.26%

(c) α=2e-15
Relative error = 17.23%

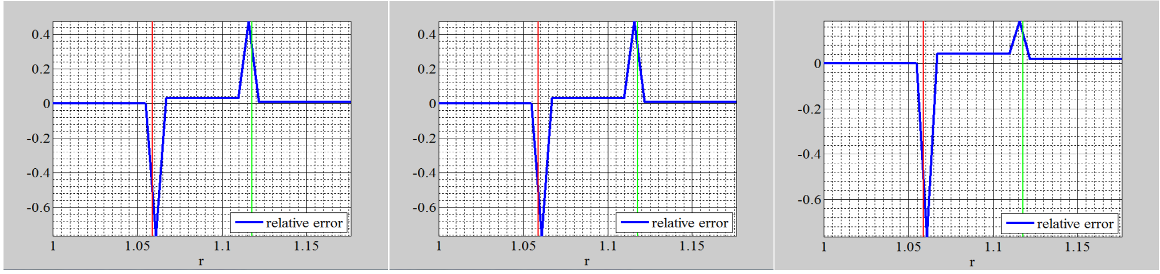

(d) α=1.75e-15
Relative error = 12.57%

(e) α=1.5e-15
Relative error = 11.75%

(f) α=1e-15
Relative error = 11.16%

Figure 3.64 Relative spatial error in the shear modulus plotted in radial direction

3.2.2.2 Continuously Defined Material with Noise Free Data

The shear modulus reconstruction is now assessed utilizing the displacement data, obtained from the continuously defined shear modulus distribution. In Figure 3.65 (e) the reconstructed shear modulus ratio of outer layer to inner layer approaches the exact value, 10, when the regularization parameter, α=1e-16 is chosen. One can observe that the value of the shear modulus will stop increasing when the value approaches the exact value, 10. This is one difference from the reconstruction using the element-wise defined material in the previous section. Figure 3.66 shows the shear modulus value plotted along the radial direction. In Figure 3.67, the relative error in the shear modulus is visualized spatially. One can observe that the shear modulus is well recovered. The comparison between the exact and reconstructed value of the shear modulus along radial direction in Figure 3.66 shows that the shear modulus is also well recovered at the borders of the layers.

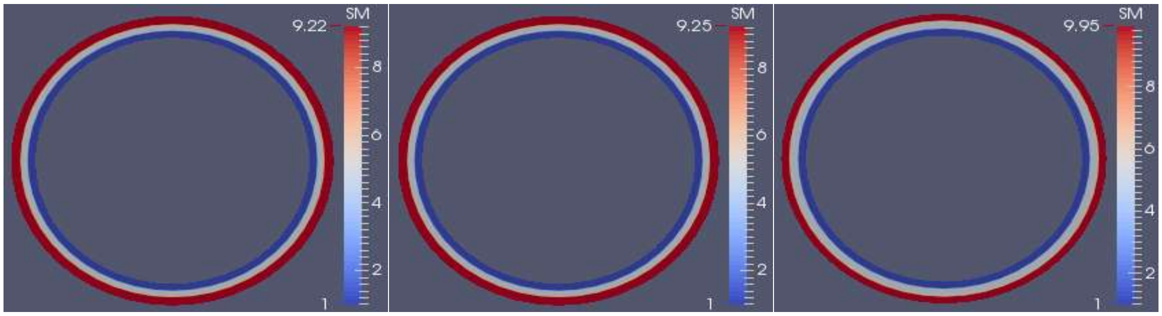

(a) α=1e-13 (b) α=5e-15 (c) α=2.5e-15

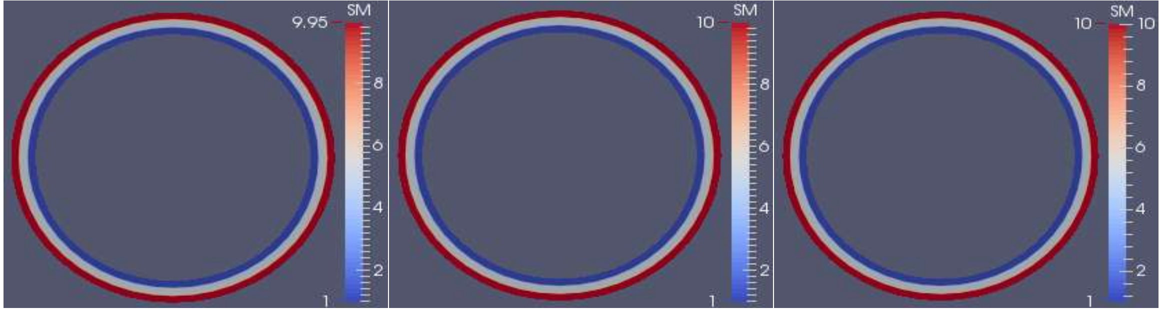

(d) α=1e-15 (e) α=1e-16 (f) α=1e-17

Figure 3.65 Shear modulus reconstruction from continuously defined material with coarse mesh and noise free data

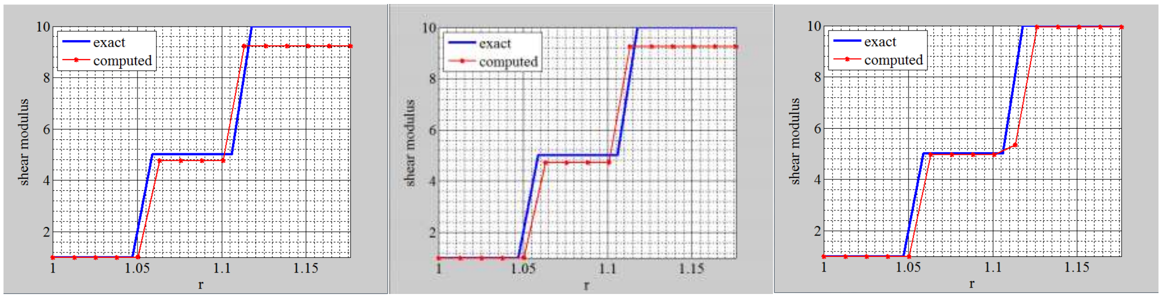

(a) α=1e-13 (b) α=5e-15 (c) α=2.5e-15

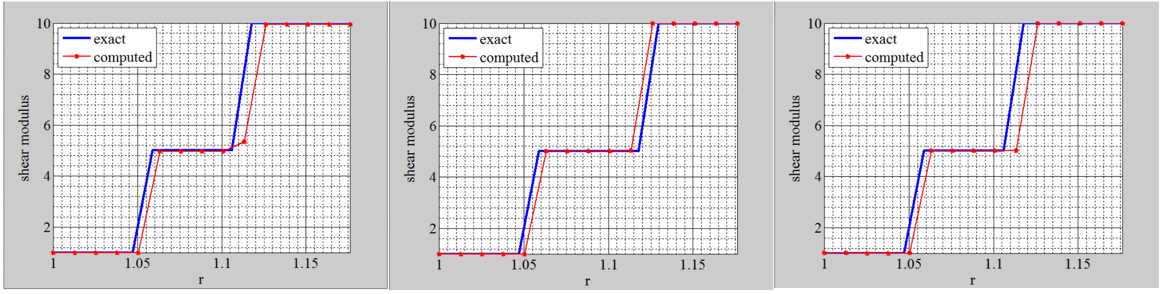

(d) α=1e-15 (e) α=1e-16 (f) α=1e-17

Figure 3.66 Shear modulus reconstruction from continuously defined material with coarse mesh and noise free data along the radial direction

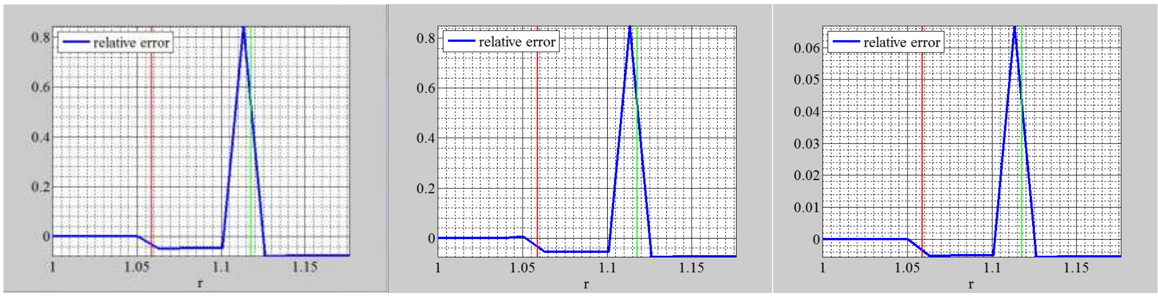

(a) α=1e-13
Relative error = 18.65%

(b) α=5e-15
Relative error = 18.67%

(c) α=2.5e-15
Relative error = 1.44%

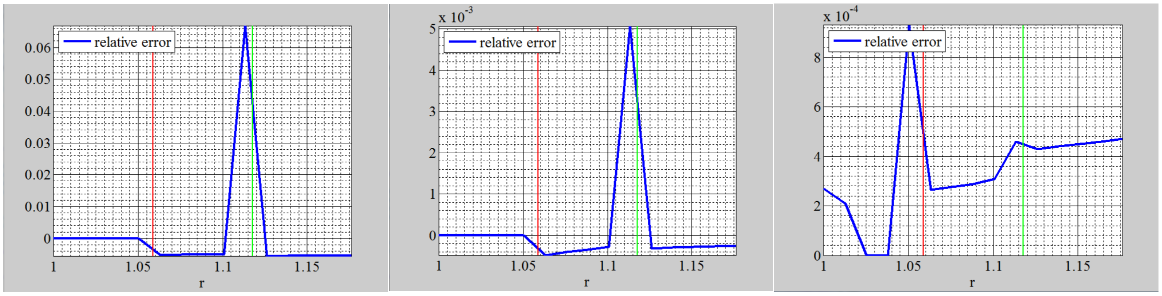

(d) α=1e-15
Relative error = 1.44%

(e) α=1e-16
Relative error = 0.11%

(f) α=1e-17
Relative error = 0.04%

Figure 3.67 Relative spatial error in the shear modulus plotted in radial direction

Figure 3.68 shows the reconstruction of the shear modulus using the fine mesh for different regularization factors. In Figure 3.68 (c) the reconstructed shear modulus ratio of outer layer to inner layer approaches the exact value, 10, when the regularization parameter, α=2e-15 is chosen. Figure 3.69 shows the shear modulus value plotted along the horizontal and vertical lines through the center of the inclusions. In Figure 3.70 the relative error in the shear modulus is visualized spatially. One can observe that the shear modulus is well recovered. In particular, one can also observe that the shear modulus is reproduced very well with clear layer boundaries.

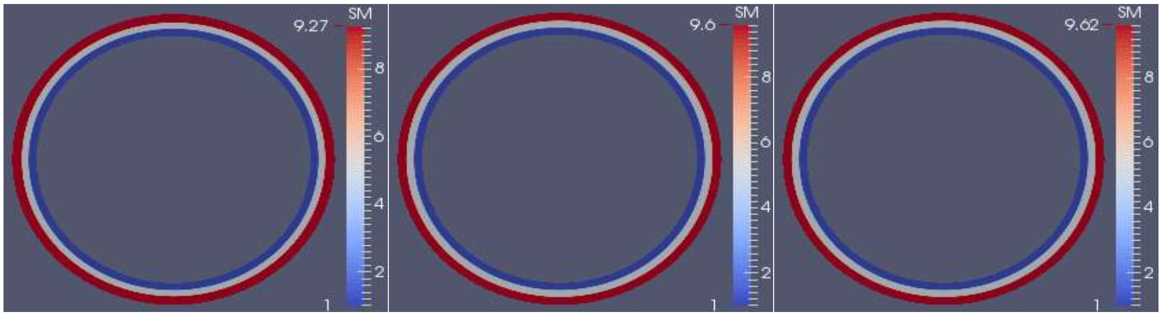

(a) α=1e-14 (b) α=5e-15 (c) α=2.5e-15

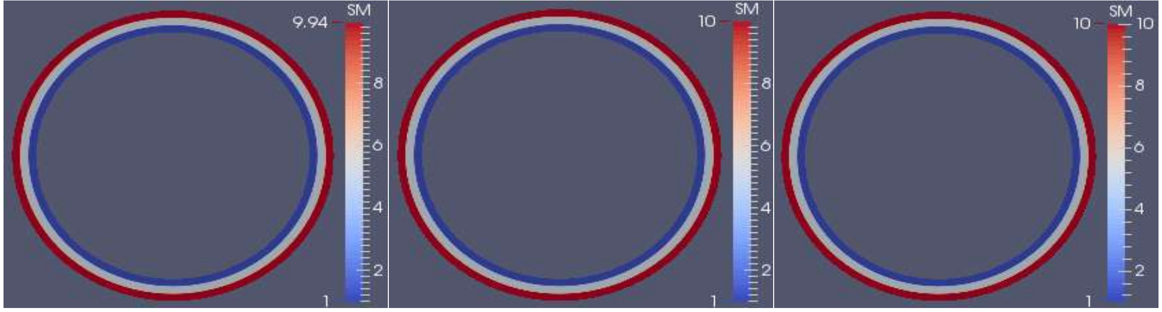

(d) α=1e-15 (e) α=1e-16 (f) α=1e-17

Figure 3.68 Shear modulus reconstruction from continuously defined material with a fine mesh and noise free data

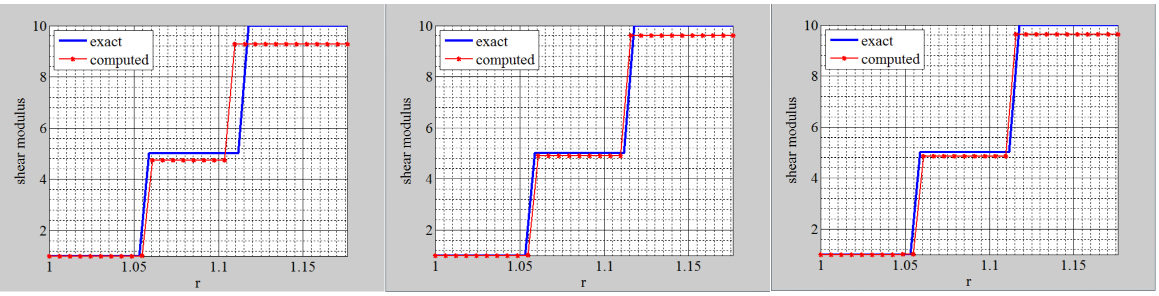

(a) α=1e-14 (b) α=5e-15 (c) α=2.5e-15

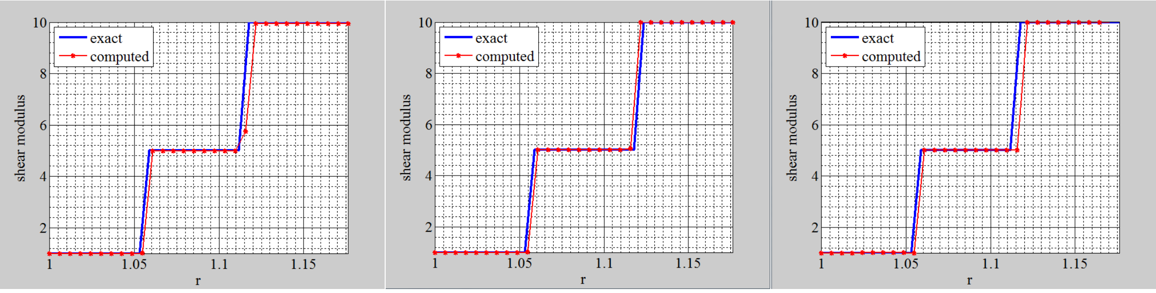

(d) α=1e-15 (e) α=1e-16 (f) α=1e-17

Figure 3.69 Shear modulus reconstruction from continuously defined material with a fine mesh and noise free data along the radial direction

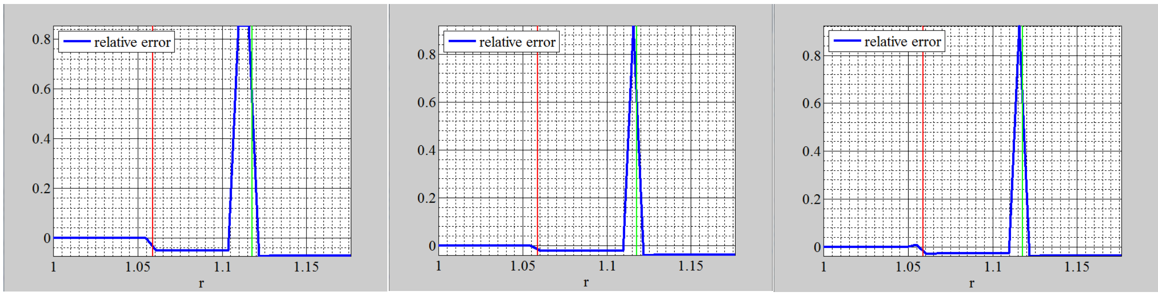

(a) α=1e-14
Relative error = 18.61%

(b) α=5e-15
Relative error = 13.59%

(c) α=2.5e-15
Relative error = 13.60%

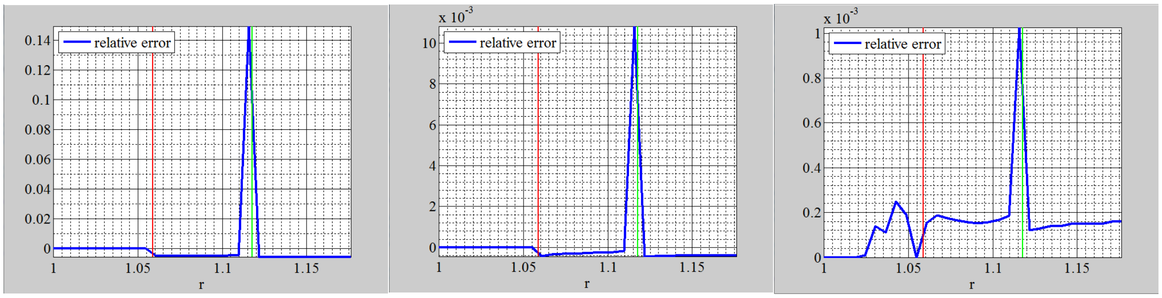

(d) α=1e-15
Relative error = 2.18%

(e) α=1e-16
Relative error = 0.17%

(f) α=1e-17
Relative error = 0.03%

Figure 3.70 Relative spatial error in the shear modulus plotted in radial direction

3.2.2.3 Element-wise Defined Material with Noised Data

For 1% noise the shear modulus is plotted in Figures 3.71. It can be observed that the reconstructions are in good agreement with the exact distributions. To visualize the shear modulus at the interface of the layers, Figure 3.72 and 3.73 are provided. Therein, the shear modulus values are plotted for both, the horizontal and vertical centerlines. The relative spatial error in the shear modulus is plotted in Figure 3.74. One can observe that the maximum relative error occurs at the border of the layers.

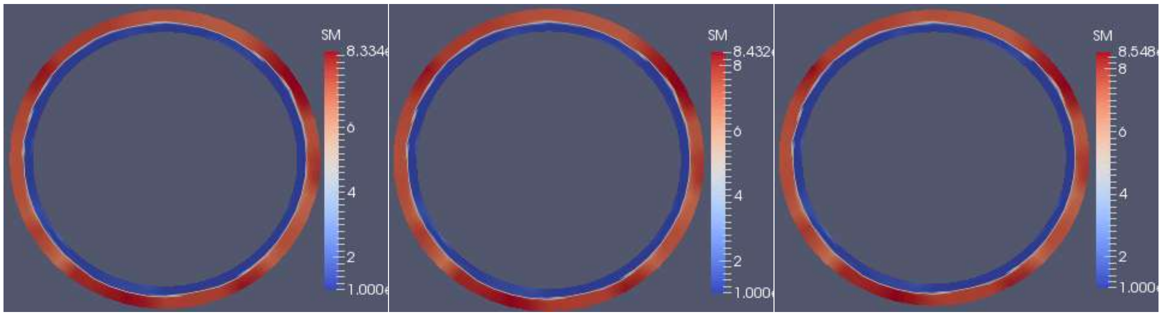

(a) α=1e-12 (b) α=9e-13 (c) α=8e-13

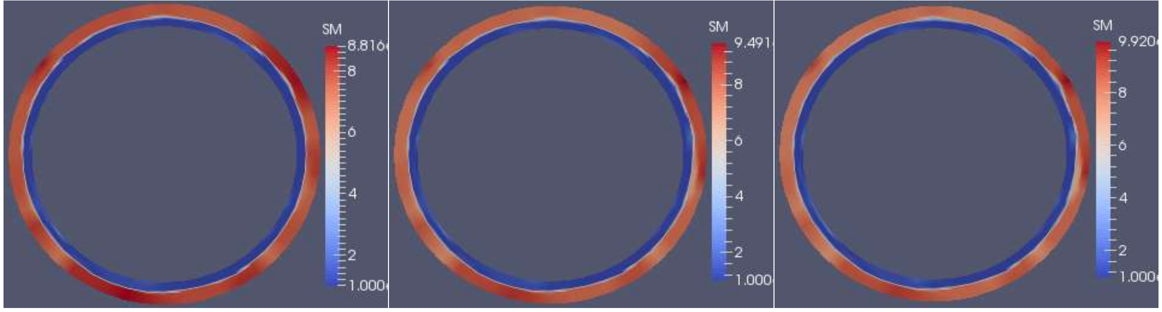

(d) α=7e-13 (e) α=6e-13 (f) α=5e-13

Figure 3.71 Shear modulus reconstruction from element-wise defined material with a coarse mesh and 1% noise

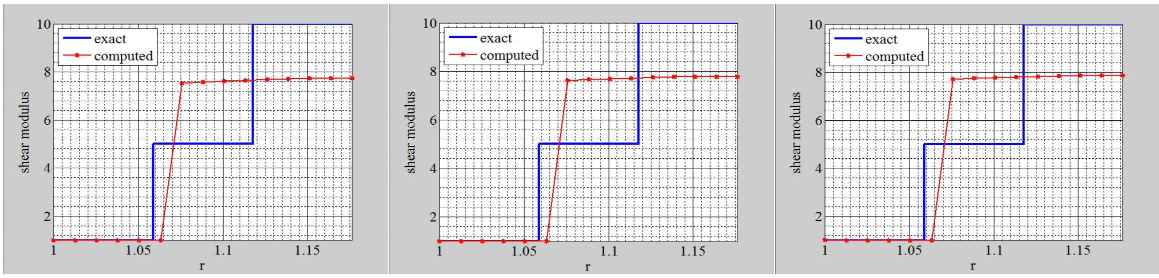

(a) α=1e-12 (b) α=9e-13 (c) α=8e-13

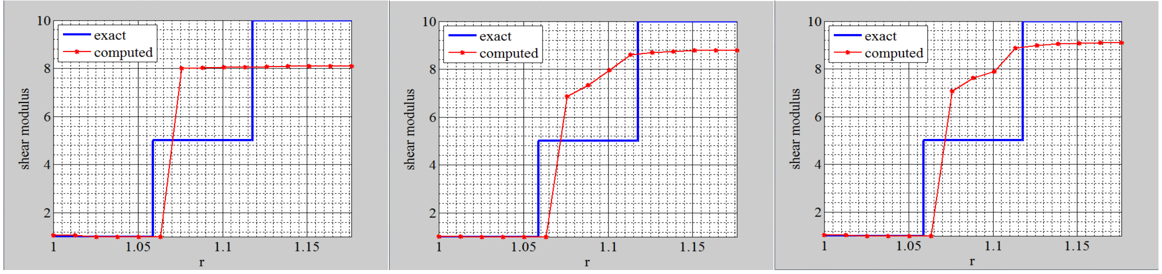

(d) α=7e-13 (e) α=6e-13 (f) α=5e-13

Figure 3.72 Shear modulus reconstruction from element-wise defined material with a coarse mesh and 1% noise along the radial direction

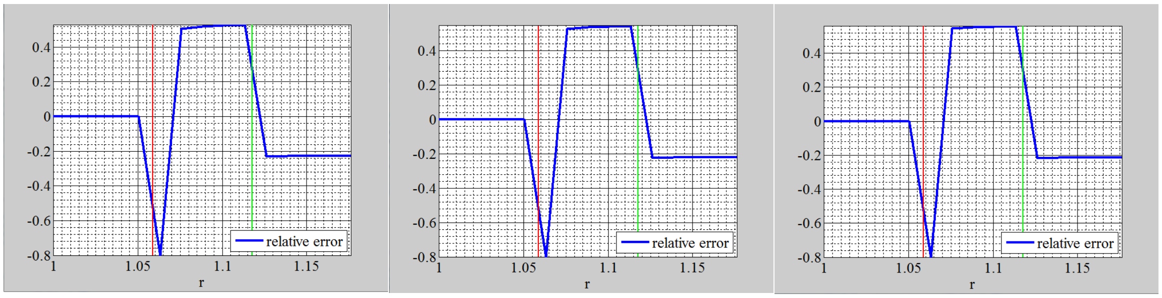

(a) α=1e-12
Relative error = 37.78%

(b) α=9e-13
Relative error = 37.09%

(c) α=8e-13
Relative error = 36.51%

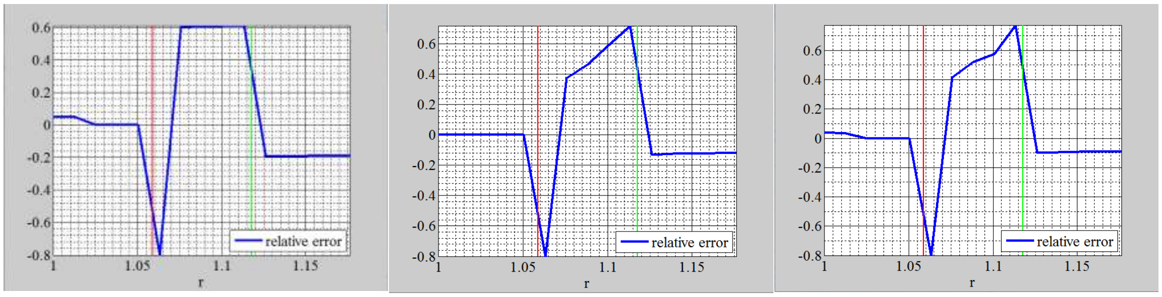

(d) α=7e-13
Relative error = 35.37%

(e) α=6e-13
Relative error = 34.42%

(f) α=5e-13
Relative error = 33.53%

Figure 3.73 Relative spatial error in the shear modulus with a coarse mesh and 1% noise in the displacement field

For the displacement field with 3% noise the shear modulus reconstruction is plotted in Figure 3.74. It can be observed that reconstructions are not in good agreement with the exact distributions. The border of each layer is not well recovered. In order to illustrate the change of the shear modulus in the border of each layer, Figure 3.75 shows the reconstruction of the shear modulus from the element-wise defined material in radial direction. The relative spatial error in the shear modulus is plotted in the Figure 3.76.

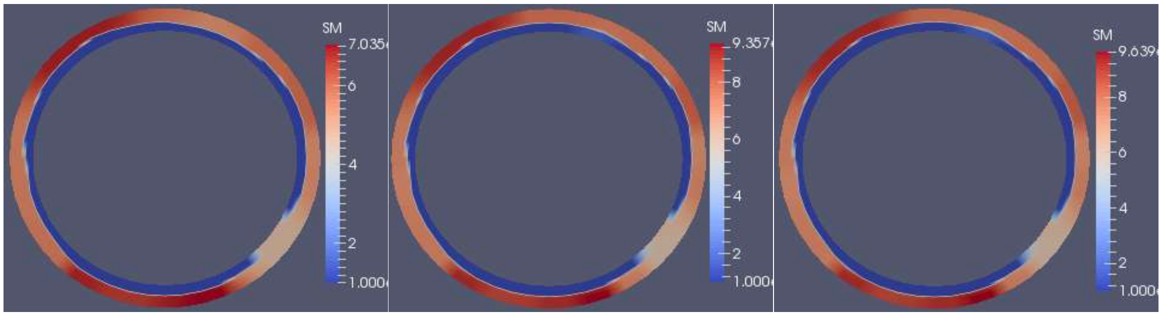

(a) α=2e-11 (b) α=1e-11 (c) α=9e-12

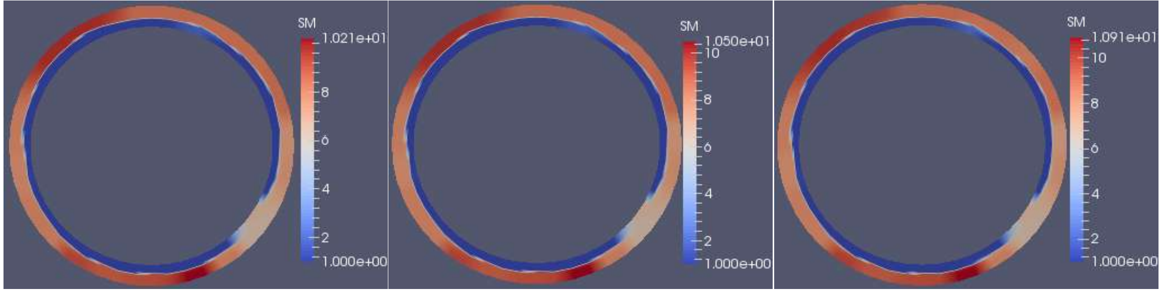

(d) α=8e-12 (e) α=7e-12 (f) α=6e-12

Figure 3.74 Shear modulus reconstruction from element-wise defined material with a coarse mesh and 3% noise

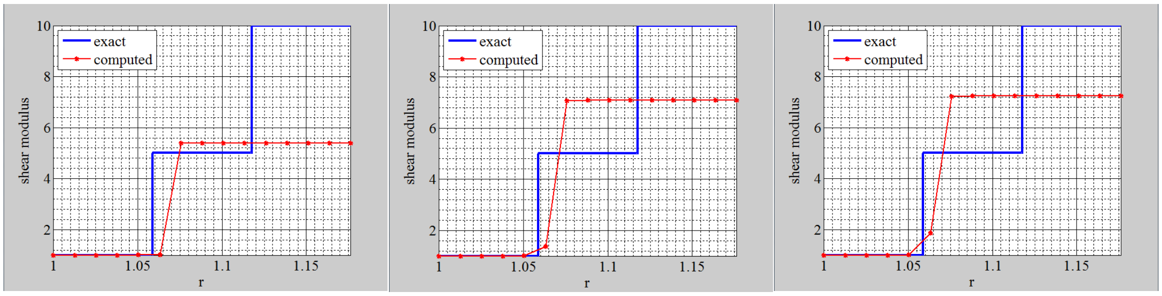

(a) α=2e-11 (b) α=1e-11 (c) α=9e-12

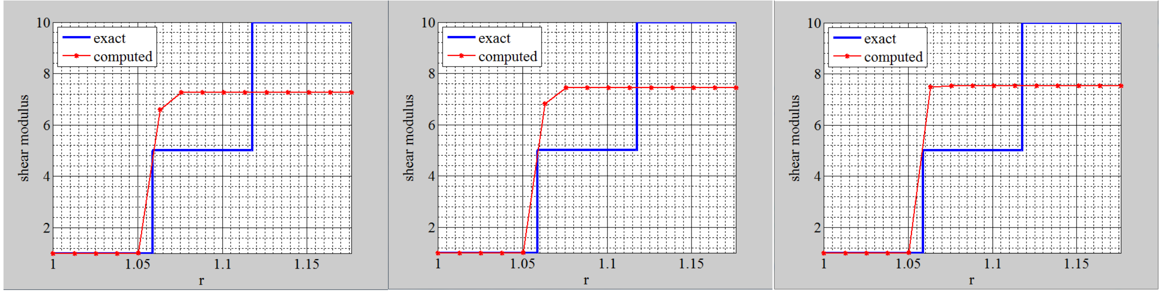

(d) α=8e-12 (e) α=7e-12 (f) α=6e-12

Figure 3.75 Shear modulus reconstruction from element-wise defined material with a coarse mesh and 3% noise along the radial direction

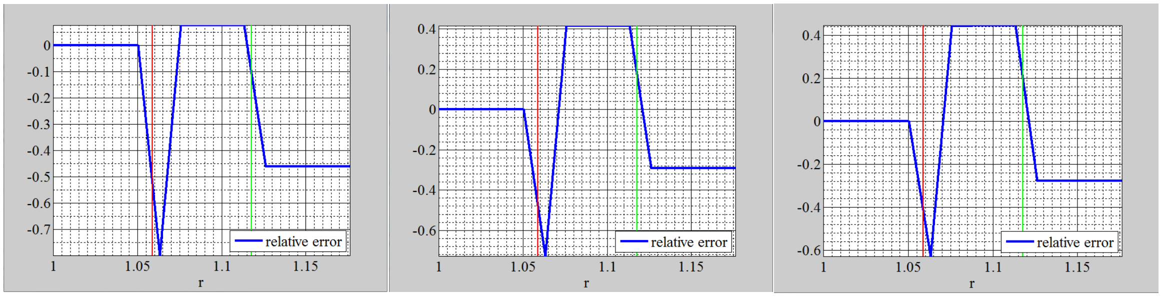

(a) α=2e-11
Relative error = 58.21%

(b) α=1e-11
Relative error = 38.63%

(c) α=9e-12
Relative error = 37.76%

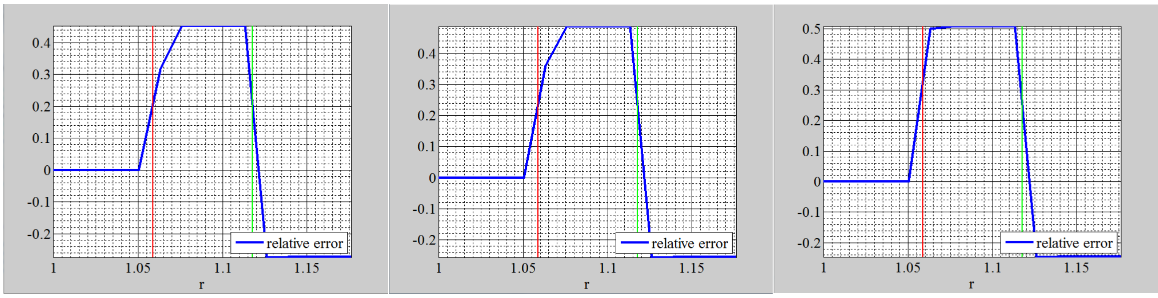

(d) α=8e-12
Relative error = 36.62%

(e) α=7e-12
Relative error = 36.26%

(f) α=6e-12
Relative error = 35.80%

Figure 3.76 Relative spatial error in the shear modulus with a coarse mesh and 3% noise in the displacement field

In Figure 3.77 the reconstruction of the shear modulus is presented for the fine mesh. One can observe that the shear modulus reconstruction with the fine mesh is much better than the reconstruction with the coarse mesh. Figure 3.78 shows the shear modulus value plotted along the radial direction. In Figure 3.79 the relative spatial error in the shear modulus is visualized spatially. Here, the relative error does not change much as the mesh is refined, because the reconstruction is already well recovered and the convergence is reached. One can also observe that the shear modulus is reproduced very well with clear layer boundaries. Again, the maximum error occurs at the border of the layers (see Figure 3.79).

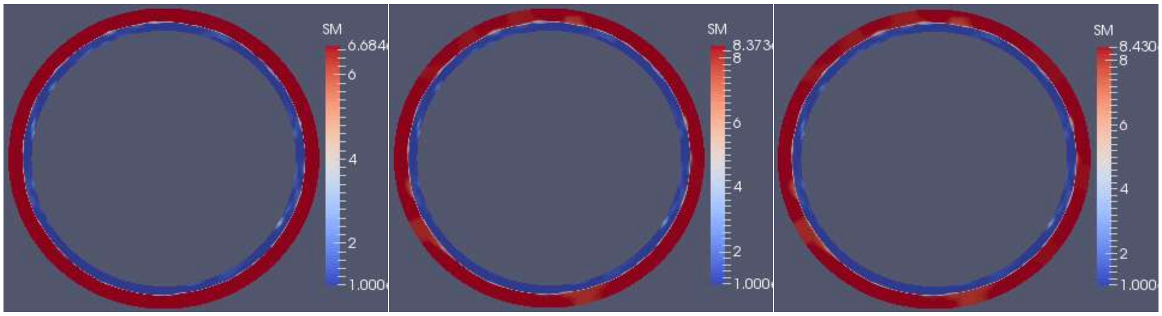

(a) α=1e-11 (b) α=1e-12 (c) α=9e-13

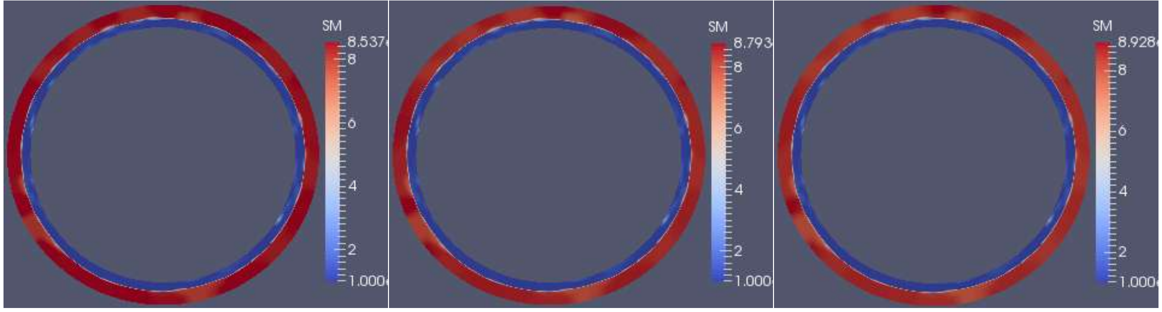

(d) α=8e-13 (e) α=7e-13 (f) α=6e-13

Figure 3.77 Shear modulus reconstruction from element-wise defined material with a fine mesh and 1% noise

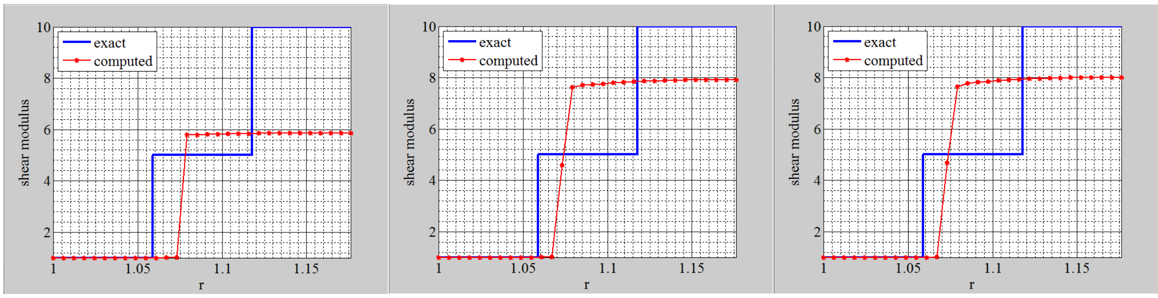

(a) α=1e-11 (b) α=1e-12 (c) α=9e-13

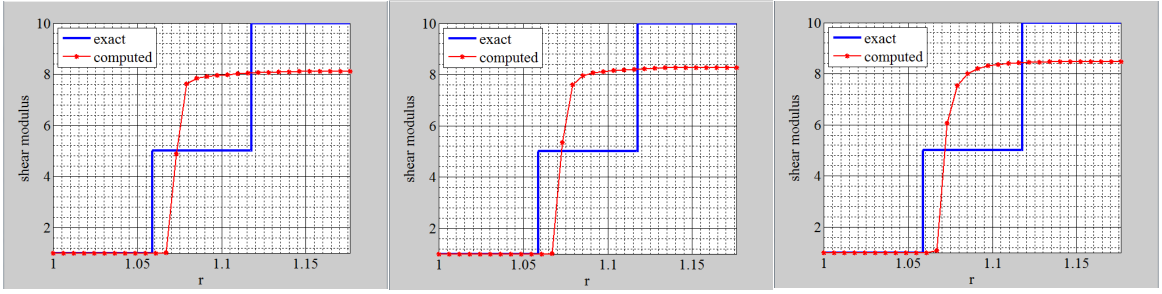

(d) α=8e-13 (e) α=7e-13 (f) α=6e-13

Figure 3.78 Shear modulus reconstruction from element-wise defined material with a fine mesh and 1% noise along the horizontal centerline

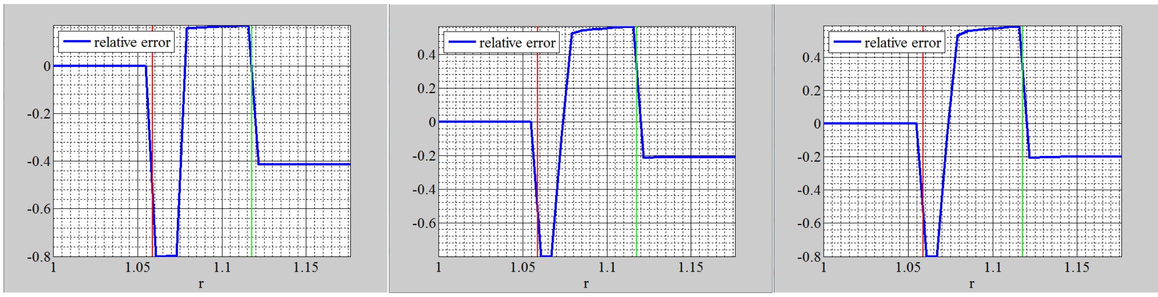

(a) α=1e-11
Relative error = 57.94%

(b) α=1e-12
Relative error = 34.72%

(c) α=9e-13
Relative error = 34.33%

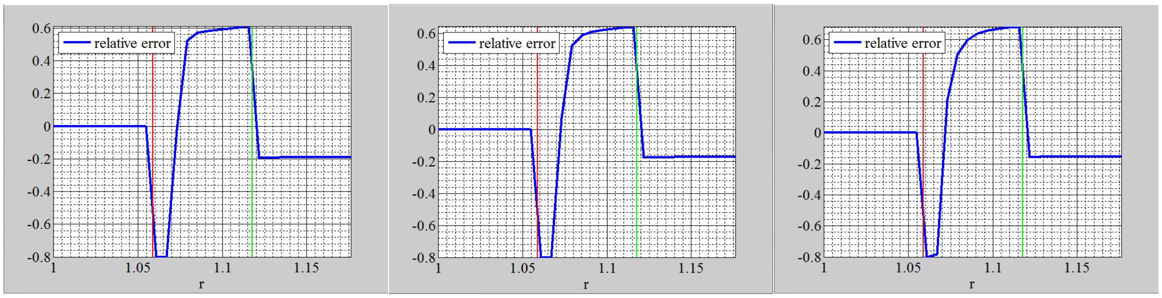

(d) α=8e-13
Relative error = 33.91%

(e) α=7e-13
Relative error = 33.39%

(f) α=6e-13
Relative error = 32.75%

Figure 3.79 Relative spatial error in the shear modulus with a fine mesh and 1% noise in the displacement field

For the displacement field with 3% noise the shear modulus is plotted in Figure 3.80. It can be observed that reconstructions are not in good agreement with the exact distributions. The border between the middle and outer layer is not well recovered. In order to illustrate the change of the shear modulus in the border of the layer, Figure 3.81 shows the reconstruction of the shear modulus plotted along the radial direction. The relative spatial error in the shear modulus is plotted in Figure 3.82.

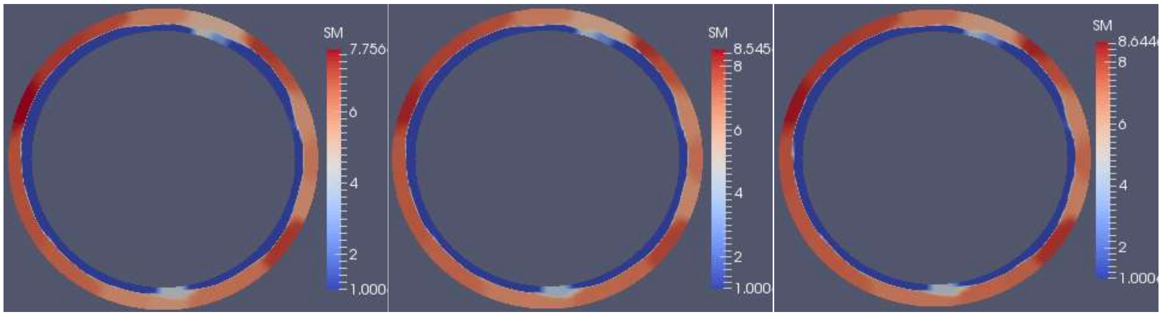

(a) α=1e-11 (b) α=7e-12 (c) α=6e-12

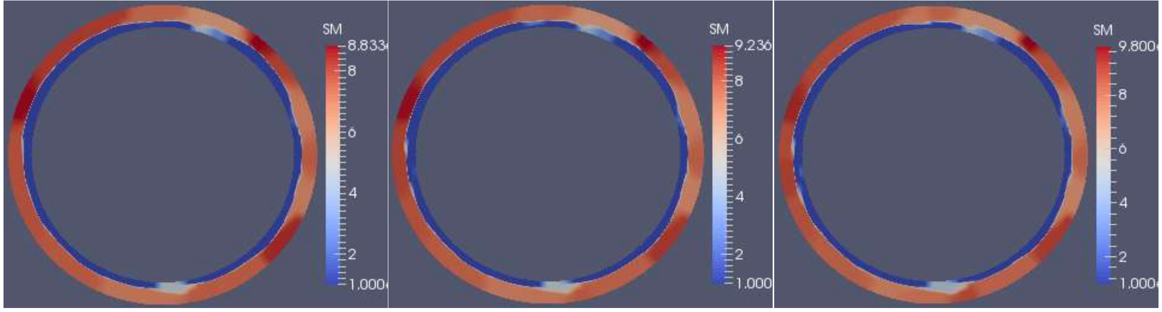

(d) α=5e-12 (e) α=4e-12 (f) α=3e-12

Figure 3.80 Shear modulus reconstruction from element-wise defined material with fine mesh and 3% noise

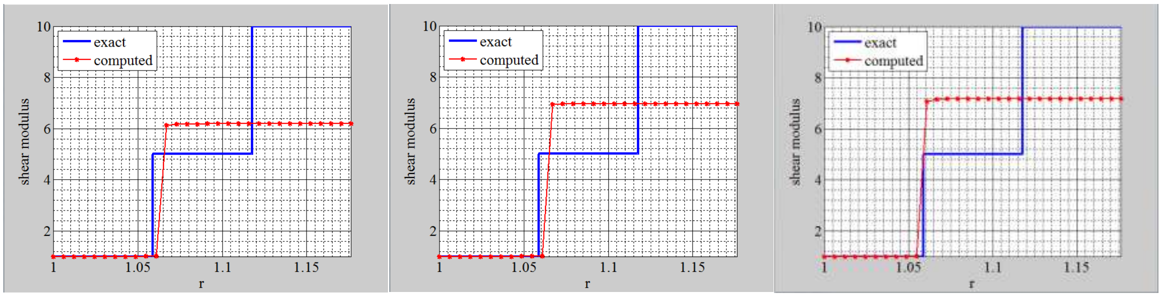

(a) α=1e-11 (b) α=7e-12 (c) α=6e-12

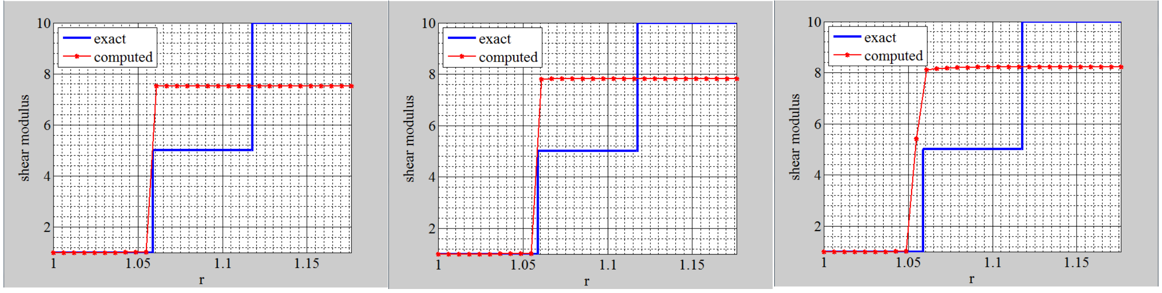

(d) α=5e-12 (e) α=4e-12 (f) α=3e-12

Figure 3.81 Shear modulus reconstruction from element-wise defined material with fine mesh and 3% noise along the horizontal centerline

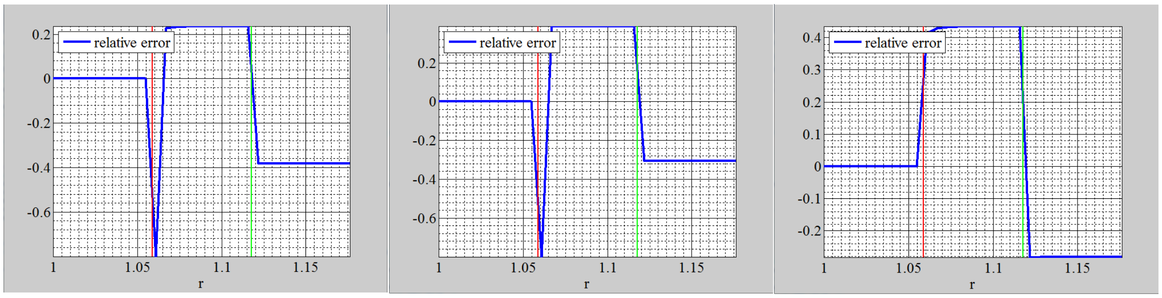

(a) α=1e-11
Relative error = 48.79%

(b) α=7e-12
Relative error = 40.37%

(c) α=6e-12
Relative error = 38.24%

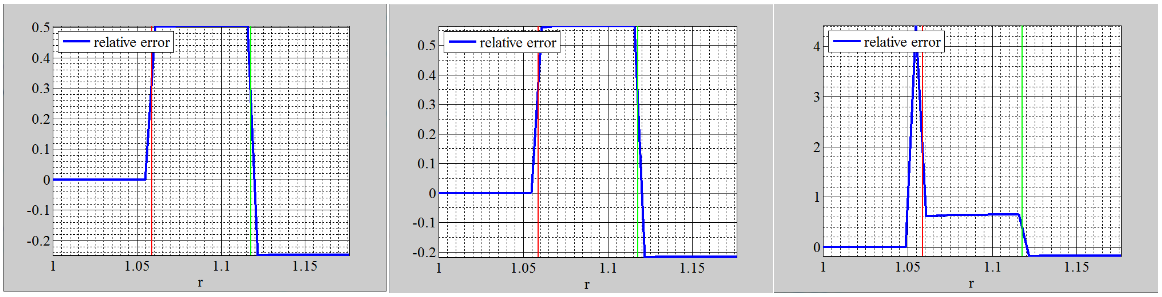

(d) α=5e-12
Relative error = 36.66%

(e) α=4e-12
Relative error = 35.55%

(f) α=3e-12
Relative error = 34.68%

Figure 3.82 Relative spatial error in the shear modulus with a fine mesh and 3% noise in the displacement field

3.2.2.4 Continuously Defined Material with Noised Data

To the displacement field obtained from the continuously defined shear modulus about 1% and 3% noise are added. For the displacement field with 1% noise the shear modulus reconstruction is plotted in Figure 3.83. It can be observed that the reconstructions are not in good agreement with the exact distributions. In order to illustrate the change of the shear modulus at the border of the layers, Figure 3.84 shows the reconstruction of the shear modulus in the radial direction. The relative error is plotted in Figure 3.85. One can observe that the maximum relative error occurs at the border of the layer.

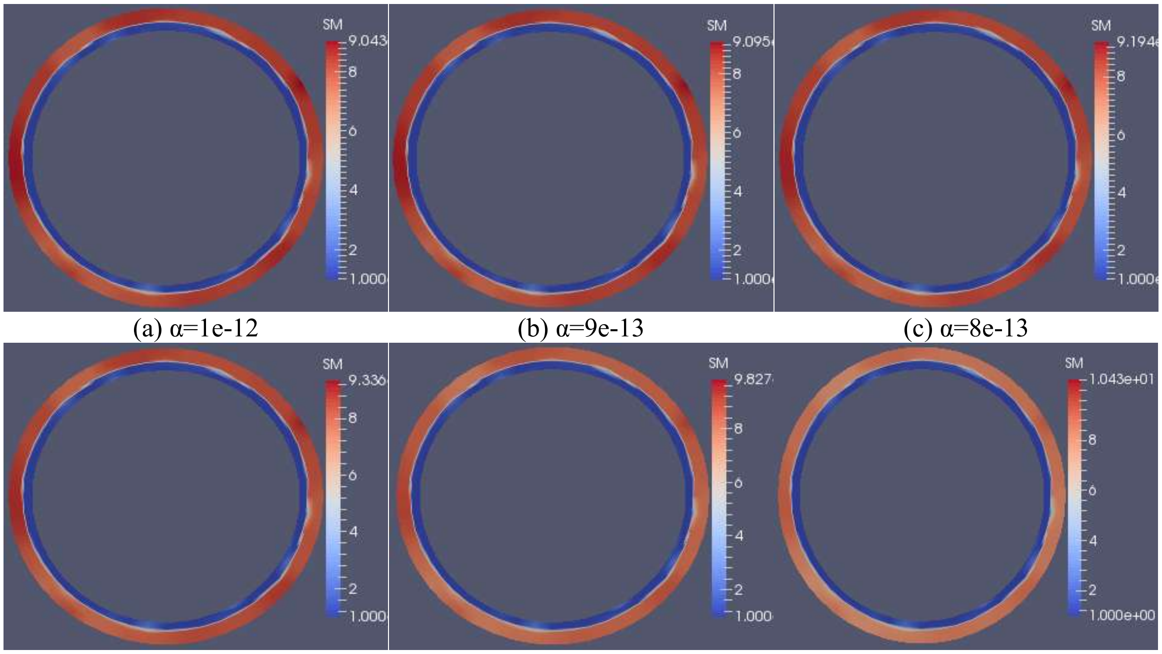

(a) α=1e-12 (b) α=9e-13 (c) α=8e-13

(d) α=7e-13 (e) α=6e-13 (f) α=5e-13

Figure 3.83 Shear modulus reconstruction from continuously defined material with a coarse mesh and 1% noise

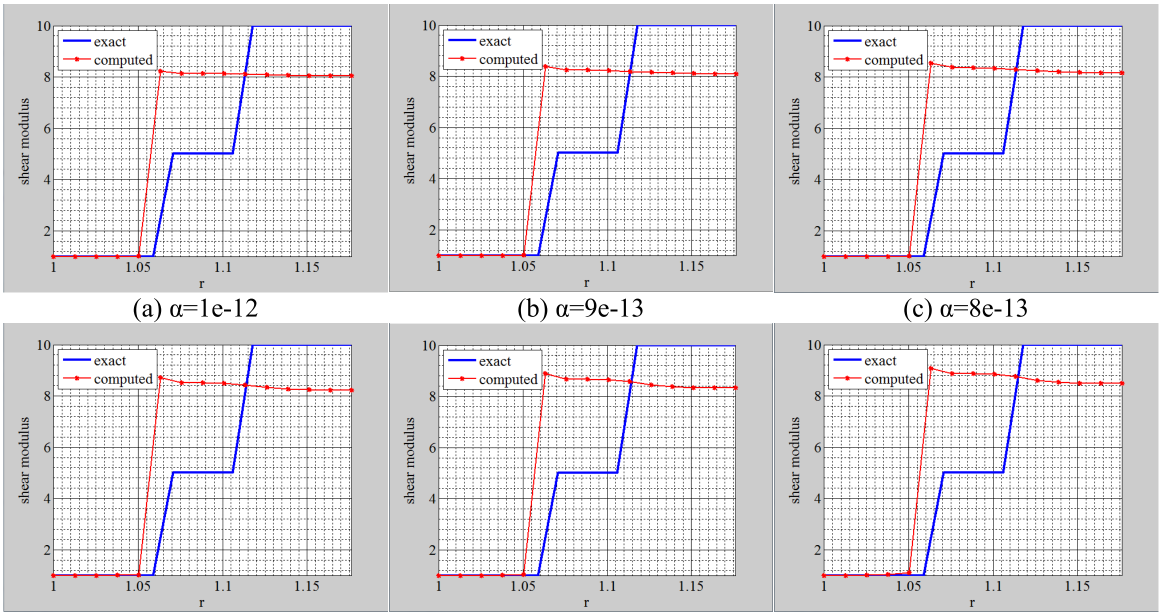

(a) α=1e-12 (b) α=9e-13 (c) α=8e-13

(d) α=7e-13 (e) α=6e-13 (f) α=5e-13

Figure 3.84 Shear modulus reconstruction from continuously defined material with a coarse mesh and 1% noise along the radial direction

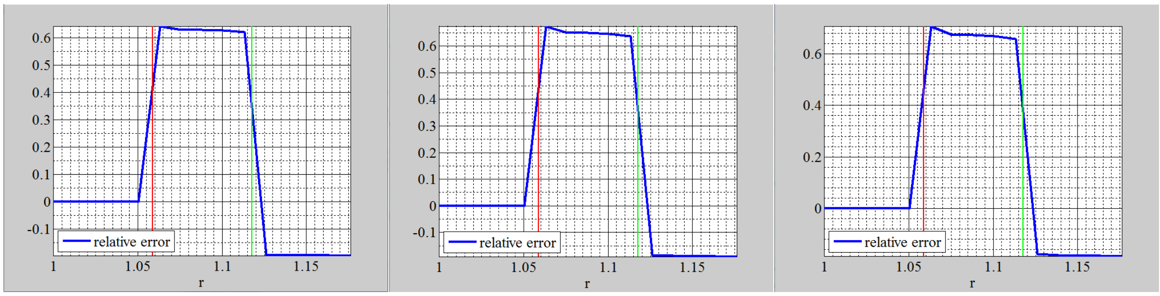

(a) α=1e-12
Relative error = 32.23%

(b) α=9e-13
Relative error = 32.01%

(c) α=8e-13
Relative error = 31.68%

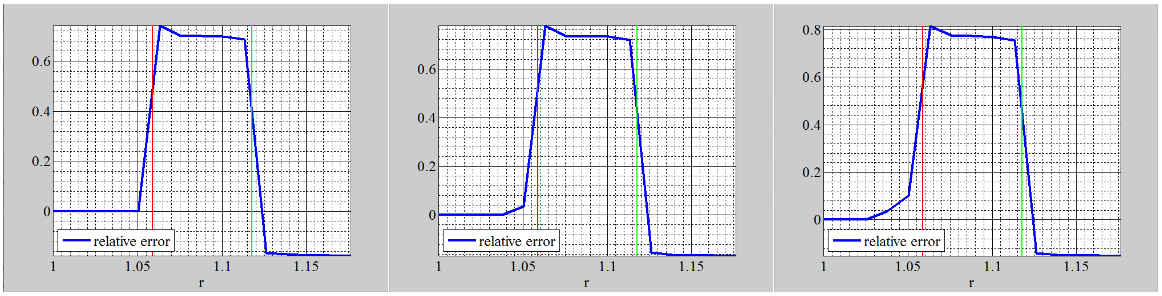

(d) α=7e-13
Relative error = 31.38%

(e) α=6e-13
Relative error = 31.19%

(f) α=5e-13
Relative error = 31.13%

Figure 3.85 Relative spatial error in the shear modulus with a coarse mesh and 1% noise in the displacement field

For the displacement field with 3% noise the shear modulus is plotted in Figure 3.86 for different regularization factors. It can be observed that the shear modulus reconstructions are not in good agreement with the exact distributions. The shear modulus values are poorly recovered as well as their interfaces between the layers. Figure 3.87 visualizes the change of the shear modulus along the thickness, i.e. in radial direction. The relative spatial error in the shear modulus is plotted in Figure 3.88.

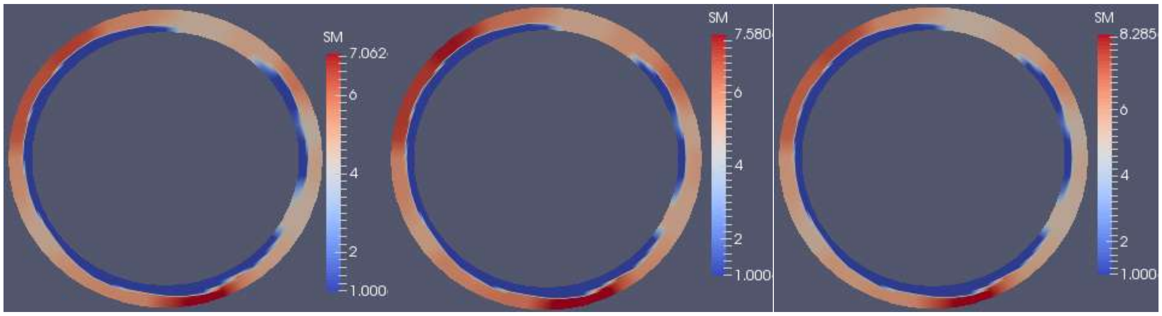

(a) α=2e-11 (b) α=1.8e-11 (c) α=1.6e-11

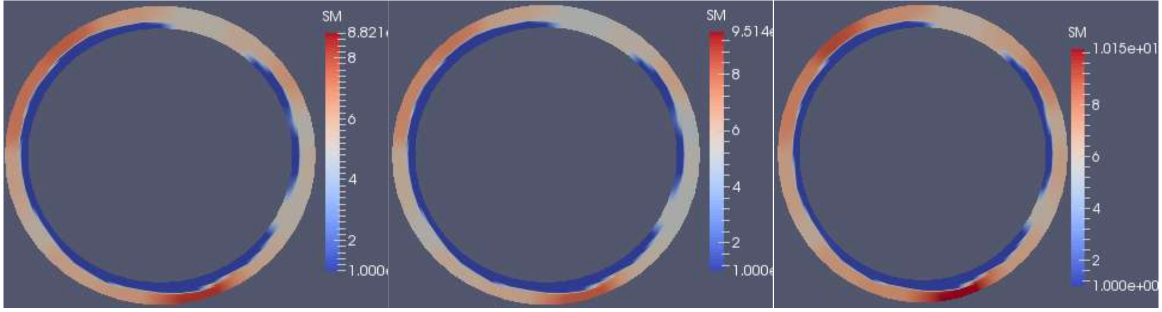

(d) α=1.4e-11 (e) α=1.2e-11 (f) α=1e-11

Figure 3.86 Shear modulus reconstruction from continuously defined material with a coarse mesh and 3% noise

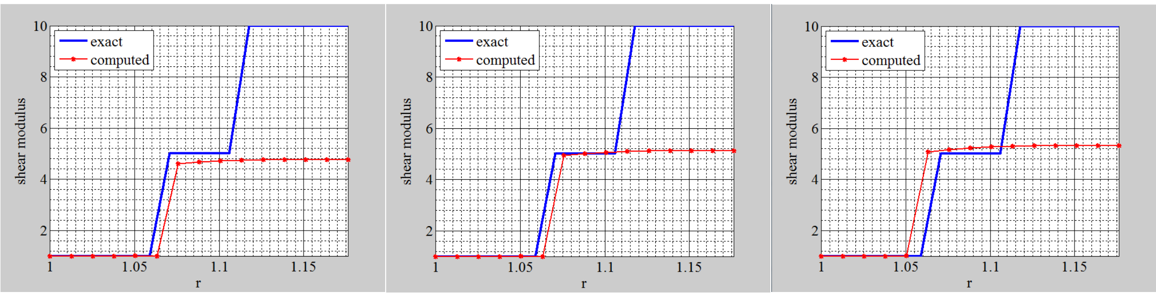

(a) α=2e-11 (b) α=1.8e-11 (c) α=1.6e-11

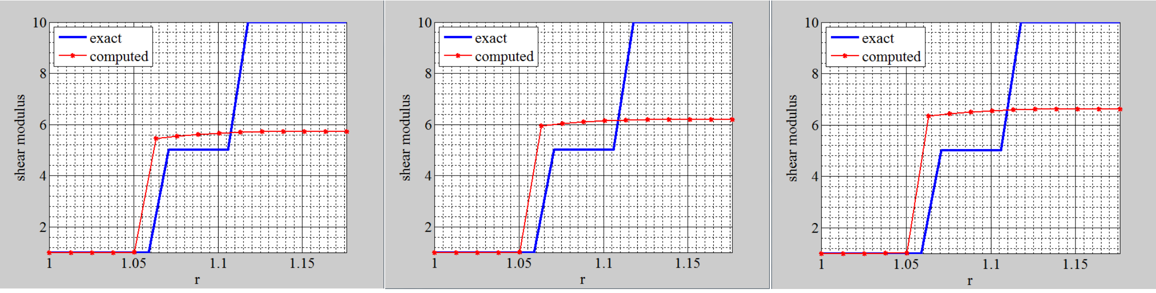

(d) α=1.4e-11 (e) α=1.2e-11 (f) α=1e-11

Figure 3.87 Shear modulus reconstruction from continuously defined material with a coarse mesh and 3% noise along the horizontal centerline

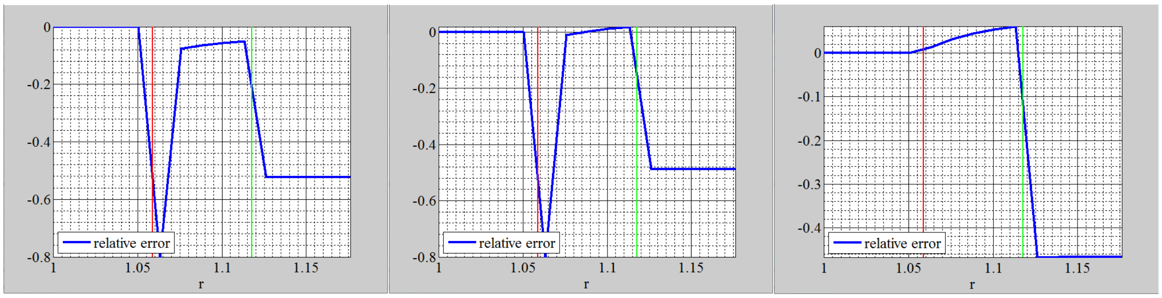

(a) α=2e-11
Relative error = 70.80%

(b) α=1.8e-11
Relative error = 63.52%

(c) α=1.6e-11
Relative error = 55.82%

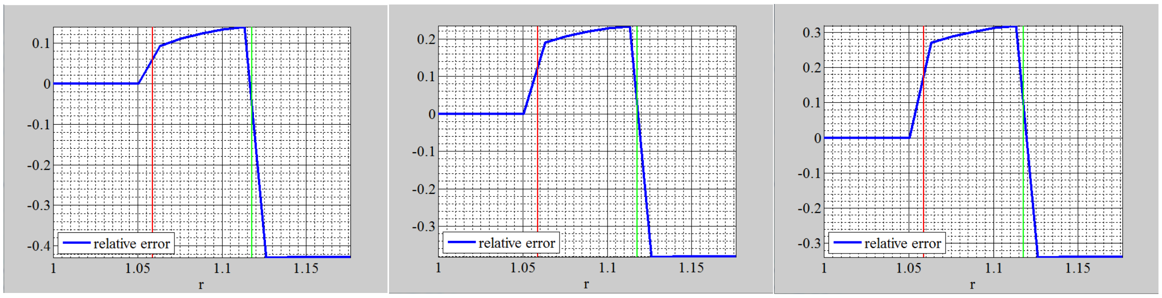

(d) α=1.4e-11
Relative error = 50.84%

(e) α=1.2e-11
Relative error = 45.91%

(f) α=1e-11
Relative error = 42.81%

Figure 3.88 Relative spatial error in the shear modulus with a coarse mesh and 3% noise in the displacement field

Figure 3.89 shows the reconstruction of the shear modulus with different regularization factors using a fine mesh. Figure 3.90 represents the shear modulus plotted along the radial direction. In Figure 3.91 the relative error in the shear modulus is visualized in radial direction. Comparing this to the results with the coarse mesh, the relative error does not change much as the mesh is refined. One can clearly observe that the shear modulus is not reproduced, i.e. the shear modulus values are far off from the target shear modulus values and the interface between the layers are not resolved properly. The maximum error occurs at the border between the inclusion and the background (see Figure 3.91).

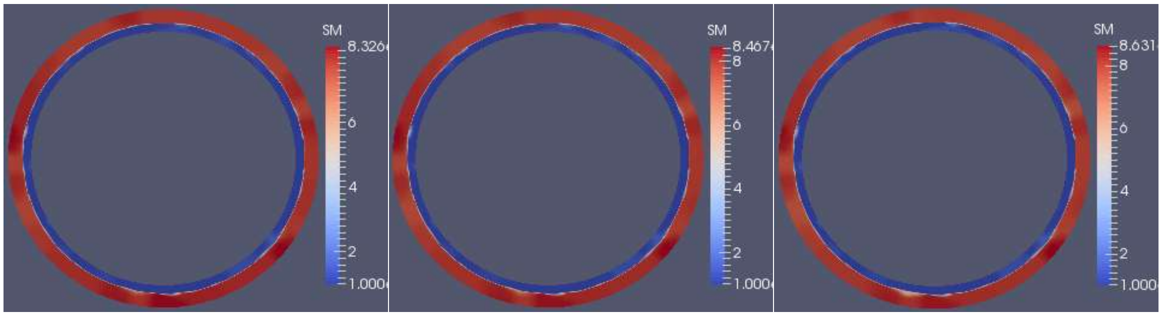

(a) α=1e-12 (b) α=9e-13 (c) α=8e-13

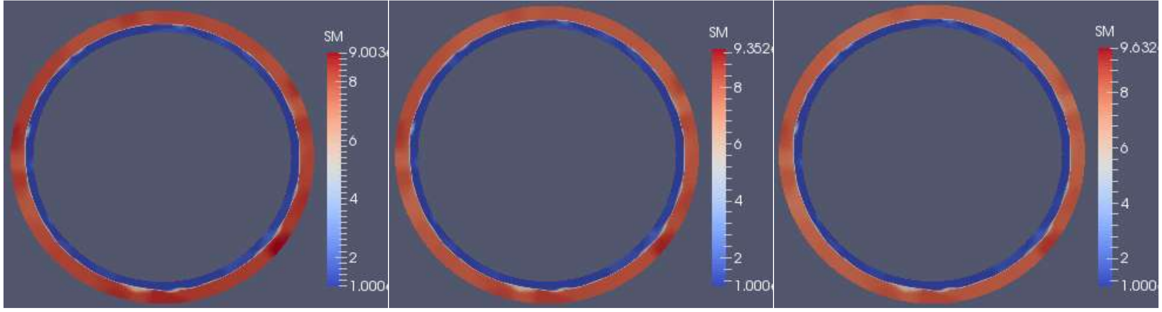

(d) α=7e-13 (e) α=6e-13 (f) α=5e-13

Figure 3.89 Shear modulus reconstruction from continuously defined material with a fine mesh and 1% noise

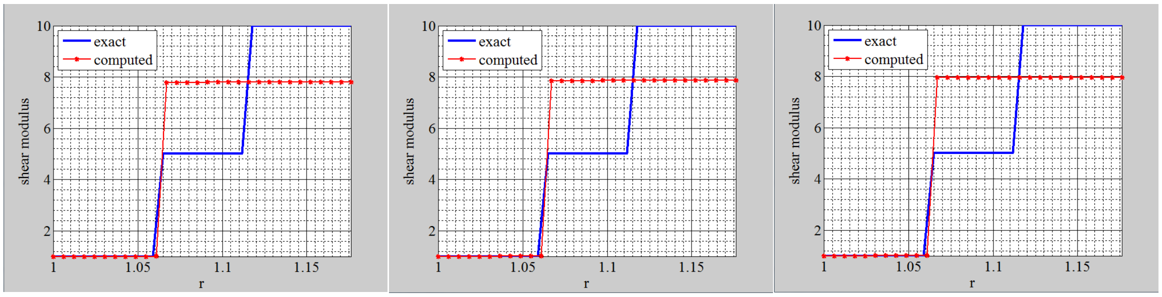

(a) α=1e-12 (b) α=9e-13 (c) α=8e-13

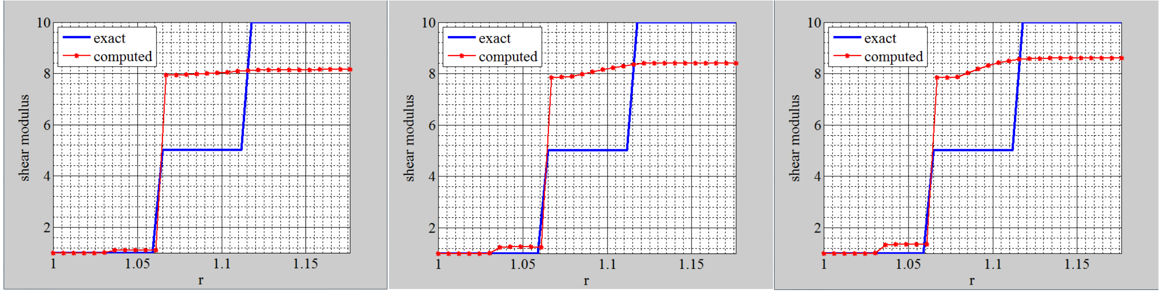

(d) α=7e-13 (e) α=6e-13 (f) α=5e-13

Figure 3.90 Shear modulus reconstruction from continuously defined material with a fine mesh and 1% noise along the horizontal centerline

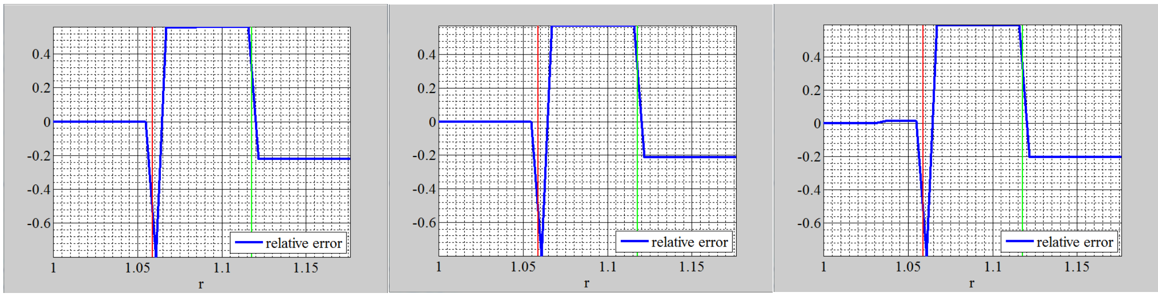

(a) α=1e-12
Relative error = 33.37%

(b) α=9e-13
Relative error = 33.04%

(c) α=8e-13
Relative error = 32.60%

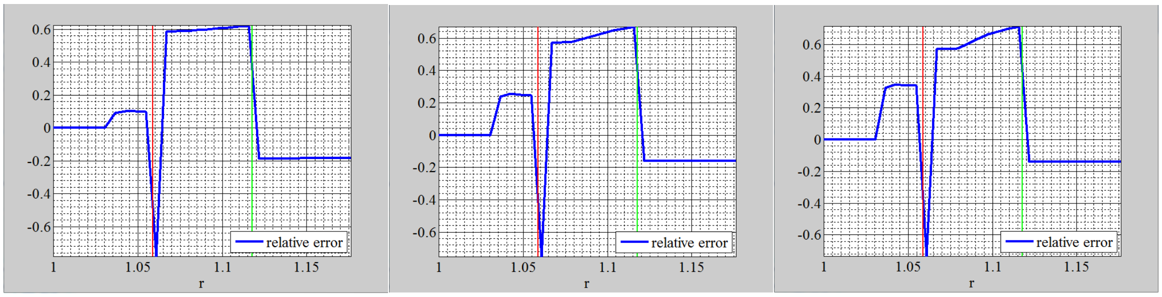

(d) α=7e-13
Relative error = 32.11%

(e) α=6e-13
Relative error = 31.63%

(f) α=5e-13
Relative error = 31.28%

Figure 3.91 Relative spatial error in the shear modulus with a fine mesh and 1% noise in the displacement field

For the displacement field with 3% noise the shear modulus reconstruction is plotted for different regularization factors in Figure 3.92 for the fine mesh. It can be observed that the reconstructions are not in good agreement with the exact distributions. The border of the middle and outer layer is not well recovered. In order to clearly visualize the change in the shear modulus between these layers Figure 3.93 is provided, representing the shear modulus reconstruction along a radial direction. The relative spatial error in the shear modulus is plotted in Figure 3.94.

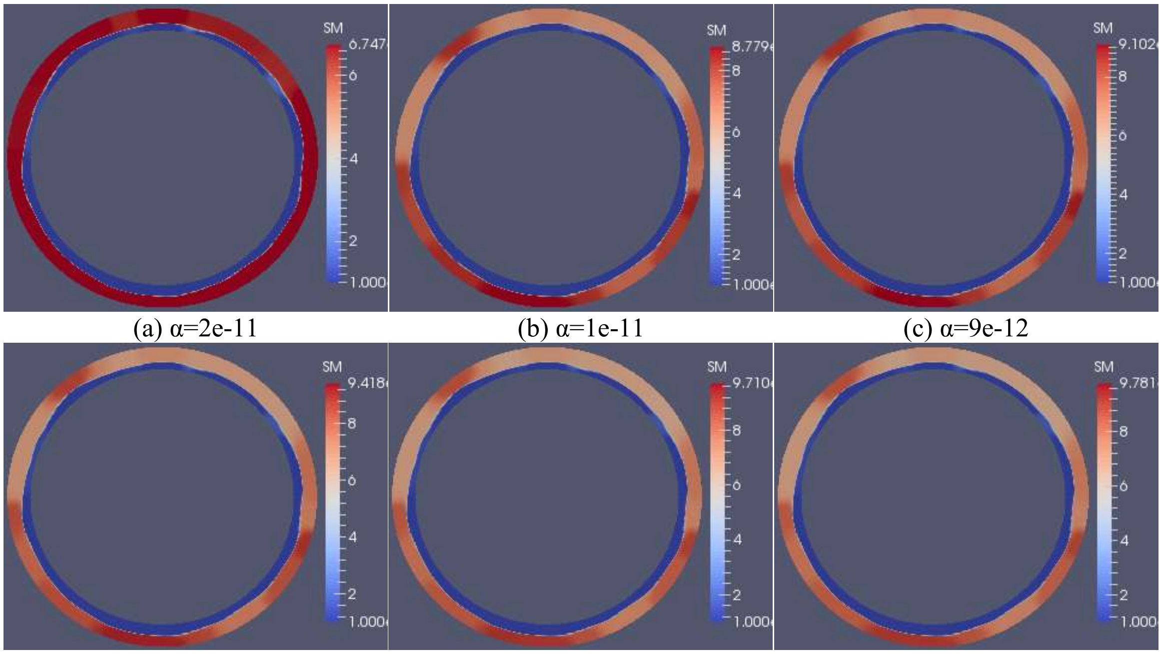

(a) α=2e-11 (b) α=1e-11 (c) α=9e-12

(d) α=8e-12 (e) α=7e-12 (f) α=6e-12

Figure 3.92 Shear modulus reconstruction from continuously defined material with fine mesh and 3% noise

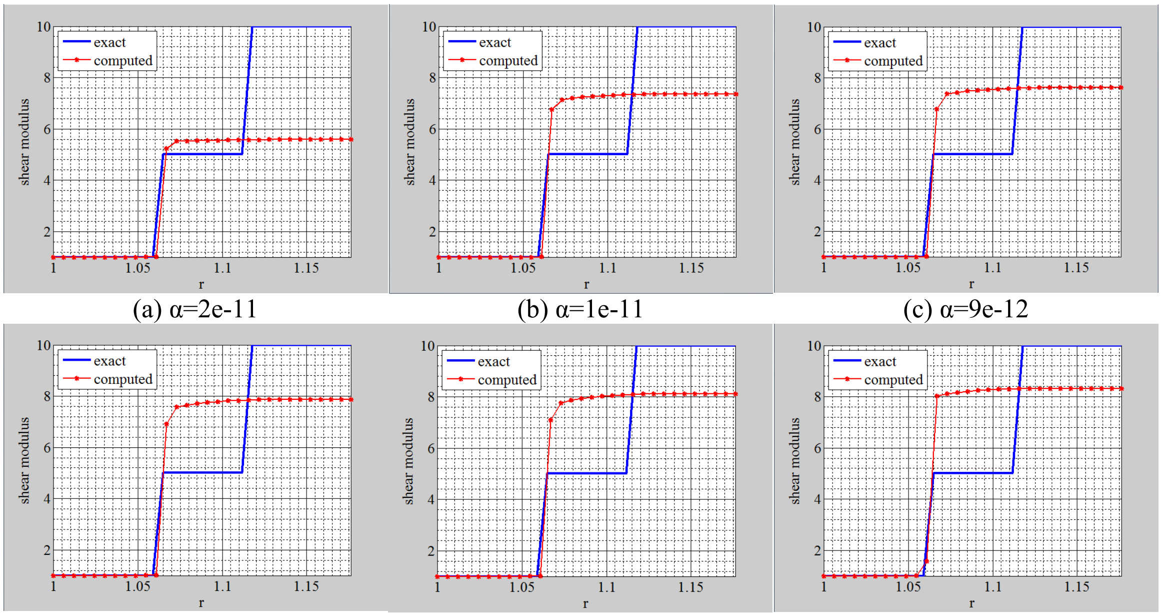

(a) α=2e-11 (b) α=1e-11 (c) α=9e-12

(d) α=8e-12 (e) α=7e-12 (f) α=6e-12

Figure 3.93 Shear modulus reconstruction from continuously defined material with fine mesh and 3% noise along the horizontal centerline

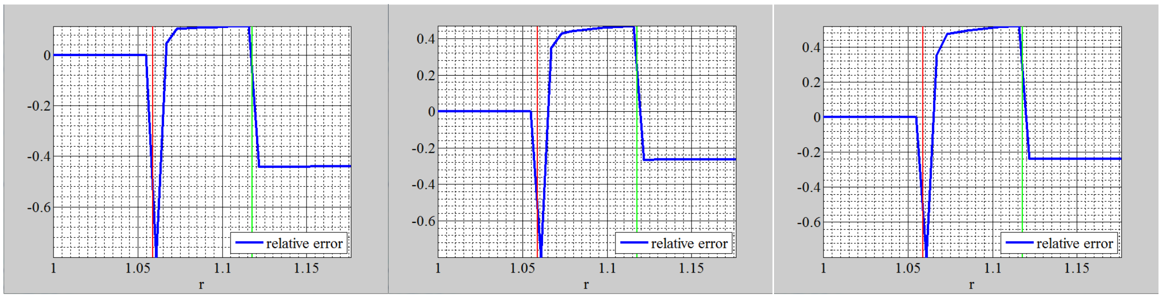

(a) α=2e-11
Relative error = 60.71%

(b) α=1e-11
Relative error = 39.53%

(c) α=9e-12
Relative error = 38.03%

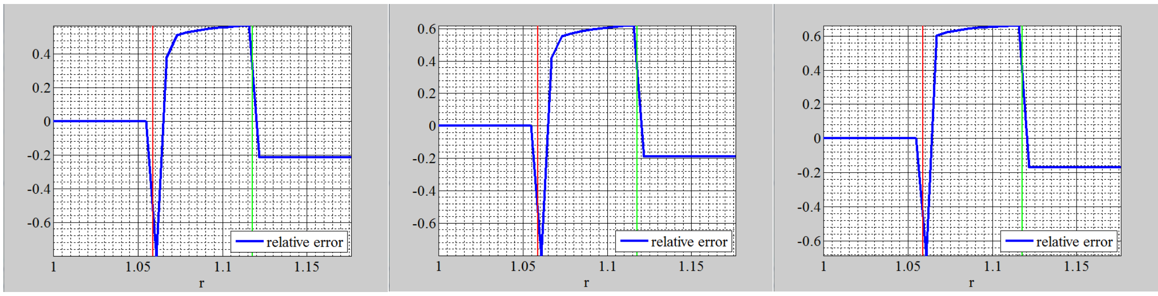

(d) α=8e-12
Relative error = 36.76%

(e) α=7e-12
Relative error = 35.89%

(f) α=6e-12
Relative error = 34.93%

Figure 3.94 Relative spatial error in the shear modulus with a fine mesh and 3% noise in the displacement field

4. DISCUSSION, CONCLUSIONS AND FUTURE WORK

In this thesis, the effect of defining the shear modulus distribution continuously versus discontinuously in the problem domain for non-homogeneous solids has been studied on two models using finite element techniques. For the continuously defined method, the shear modulus values are prescribed at the finite element mesh nodes and interpolated with bilinear shape functions. For the discontinuous method, the shear modulus is defined element-wise, i.e. constant on finite elements, as is common in most commercial finite element method software.

The finite element forward problem has been solved for both shear modulus distributions (continuous and discontinuous) and the strain difference between them has been studied. Afterwards, the resulting displacement field from the continuously and element-wise defined shear modulus distribution has been utilized to solve the inverse problem in elasticity, i.e. to recover the shear modulus distribution.

4.1 Discussion

The inverse problem is solved as a constrained minimization problem as follows: Say we have n measured (numerical) displacement fields $u^1_{meas}, \ldots, u^n_{meas}$, find the shear modulus μ such that the objective function

$$\pi = \frac{1}{2}\sum_{i=1}^{n} w_i \left\| Tu^i - Tu^i_{meas} \right\|_0^2 + \frac{1}{2}\alpha \int_{\Omega_0} \sqrt{\left|\nabla\mu\right|^2 + c^2}\, d\Omega_0 \tag{4.1}$$

is minimized based on the predicted displacement fields satisfying the equations of equilibrium and boundary conditions. The first term of the objective function minimizes the difference between the predicted and the measured displacement. The second term is a regularization term used to ensure the smoothness of the reconstructed materials.

Before solving the inverse problem and analyzing the shear modulus reconstruction, the strain difference computed with element-wise and continuously defined material is analyzed obtained by solving the finite element forward problem. The accuracy of the shear modulus distribution using element-wise and continuously defined material as ground truth is evaluated afterwards solving the inverse problem. The forward problem, discussed in Section 3.1, is solved for the displacement field and the strain in horizontal direction computed. Then the difference in the strain between the two different shear modulus distributions is assessed using two models. The inverse problem, discussed in Section 3.2, is solved to get the shear modulus reconstruction from the continuous and discontinuous target shear modulus distribution in these models. The nonlinear parameter γ is set to zero as this study is concerned with only a linear material behavior. The objective function shown in Eq. 2.3 is minimized using only the vertical displacement field. This reveals the power of the inverse problem formulation as it does not require all displacement components for the inversion process. This is in particular important when the displacement data is obtained from ultrasound measurements, because the displacement component along the ultrasound transducer beam is of much higher quality than the displacement component perpendicular to it. Thus, it would make sense to discard the highly noisy displacement component from the inversion procedure. The reconstruction of the shear modulus for model 1 with both element-wise and continuously defined material using noise free data are presented in Figure 3.11 through 3.26. The reconstructions of the shear modulus for model 1 with both element-wise and continuously defined material using different levels of noised data are presented in Figure 3.27 through 3.58. The mesh then is refined by increasing the number of mesh nodes by a factor of 2 in each lateral and horizontal direction of the square domain. The coarse mesh has 961 total nodes, while the fine mesh has 3721 total nodes. The area of the square domain is 1. The reconstructions of the shear modulus for model 2 with both element-wise and continuously defined material with noise free data are presented in Figure 3.59 through 3.70. The reconstructions of the shear modulus for model 2 with both element-wise and continuously defined material with different levels of noised data are presented in Figure 3.71 through 3.94. The mesh is also refined for this model by a factor of 2 in each radial and circumferential direction of the ring domain. The coarse mesh has 720 total nodes, while the fine mesh has 2880 total nodes. Table 3.1 lists the material properties of each layer of model 2. Different regularization parameters for the shear modulus reconstruction are used to select the reconstruction with the best smoothness criteria. It is observed that the value of the reconstructed shear modulus contrast increases as the regularization parameter decreases.

The soft tissue in both problems is modeled with geometric nonlinearity for an incompressible material in plane stress. When solving the inverse problem, it is assumed that the shear modulus distribution is continuous over the problem domain. In other words, the shear modulus is unknown on the mesh nodes and interpolated here with bilinear shape functions. The ground truth (target shear modulus distribution) on the other hand is defined with the continuous and element-wise shear modulus distribution. In Figure 3.11 and 3.14, the reconstructions from the element-wise defined target shear modulus distribution with noise free data are presented for model 1. The shear modulus contrast is clearly recovered and the inclusion shape is well resolved. In Figure 3.19 and 3.23, the reconstructions from the continuously defined target shear modulus distribution with noise free data is presented. Again, the shear modulus contrast is clearly recovered and the inclusion shape is well resolved. With the noised data shown in Figure 3.27 and 3.31, the shear modulus contrast decreases because of the larger regularization parameter. With increasing noise levels, the coarse mesh does not recover the shape of the inclusion well. However, after refining the mesh in Figure 3.35 and 3.39, the inclusion shape improves significantly, while the shear modulus contrast does not increase much. In model 2, the shear modulus between the middle and outer layer is of poor quality with noised data. This is because the ratio of the shear modulus between the outer layer and middle layer is only 2, while the ratio of the shear modulus between the middle and inner layer is 5. Thus it seems to be "easier" to recover the higher contrast in the shear modulus. Furthermore, in those shear modulus reconstructions, the different values of the regularization parameters result in different shear modulus contrasts. When the value of the regularization parameter increases, the shear modulus contrast decreases. This is because the regularization parameter penalizes the difference or changes in the shear modulus reconstruction. On the other hand, decreasing the regularization parameter results in oscillations and fluctuations of the shear modulus distribution when noisy displacement data is utilized. Thus, the right choice of the TVD regularization parameter is a trade-off between contrast and smoothness. A good choice of this parameter will give the accurate information about the soft tissue detected.

Finally, the stiff inclusion in model 1 could represent a tumor. And this has been shown to be reconstructed well with a fine mesh despite of high noise levels in the displacement field. This indicates the potential of using the shear modulus in detecting tumors as a medical modality.

4.2 Conclusions

In this thesis, the forward and inverse problem are solved with both element-wise and continuously defined materials to assess the strain and the shear modulus reconstruction. The effect of mesh refinement is tested to see if the solution improves. The effect of noise in two different models is also tested to simulate real noisy measured displacement data from medical devices, such as ultrasound devices, magnetic resonance imaging and optical coherence tomography (OCT). The tissue in these two models is modeled as an incompressible material in 3D in a state of plane stress. The performance of the shear modulus reconstruction can be improved, so that the potential of the elasticity imaging in the medical field is emerging. The inclusion in model 1, representing a stiffer tumor in a uniform background, can be found and located in the shear modulus reconstructions. Thus, these reconstructed images can potentially be used to detect tumors in the medical field. Following conclusions can be given about these reconstructed shear modulus images. First, the total relative error is much larger for the element-wise defined material. Second, the total relative error decreases when the mesh is refined for the element-wise defined material. Third, the total relative error remains similar when the mesh is refined for continuously defined material. Last but not least, the maximum spatial error occurs at the interfaces of shear modulus changes and does not significantly reduce with mesh refinement.

4.3 Future Work

As future work, two questions need to be answered: 1) Why does model 2 (layered ring model) perform worse? 2) How can the reconstructions using noised data be improved? Solving the first problem can potentially improve the performance of detecting diseased tissues such as atherosclerotic plaques in blood vessels. The second question is important because medical devices, like ultrasound, in general acquire highly noisy displacement fields. By solving these problems, the accuracy of tumor detection in elasticity imaging can be significantly improved. Future work also comprises the extension of this study to other models, such as skin cancer, liver cirrhosis, liver tumors, prostate cancer, etc.

Since the size of some tissues such as cardiovascular tissue is significantly larger in the axial direction comparing with that of the cross section perpendicular to the axial direction, it would also be desirable to model the tissue in plane strain and perform this study to analyze the shear modulus reconstruction from the element-wise and continuously defined shear modulus distributions. Furthermore, a way to define element-wise material to solve the inverse problem will be developed for characterizing discontinuous shear modulus distribution in the domain of interest. This will clearly reduce the errors in the shear modulus reconstructions if the ground truth is actually a discontinuously defined shear modulus distribution. Finally, the models in this thesis assumed the material (tissues) to be linear elastic. In fact, most tissues such as breast tumors, skin, arteries are nonlinear and viscoelastic. Thus, the study needs to be extended to nonlinear solids and the inverse problem must be enriched to take into account viscoelastic material behavior.

REFERENCES

[1] J. Ophir, I. Céspedes, H. Ponnekanti, Y. Yazdi, and X. Li, “Elastography: A quantitative method for imaging the elasticity of biological tissues,” Ultrason. Imaging, vol. 13, no. 2, pp. 111–134, 1991.

[2] D. Morrison, W. McDicken, and D. Smith, “A motion artifact in realtime ultrasound scanners,” Ultrasound in Medicine Biology, vol. 9, no. 2, pp. 201–203, 1983.

[3] R. Dickinson and C. Hill, “Measurement of soft-tissue motion using correlation between A-scans,” Ultrasound in Medicine Biology, vol. 8, no. 3, pp. 263–271, 1982.

[4] Gao L, Parker KJ, Lerner RM, Levinson SF. “Imaging of the elastic properties of tissue – A review.” Ultrasound in Medicine and Biology. 1996; 22:959–977.

[5] Parker KJ, Gao L, Lerner RM, Levinson SF. “Techniques for elastic imaging: a review.” IEEE Engineering in Medicine and Biology Magazine. 1996; 15:52–59.

[6] Wellman, P.; Howe, RH.; Dalton, E.; Kern, KA. Technical Report. Harvard BioRobotics Laboratory, Division of Engineering and Applied Sciences; Harvard University: 1999. “Breast Tissue Stiffness in Compression is Correlated to Histological Diagnosis.”

[7] Samani A, Plewes D. “A method to measure the hyperelastic parameters of ex vivo breast tissue samples.” Physics in Medicine and Biology. 2004; 49:4395–4405.

[8] Y. C. Fung, “Biomechanics: mechanical properties of living tissues”, Springer-Verlag, New York, 1981.

[9] S. Goenezen, “Inverse problems in finite elasticity: an application to imaging the nonlinear elastic properties of soft tissues”

[10] A. A. Oberai, N. H. Gokhale, S. Goenezen, P. E. Barbone, T. J. Hall, A. M. Sommer, and J. Jiang, “Linear and nonlinear elasticity imaging of soft tissue in vivo: demonstration of feasibilty,” Physics in Medicine and Biology. 54 1191-1207, 2009

[11] S. Goenezen, A. Oberai, “Nonlinear Elasticity Imaging”, Bioengineering Conference (NEBEC), 2011 IEEE 37th Annual Northeast

[12] J. Kim, G. Paulino, “Isoparametric graded finite elements for nonhomogeneous isotropic and orthotropic materials”, Journal of Applied Mechanics, 2002

[13] C. Horgan, A. Chan, “The pressurized hollow cylinder or disk problem for functionally graded isotropic linearly elastic materials”, Journal of Elasticity, 1999

[14] C. Vogel, “Computational methods for inverse problem.” Philadelphia, PA, USA: Society of Industrial and Applied Mathematics, 2002

[15] A. E. Adkins, J. E. Green, “Large elastic deformations, and non-linear continuum mechanics”, Oxford Clarenden Press, 1960

[16] J. Ophir, I. Cespedes, B. Garra, H. Ponnekanti, Y. Huang, and N. Maklad, “Elastography: Ultrsonic imaging of tissue strain and elastic modulus in vivo,” European Journal of Ultrasound, vol. 3, no. 1, pp. 49-70, 1996

[17] S. Goenezen, J. F. Dord, Z. Sink, P. E. Barbone, J. Jiang, T. J. Hall, and A. A. Oberai, “Linear and nonlinear elastic modulus imaging: An application to breast cancer diagnosis,” IEEE Transactions on Medical Imaging. 31 8, 1628-37, 2012.

[18] M. J. Paszek, N. Zahir, K. R. Johnson, J. N. Lakins, G. I. Rozenberg, A. Gefen, C. A. Reinhart-King, S. S. Margulies, M. Dembo, D. Boettiger, D. A. Hammer, and V. M. Weaver, “Tensional homeostasis and the malignant phenotype," Cancer Cell, vol. 8, no. 3, pp. 241 – 254 , 2005.

[19] J. Ophir, I. Cespedes, B. Garra, H. Ponnekanti, Y. Huang, and N. Maklad, “Elastography: Ultrasonic imaging of tissue strain and elastic modulus in vivo," European Journal of Ultrasound, vol. 3, no. 1, pp. 49–70, 1996.

[20] T. J. Hall, A. A. Oberai, P. E. Barbone, A. M. Sommer, N. H. Gokhale, S. Goenezen, and J. Jiang, “Elastic Nonlinearity Imaging," in EMBC: 2009 Annual International Conference of the IEEE Engineering in Medicine and Biology Society, VOLS 1-20, IEEE Engn Med & Biol Soc. IEEE, 2009, Proceedings Paper, pp. 1967 – 1970.

[21] C. L. de Korte, E. I. Cspedes, A. F. W. van der Steen, and C. T. Lance, “Intravascular elasticity imaging using ultrasound: Feasibility studies in phantoms," Ultrasound in Medicine & Biology, vol. 23, no. 5, pp. 735–746,1997.

[22] C. L. de Korte, A. F. van der Steen, E. Cspedes, and G. Pasterkamp, “Intravascular ultrasound elastography in human arteries: Initial experience in vitro," Ultrasound in Medicine & Biology, vol. 24, no. 3, pp. 401–408, 1998.

[23] S. Y. Emelianov, X. Chen, M. O'Donnell, B. Knipp, D. Myers, T. W. Wake_eld, and J. M. Rubin, “Triplex ultrasound: elasticity imaging to age deep venous thrombosis," Ultrasound in Medicine & Biology, vol. 28, no. 6, pp. 757–767, 2002.

[24] A. Skovoroda, L. Lubinski, S. Emelianov, and M. O'Donnell, “Reconstructive elasticity imaging for large deformations," Ultrasonics, Ferroelectrics and Frequency Control, IEEE Transactions on, vol. 46, no. 3, pp. 523-535, 1999.

[25] F. Kallel and M. Bertrand, “Tissue elasticity reconstruction using linear perturbation method," Medical Imaging, IEEE Transactions on, vol. 15, no. 3, pp. 299-313, 1996.

[26] M. Doyley, P. Meaney, and J. Bamber, “Evaluation of an iterative reconstruction method for quantitative elastography," Physics in Medicine and Biology, vol. 45, no. 6, pp. 1521-1540, 2000.

[27] A. A. Oberai, N. H. Gokhale, M. M. Doyley, and J. C. Bamber, “Evaluation of the adjoint equation based algorithm for elasticity imaging," Physics in Medicine and Biology, vol. 49, no. 13, pp. 2955-2974, 2004.

[28] I. Babuska, “The Finite element method with Lagrangian multipliers," Numerische Mathematik, vol. 20, no. 3, pp. 179-192, 1973.

[29] F. Brezzi, “Existence uniqueness and approximation of saddle-point problems arising from Lagrangian multipliers," Revue Francaise D Automatique Informatique Recherche Operationnelle, vol. 8, no. NR2, pp. 129-151, 1974

[30] T. J. R. Hughes, "The finite element method-linear static and dynamic finite element analysis." Mineola, New York, USA: Dover Publications, 2000.

[31] P. J. Blatz, B. M. Chu, and H. Wayland, "On the mechanical behavior of elastic animal tissue," Journal of Rheology, vol. 13, no. 1, pp. 83-102, 1969.

[32] O. Klaas, A. Maniatty, and M. S. Shephard, "A stabilized mixed finite element method for finite elasticity.: formulation for linear displacement and pressure interpolation," Computer Methods in Applied Mechanics and Engineering, vol. 180, no. 1-2, pp. 65 -79, 1999.

[33] A. M. Maniatty, Y. Liu, O. Klaas, and M. S. Shephard, "Higher order stabilized finite element method for hyperelastic finite deformation," Computer Methods in Applied Mechanics and Engineering, vol. 191, no. 13-14,pp. 1491-1503, 2002.

[34] N. H. Gokhale, P. E. Barbone, and A. A. Oberai, "Solution of the nonlinear elasticity imaging inverse problem: the compressible case," Inverse Problems, vol. 24, no. 4, 2008.

[35] R. H. Byrd, P. Lu, J. Nocedal, and C. Y. Zhu, "A limited memory algorithm for bound constrained optimization," SIAM Journal on Scientific Computing, vol. 16, no. 6, pp. 1190-1208, 1995.

[36] D. Michael, L. Hans, "Strain and strain rate imaging by echocardiography – basic concepts and clinical applicability", Curr Cardiol Rev. May 2009; 5(2): 133-148

[37] Brian D. Hoit, "Strain and strain rate echocardiography and coronary artery disease" Cardiovascular imaging. 2011; 4: 179-190

[38] T. Paaladinesh, P. Frederic, “Use of myocardial strain imaging by echocardiography for the early detection of cardiotoxicity in patients during and after cancer chemotherapy: a systematic review”

[39] A. Samani, D. Plewes, “A method to measure the hyperelastic parameters of ex vivo breast tissue samples”, Physics in medicine and biology, vol. 49, no. 18, pp. 4395 – 4405, 2004

[40] P. Wellman, R. H. Howe, “Breast tissue stiffness in compression is correlated to histological diagnosis”, Technical report, Harvard biorobotics laboratory, Division of Engineering and Applied Sciences, Harvard University, 1999

[41] P. Blatz, B. Chu, “On the mechanical behavior of elastic animal tissue”, Journal of Rheology. Vol. 13, no.1, pp. 83 – 102, 1969

[42] J. Humphrey, “Mechanics of the arterial wall: review and directions”, Critical Reviews in Biomedical Engineering, vol. 23, no. 1 – 2, pp. 1 – 162, 1995

[43] C. R. Vogel, “Computational methods for inverse problems”. Philadelphia, PA, USA: Society for Industrial and Applied Mathematics, 2002

[44] S. Goenezen, A. A. Oberai, P. E. Barbone, “Solution of the nonlinear elasticity imaging inverse problem: the incompressible case,” Computer Methods in Applied Mechanics and Engineering. 200 13-16, 1406-1420, 2011

[45] T. J. Hall, P. E. Barbone, A. A. Oberai, J. Jiang, J. F. Dord, S. Goenezen, and T. G. Fisher, “Recent results in nonlinear strain and modulus imaging,” Current Medical Imaging Reviews. 7 313-327, 2011